PNL-10740
UC-510

Gas Bubble Retention and Its Effects on Waste Properties: Retention Mechanisms, Viscosity, and Tensile and Shear Strengths

P. A. Gauglitz
S. D. Rassat
M. R. Powell
R. R. Shah
L. A. Mahoney

August 1995

Prepared for
the U.S. Department of Energy
under Contract DE-AC06-76RLO 1830

Pacific Northwest Laboratory
Richland, Washington

DISCLAIMER

Portions of this document may be illegible in electronic image products. Images are produced from the best available original document.

Executive Summary

Several of the underground nuclear storage tanks at Hanford have been placed on a flammable gas watch list, because the waste is either known or suspected to generate, store, and episodically release flammable gases. Because retention and episodic release of flammable gases from these tanks containing radioactive waste slurries are critical safety concerns, Pacific Northwest Laboratory (PNL)[a] is studying physical mechanisms and waste properties that contribute to the episodic gas release from these storage tanks. This study is being conducted for Westinghouse Hanford Company as part of the PNL Flammable Gas project. Previous investigations have concluded that gas bubbles are retained by the slurry or sludge that has settled at the bottom of the tanks; however, the mechanisms responsible for the retention of these bubbles are not well understood.

Understanding the rheological behavior of the waste, particularly of the settled sludge, is critical to characterizing the tendency of the waste to retain gas bubbles and the dynamics of how these bubbles are released from the waste. The presence of gas bubbles is expected to affect the rheology of the sludge, specifically its viscosity and tensile and shear strengths, but essentially no literature data are available to assess the effect of bubbles.

The objectives of this study were to conduct experiments and develop theories to understand better how bubbles are retained by slurries and sludges, to measure the effect of gas bubbles on the viscosity of simulated slurries, and to measure the effect of gas bubbles on the tensile and shear strengths of simulated slurries and sludges. In addition to accomplishing these objectives, this study developed correlations, based on the new experimental data, that can be used in large-scale computations of waste tank physical phenomena.

For bubble retention experiments, a new method of creating retained bubbles was developed. Results show that dissolving soluble gases into the interstitial liquid followed by pressure reduction provides a suitable method of creating bubbles for measuring bubble retention in waste. An equilibrium CO_2 pressure of 2.4×10^5 Pa (20 psig) is sufficient to create good bubble nucleation and growth with slurries composed of water and glass beads. A pressure reduction rate of 6900 Pa/min (1 psi/min) provided a controllable experiment.

Experiments were completed to further quantify the transition between bubbles that grow by fingering between sludge particles, called dendritic bubbles, and bubbles that grow by displacing the sludge particles, which are referred to as round bubbles. Previously, a Bond number criterion, which is a ratio of gravitational to surface tension forces, was developed to define the transition between the two different mechanisms of bubble growth and retention. In the experiments conducted, the particle size and fluid and particle densities were varied to span a range of Bond numbers. Results for the transition between dendritic and round bubbles showed that the transition moved deeper into a slurry with decreasing particle size and decreasing density difference between the fluid and particle. The observed location of the transition agrees reasonably well with the Bond number scaling when the Bond number is modified to account for the sludge strength. In most cases, very large bubbles appear to fracture

---

(a) Pacific Northwest Laboratory is operated for the U.S. Department of Energy by Battelle Memorial Institute under Contract DE-AC06-76RLO 1830.

simulated sludges at the transition between dendritic and round bubbles, as reported previously. A modified form of this experiment should be suitable for measuring bubble retention in real waste samples.

For the viscosity measurements of bubble slurries, a suitable capillary rheometer was used. Studies were conducted with bubbly slurries composed of polymethylmethacrylate particles in glycerol/water mixtures. Viscosity results were obtained for shear rates generally ranging from 1 to 30 s^{-1}. To quantify the effect of gas bubble fraction on viscosity, slurries containing 48 vol% particles were prepared with 0, 5, 12, 16, 18, and 20 vol% gas bubbles. Also, the effect of particle fraction in a bubbly slurry was investigated for particle fractions ranging from 43 to 50 vol%. In agreement with previous predictions for bubbly slurries with particles and bubbles of similar sizes, the viscosity of the bubbly slurries increased with increasing gas fraction and with increasing particle fraction. A correlation for the viscosity of a bubble slurry that fits the experimental data fairly well was developed to account for the effect of shear rate and gas and particle volume fractions on the slurry viscosity. Important results of the viscosity experiments are that the gas content had a more pronounced effect than expected and that the bubbly slurries become more shear thinning with increasing gas-bubble fraction. The observed shear thinning behavior has been reported in the literature for analogous systems such as concentrated emulsions.

An area not yet investigated is the effect of gas bubbles on the viscosity of very fine particle slurries. For bubbly clay simulants, tensile and shear strength measurements show that the bubbles decrease the strength of the material. It is expected that the viscosity of this type of sludge will also decrease with increasing gas fraction.

Tensile and shear strength measurements of bubbly sludge and glass bead slurry simulants were conducted to quantify the effect of gas bubbles on and to improve the understanding of the relationships between shear and tensile strengths for gas-containing sludges and slurries. Tensile strength measurements were made using a vertical extrusion tensiometer, and shear strength measurements were made using a shear vane for 1) slurries composed of glass particles and water and 2) sludges composed of clays dispersed in water. The vertical extrusion tensiometer was chosen because it can be adapted to hot cell experiments on actual samples. For the clay-based simulants (sludge), results show that the shear strength decreased proportionally to the gas content. For the tensile strength, however, the gas fraction had a more dramatic role, and the tensile strength decreased proportionally to the cube of the gas content. For glass bead slurry simulants, in contrast, the shear and tensile strengths were greater in the presence of gas bubbles. This dramatic difference between clay-based sludge and glass bead slurry simulants highlights the need to perform measurements on real waste samples.

Calculations were also performed to determine how bubbles of different morphology are distributed within a waste tank based on the Bond number criteria. Gas was allowed to migrate within the tank when the gas fraction was sufficiently large to allow gas bubbles to connect. This model shows how the different regimes of bubble retention evolve following a series of rollover events.

Acknowledgments

The authors would like to thank the following contributors for support in this project: Professor William R. Rossen of the University of Texas at Austin for helpful discussions regarding bubble retention mechanisms and the effect of gas bubbles on waste properties; Jim Johnston for his comments on experimental design; and John Sukamto for conducting the multivariable nonlinear least squares calculations for correlating the viscosity data.

Contents

Figures

Tables

Nomenclature

D_p	Particle diameter
D_t	Diameter of vertical extrusion tube
D_v	Shear vane diameter
g	Gravitional acceleration
H_v	Shear vane height
M_v	Mass of piece that breaks free in vertical extrusion (Eq. 5.1)
N_{Bo}	Bond number defined by Eq. 3.1 - 3.3, dimensionless
Q	Flow rate used in Eq. 4.1
R	Radius of capillary tube (Eq. 4.1)
S_t	Tensile strength (Eq. 5.1)
T_{peak}	Peak torque
V_w	Slip velocity at the wall of the tube (Eq. 4.1)
z	Exponent in percolation model (Eq. 5.4)
γ	Surface tension
$\dot{\gamma}_w$	Shear rate at capillary wall (Eq. 4.1)
$-\Delta P/L$	Pressure drop over length L of capillary tube (Eq. 4.2)
η	Viscosity (Pa*s)
η_w	Viscosity at capillary wall
ϕ_c	Solids fraction when tensile strength goes to zero (Eq. 5.4)
ϕ_g	Gas void fraction
ϕ_{gs}	Pore space gas fraction, or gas saturation
τ_s	Shear strength (Eq. 5.2)
τ_w	Wall shear stress used in Eq. 4.2

1.0 Introduction

Several of the underground nuclear waste storage tanks at Hanford have been placed on a flammable gas watch list because the waste is either known or suspected to generate, store, and episodically release flammable gases. Episodic releases of flammable gases from waste tanks is an important safety concern. While each of these episodic releases is unique, the underlying physical mechanisms governing retention of gas within the waste and the sudden release of this gas interrelate the separate events. In some of the observed cases, tank waste separates into an upper liquid layer, termed the "convective" layer, and a lower layer of settled solid particles, or sludge, termed the "nonconvective" layer, as depicted in Figure 1.1 (Allemann et al. 1990a, 1990b, 1991, 1993). The formation of bubbles, their retention, and their release are central to understanding and predicting the volume and rate of gas released during a release event. Earlier studies considered the importance of bubble retention and release and evaluated many proposed gas release mechanisms (Allemann et al. 1990a). However, the mechanisms responsible for the retention of these bubbles are not well understood, and only recently have experimental methods begun to be developed to measure the ability of waste to retain gas.[a]

Bubbles held in settled sludge in the lower part of a waste tank account for most of the gas retained by a waste, and this retention of bubbles therefore plays a pivotal role in gas release events. To retain bubbles, the sludge must resist the buoyant force that is causing the bubbles to rise. Depending on the physical properties of the sludge and the depth of the retained bubbles, the bubbles have been observed to displace the sludge (round bubbles) and be retained by the yield strength of the sludge or to finger between the sludge particles (dendritic bubbles) and be retained by capillary forces (Gauglitz et al. 1994a). Previously, a Bond number criterion, which is a ratio of gravitational to surface tension forces, was developed to define the transition between these two different mechanisms of bubble growth and retention (Gauglitz et al. 1994a). Part of this study is to verify the Bond number scaling.

The rheological behavior of the waste, particularly of the settled sludge, is critical to characterizing the tendency of the waste to retain gas bubbles and the dynamics of how these bubbles are released from the waste. A number of studies have focused on measuring the rheology of simulated and actual double shell tank (DST) waste (Tingey et al. 1994; Bryan et al. 1992; Tennant et al. 1993; Allemann et

---

(a) In his *Test Plan for Tank 241-SY-101 Gas Retention Testing* (101SY-D-TP Rev. 0), P.R. Bredt, Pacific Northwest Laboratory, described the method of creating retained bubbles that involves exposing real waste to radiation with a method similar to Bryan and Pederson's (1994) method of generating gas in simulated waste. Gas is generated by waste decomposition, and the rate of gas generation is controlled by adjusting the radiation dosage. The results of this study will appear in a 1995 PNL report entitled, *The Effect of Dilution on the Gas Retention Behavior of Tank 241-SY-101*, by Bredt, J. M. Tingey, and E. H. Shade.

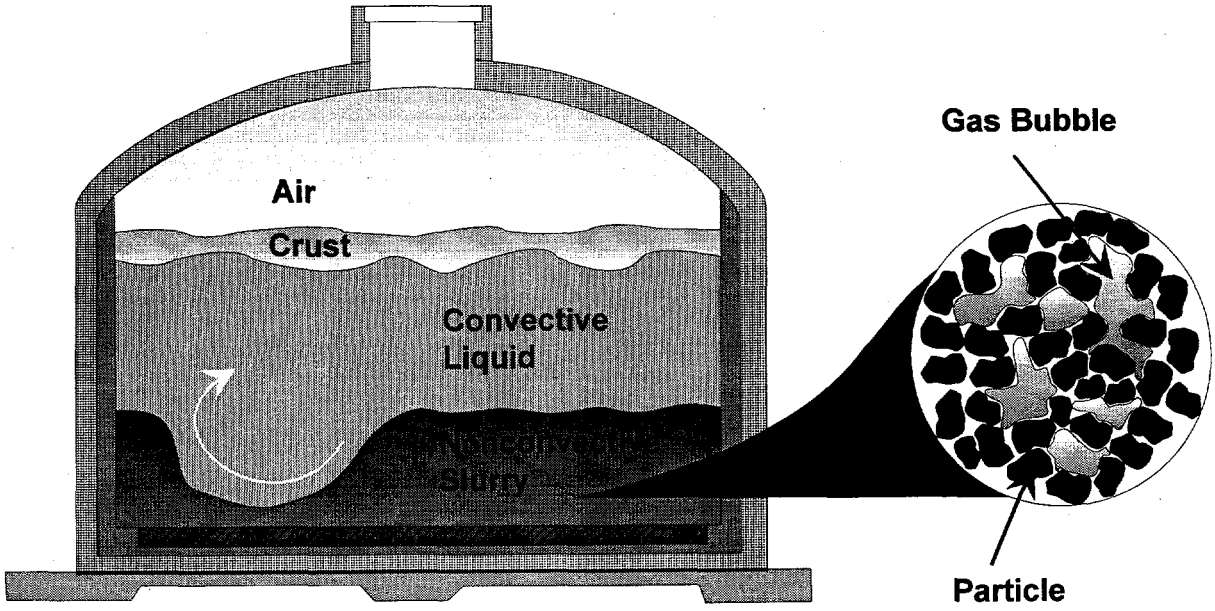

Figure 1.1. Schematic of a Double-Shell Tank with a Nonconvective Layer of Sludge Composed of Particles, Bubbles, and Supernatant Liquid

al.; 1990a; Herting 1991; Reynolds 1992; Hall 1993).[a] While very few literature data are available to assess the effect of bubbles, the presence of gas bubbles in a slurry composed of solid particles, bubbles, and liquid, which we will refer to as a bubbly slurry, is expected to affect the viscosity of the sludge.[b] In a recent study, Gauglitz et al. (1994b) reported on the viscosity of slurries that contained a high *solid* volume fraction and gas bubbles. These data showed that gas bubbles increase the viscosity of the particulate slurry, but the data were not sufficient to develop reasonable correlations. One purpose of this study is to extend the work described by Gauglitz et al. (1994b) and to collect sufficient data to develop correlations of bubbly slurry viscosity.

Sludge shear and tensile strengths have also been implicated in providing a measure of the ability of jet mixer pumps to mobilize sludge (Powell et al. 1995a). Tensile strength provides a more direct measure than shear strength of the cohesive forces within tank sludge. It is these cohesive forces that

---

(a) Two unpublished reports also contain results of studies on the rheology of simulated and actual DST waste: *Rheological Properties of Waste from Tank 101-SY*, by J. M. Tingey (PNL) (1992); and *A Theoretical and Experimental Study of Waste Tank Sludge Rheology Within a Hot Spot or During Draining*, letter report to WHC by D. O. Campbell (1993).

(b) Tennant et al. (1993, p. 53) noted that air bubbles increased the viscosity (less than 50%) of slurries that mimicked tank waste. In these experiments, the volume fraction of air was not determined but was likely quite small.

resist the eroding action of the mixer pump fluid jets. Shear strength measurements alone are often not sufficient to predict mixer pump performance, because shear strength provides a measure of combined cohesive and frictional forces within the sludge. Because a jet mixer pump has effectively mitigated flammable gas releases in Tank 241-SY-101 (Allemann et al. 1994), it is important to understand the factors that control mixer pump effectiveness so that the potential application of mixer pumps in other tanks can be evaluated.

Because of the importance of tensile and shear strengths on gas bubble retention and release, an effort was made to develop methods for making these measurements. Because shear strength is used extensively in soil mechanics and civil engineering, shear strength measurement techniques are well developed and readily available. Tensile strength, however, is rarely used for engineering applications and has only recently been given attention by soil scientists. For this reason there are no well accepted standard techniques for making tensile strength measurements on sludge-like materials. Previously, a literature review was completed, and several candidate tensiometer designs were identified.[a] One of the tensiometer designs recommended for testing Hanford wastes and waste simulants was the vertical extrusion tensiometer, which was used to make tensile strength measurements for the present study. The vertical extrusion tensiometer was chosen because of its technical defensibility and its adaptability for hot cell use. To improve the understanding of the relationships between shear and tensile strengths for gas-containing sludges, the shear and tensile strengths of various simulants were measured at several different gas contents. Shear strength measurements were made using a shear vane and tensile strength measurements were made using a vertical extrusion tensiometer.

This report covers three main activities: studies of bubble retention mechanisms, viscosity measurements of bubbly slurries, and measurements of tensile and shear strengths of bubbly sludges. The development of theories and expressions to correlate the measured physical properties is a fourth activity that contributed to each of the three main areas. Section 2 of this report presents the objectives and scope for the three main activities. Each of the three main activities is described in turn in Sections 3 through 5. For each main activity, a summary of background information and literature is provided, the theory for the experimental approach is discussed, the experiment is described, and finally, the results are presented. The development of correlations for the experimental data is included in each results section. Conclusions can be found in Section 6, and more detailed information is contained in a series of appendixes.

(a) The literature review and candidate designs are described in *Devices for the Measurement of the Tensile Strength of Sludge Simulants*, by M. R. Powell, April 1994, a letter report prepared for Westinghouse Hanford Company by Pacific Northwest Laboratory, Richland, Washington.

2.0 Objectives and Scope

For the bubble retention studies, the first objective was to develop a new method to generate retained gas bubbles in sludge. An important criterion for the new technique is that it should be readily adaptable to measurements on real waste as well as provide a laboratory technique for studies of bubble retention in simulated waste. The second objective for the bubble retention studies was to evaluate the ability of the Bond number (defined in Section 3.1) to discriminate between different bubble retention mechanisms. The scope of the bubble retention studies was to evaluate the technique of 1) dissolving a gas that is soluble in the waste at an elevated pressure, and then 2) reducing the pressure to initiate bubble nucleation and growth. In these studies, CO_2 was used as the soluble gas, and the slurry comprised water and glass beads. To evaluate the Bond number scaling, bubble retention experiments were conducted with particles of different diameters and particles and fluids with different densities. The scaling suggested by the Bond number was used to correlate the data for the location of the transition between different bubble retention regimes.

For the rheology studies, the first objective was to measure the viscosity of bubbly slurries. The capillary rheometer developed previously (Gauglitz et al. 1994b) was used, and the waste simulant was a mixture of polymethylmethacrylate (PMMA) particles suspended in a glycerol/water mixture that had a viscosity of approximately 0.02 Pa*s (20 cP), which is typical of supernatant liquid in 241-SY-101. The second objective was to develop correlations of the viscosity data that correctly reflect the role of gas bubbles. These correlations are suitable for use in large-scale computations of waste tank physics.

For the tensile and shear strength studies, the first goal was to develop an experimental method for measuring the tensile strength of sludge-like materials. It was required that this method be adaptable to hot cell experiments on actual samples. The vertical extrusion tensiometer developed by Powell et al. (1995b) was modified to allow testing with bubbly simulants. The second objective of this activity was to measure the shear and tensile strengths of waste simulants retaining gas bubbles and to correlate the measured strengths with the gas content and bubble morphology. As with the viscosity correlations, the improved understanding of the effects of gas bubbles on the mechanical properties of waste tank sludge will be used in large-scale computations of waste tank physics.

3.0 Gas Bubble Retention Mechanisms

Bubble retention is known to play a pivotal role in the ability of waste to retain gases. To retain bubbles, the sludge must resist the buoyant force that is causing the bubble to rise. Bubble retention in waste is generally classified into one of the five mechanisms shown in Figure 3.1. These mechanisms have been discussed previously (Gauglitz et al. 1994a).[a] In this study, we investigated primarily the yield stress and capillary force retention mechanisms.

3.1 Bubble Retention Mechanisms

Figures 3.2 and 3.3 summarize the bubble retention mechanisms observed recently for gas bubbles retained in beds of settled silica particles (Gauglitz et al. 1994a). In these earlier experiments, gas bubbles were created by mixing yeast with sugar to create CO_2 bubbles. Three distinct regimes of bubble retention were observed. In the upper region of the settled sand, essentially spherical bubbles (round) were observed to displace the sludge particles. Here, bubble retention appeared to be due to yield strength. In the middle region the sludge "fractured," and gas collected in very large bubbles. Retention of these huge bubbles is also yield-stress retention, because the sand containing gas bubbles above the large fracture has an apparent yield stress. In the bottom region, dendritic bubbles that finger between the individual particles were observed, and the bubbles were retained by capillary forces. Equivalent bubble retention mechanisms have been observed in this work, where bubbles were created by reducing the pressure of a slurry containing dissolved CO_2 (see Section 3.5).[b]

Previous studies have shown that the morphology of bubbles retained in sludge can be related to a Bond number (Gauglitz et al. 1994a). The Bond number that follows defines the transitions between bubbles that displace the sludge (round bubbles) and bubbles that finger between the particles making up the sludge (dendritic bubbles):

$$N_{Bo} = \frac{(\rho_{sludge} - \rho_{liquid})Dhg}{4\gamma} \qquad (3.1)$$

(a) N. G. McDuffie (WHC) summarized these mechanisms in a recent presentation entitled, *Flammable Gas Generation, Retention, and Release in High-Level Waste Tanks: Physical and Chemical Models*, presented at Hanford Technical Exchange, "The Hanford High-Level Waste Tank Remediation Program - A Strategic Re-Evaluation" (1994).

(b) W. R. Rossen (University of Texas, Austin) is investigating the role of armored bubbles and bubble/particle attachment as part of the Waste Tank Safety Program Flammable Gas Project at PNL. Aggregates do represent a bubble retention mechanism, but if the aggregates are sufficiently strong, these bubbles do not play a role in gas release events.

where ρ_{sludge} and ρ_{liquid} are the sludge and supernatant liquid densities, D is the pore throat between the sludge particles, h is the depth of the bubble from the top of the sludge, γ is the gas-liquid surface tension, and g is the gravitational acceleration. For Bond numbers greater than 1 gravitational forces dominate, and bubbles deform and neck between particles as they grow (dendritic bubbles). For Bond numbers less than 1, surface tension dominates, and bubbles can displace the sludge particles (round bubbles). Equation (3.1) shows that, deeper into the sludge, gas will collect in dendritic bubbles; while closer to the surface, bubbles will distort the sludge. Equation (3.1) also shows how to scale laboratory studies with simulated sludge to reflect actual tank conditions, and it implies that, as the sludge collects gas and becomes less dense, bubbles that initially grow as dendritic bubbles may shift and continue growing by displacing particles (round or fracture bubbles).

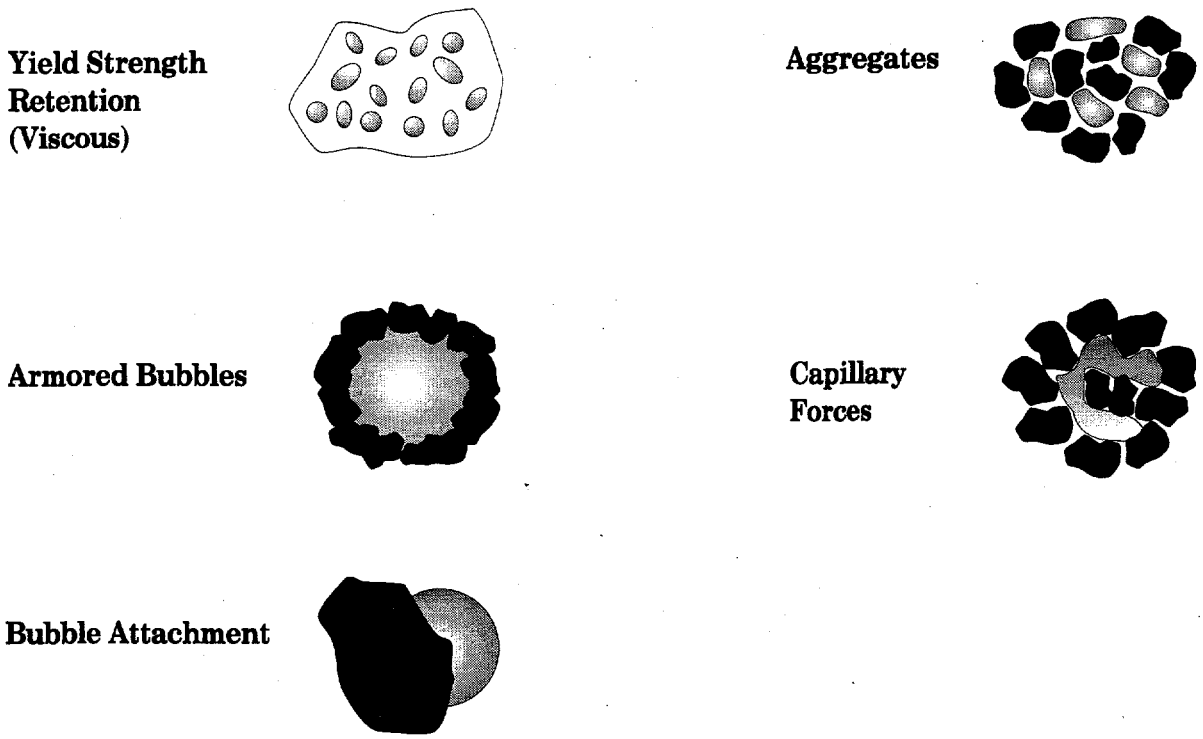

Figure 3.1. Bubble Retention Mechanisms

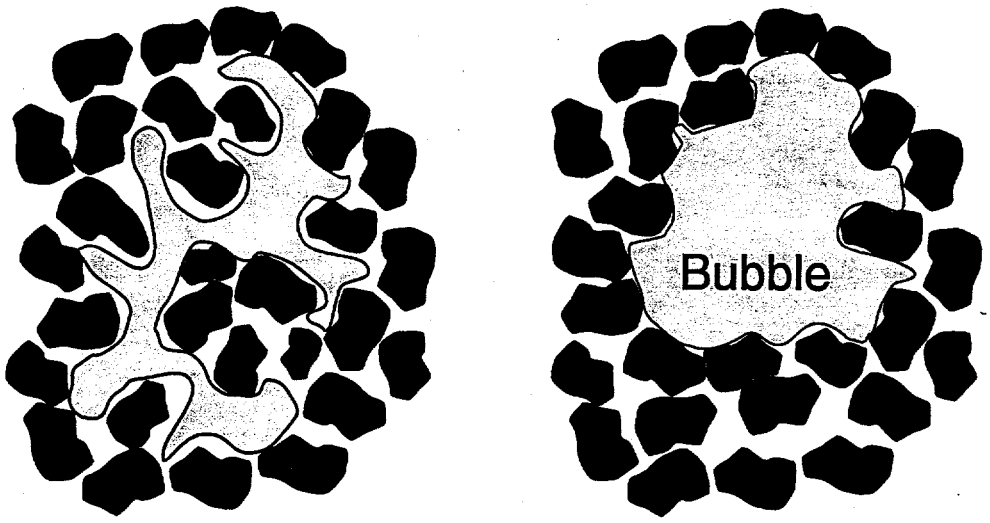

Figure 3.2. Schematic of a Bubble Displacing the Sludge and a Dendritic Bubble Fingering Between Sludge Particles

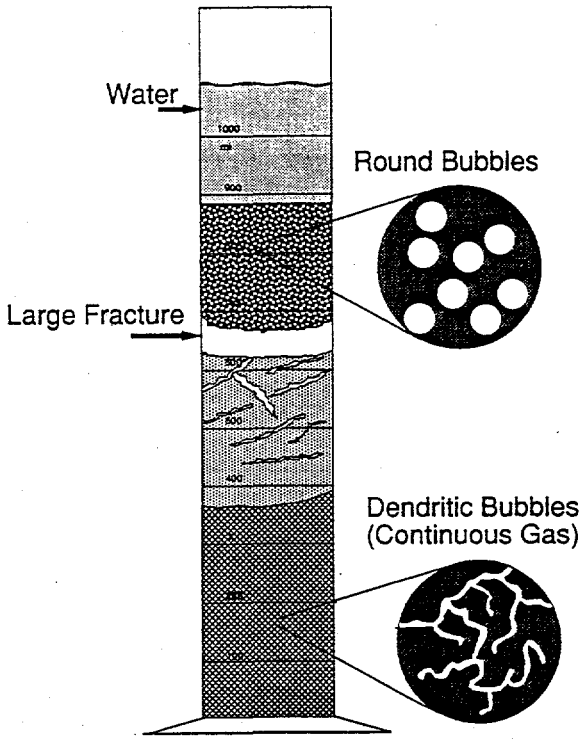

Figure 3.3. Schematic of Bubble Retention in Settled Sand

3.2 Effect of Sludge Strength on Bubble Retention

In the original derivation of the Bond number resulting in Equation 3.1 (Gauglitz et al. 1994a), the forces exerted by a bubble to displace sludge particles were considered. The ratio between the gravitational force holding the particles down to the surface tension force determined whether the bubble would displace the particles or finger between them. In this section, we modify this analysis to include the effect of a material yield strength. When a slurry or sludge has a yield strength, it will be more difficult for a bubble to displace the particles. Figure 3.4 shows the geometry of a model system that we can use for including the strength of the material. Assuming that the maximum force resisting the displacement of the sludge contributed by the sludge strength is equal to $\tau_s A_2$, and modifying the analysis given in Gauglitz et al. (1994a) gives the following modified Bond number:

$$N_{Bo} = \frac{(\rho_{sludge} - \rho_{liquid})ghD}{4\gamma} + \frac{\tau_s D}{4\gamma}\left(\frac{A_2}{A_1}\right) \tag{3.2}$$

where A_2 is the area over which the sludge strength applies, and A_1 is the area of sludge exposed to the bubble.

In general, the sludge strength varies with gas fraction. Determining a suitable (value) expression for A_2 is probably the least well-defined part of this scaling analysis. For widely spaced bubbles, the mechanical deformation of the sludge should occur within a region that is proportional to the bubble diameter. In this situation, the ratio A_2/A_1 should be a constant. When bubbles are close enough to interact, this becomes a poor assumption. In Appendix E, an approach is presented for this scaling analysis that accounts for bubble interaction. Finally, while both tensile and shear deformations are likely occurring, we will not explore this detail for this scaling analysis.

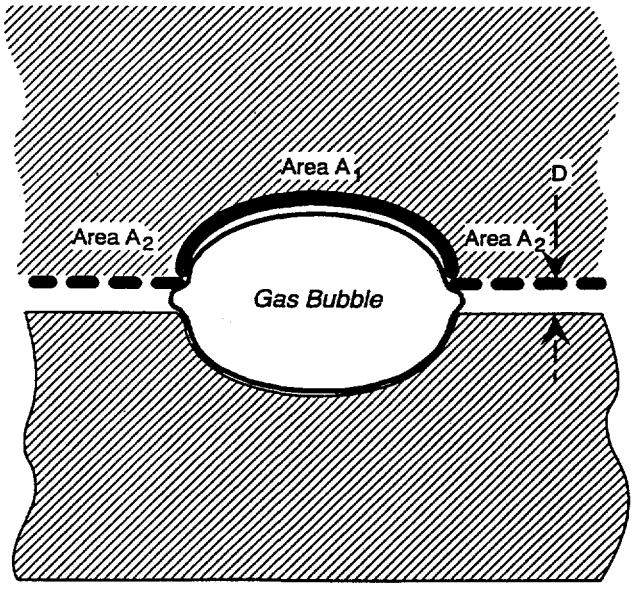

Figure 3.4. Geometry of Bubble Displacing Sludge

In a previous study, Gauglitz et al. (1994a) summarized literature correlations for the effect of gas content and particle size on the tensile strength and presented shear strength data for beadpacks with a range of gas contents. (In addition, shear and tensile strength data for glass beadpacks are presented in Section 5.3.) Theory suggests that the strength of partially liquid saturated porous media should scale as $\tau_s = \tau_s^o/D_P$, where D_P is the particle diameter. Assuming this scaling and that $D_p \sim D$, the effect of sludge strength on the transition depth becomes

$$N_{Bo} = \frac{\Delta \rho g h D}{4\gamma} + \frac{\tau_s^o}{4\gamma}\left(\frac{A_2}{A_1}\right) \tag{3.3}$$

Rearranging this equation and letting $Bo=1$ gives the following result for the transition depth between dendritic and round bubbles:

$$h = \left[1 - \frac{\tau_s^o}{4\gamma}\left(\frac{A_2}{A_1}\right)\right] \frac{4\gamma}{(\rho_{sludge} - \rho_{liquid})gD} \tag{3.4}$$

Because the τ_s^o term in Equation 3.4 is negative, this result shows that the strength of the sludge makes it more difficult for bubbles to displace the sludge. Accordingly, the transition depth is shallower, and more dendritic bubbles are expected in the waste. As described in Section 3.5.4, this modification agrees with our experimental observations. A second important result implied by Equation 3.4 is that, if the τ_s^o term is sufficiently large, the transition depth becomes negative. Physically, this implies that bubbles can never overcome the sludge strength and displace it. In this case, only dendritic bubbles are expected.

3.3 Approach

The experimental approach for creating bubbles in sludge involves dissolving a soluble gas into the supernatant liquid at an elevated pressure, then reducing the pressure to allow bubbles to nucleate and grow. The gas must be sufficiently soluble in the supernatant liquid, and the experiments must also allow controlled bubble growth. If bubble growth is too rapid, the nucleation of bubbles will be unrealistic, and the mechanism of growth may become controlled by viscous or inertial forces. In the real situation of bubble growth in tank waste, the bubbles grow very slowly as gases are generated by reaction and diffuse through the supernatant liquid to the bubbles. In the experiments we describe herein, we varied the rate at which the pressure was reduced and thereby affected the rate of bubble growth.

A number of gases are suitable for this study, including ammonia (NH_3), CO_2, and nitrous oxide (N_2O). Table 3.1 shows the Henry's Law constants for these gases in water and in a chemical simulant. Of the gases listed, ammonia is the most soluble, followed by nitrous oxide and then CO_2. Norton and Pederson (1994) reported the solubility of ammonia in chemical simulants that have high concentrations of sodium hydroxide and salts. The added salts generally reduce the solubility of the gases, although the solubility of ammonia in SY1-SIM-91A is still a hundred-fold larger than that of CO_2 in water.

Table 3.1. Solubility of Candidate Gases in Water and Waste Simulant

Gas	Henry's Constant (atm/moles/liter) water @ 20°C	Henry's Constant (atm/moles/liter) SY1-SIM-91A	Comments
NH_3	0.013[a]	0.122[a] @ 20°C 0.252[a] @ 50°C	Combustible Hazardous
N_2O	36[b]		Oxidizer
CO_2	22[c]		Will react with waste

(a) Norton and Pederson (1994), assuming 1 kg water ~ 1 liter.
(b) Perry (1950).
(c) Yaws et al. (1991).

To conduct tests on real waste samples, a soluble gas compatible with the waste must be used. CO_2 is not suitable because of chemical interactions with the alkaline waste. Ammonia is quite soluble in chemical simulants that mimic slurry waste, and it is a good candidate for real waste studies. In a recent companion study, experiments using ammonia gas and chemical simulants were successful in nucleating retained bubbles (Rassat and Gauglitz 1995), particularly when a vacuum was applied to accentuate bubble growth.

The actual gas retained in bubbles by real waste, such as in Tank 241-SY-101, is a mixture of primarily hydrogen, nitrous oxide, nitrogen, and ammonia (Allemann 1993). For the laboratory technique we are investigating to succeed, the gas must be reasonably soluble in the liquid waste. A very high gas pressure would be required to dissolve sufficient hydrogen and nitrogen, because these gases are very insoluble. Accordingly, experiments to dissolve gas mixtures representative of actual tank conditions are impractical.

For bubble retention measurements on real waste samples, a modification of the approach described here and in Rassat and Gauglitz (1995) should provide a suitable measurement of bubble retention. The modified approach involves applying a vacuum to the sample to enhance bubble nucleation and growth, following a dosage of radiation sufficient to create a small volume of gas. In this experiment, gases representative of actual tank conditions will be generated and retained as bubbles.[a]

(a) In his *Test Plan for Tank 241-SY-101 Gas Retention Testing (101SY-D-TP Rev. 0) (1994)*, P. R. Bredt, Pacific Northwest Laboratory, Richland, Washington, described the method of creating retained bubbles that involves exposing real waste to radiation with a method similar to Bryan and Pederson's (1994) method of generating gas in simulated waste. Gas is generated by waste decomposition, and the rate of gas generation is controlled by adjusting the radiation dosage. The results of this study will appear in a 1995 PNL report entitled, *The Effect of Dilution on the Gas Retention Behavior of Tank 241-SY-101*, by Bredt, J. M. Tingey, and E. H. Shade.

3.4 Experimental Method and Materials

Figure 3.5 shows a schematic of the apparatus for conducting these studies. The gas of choice is delivered from a high-pressure cylinder into the top of the sample holder. The gas can be mixed into the sludge/slurry by a number of methods. In these initial studies, in which we sought to determine a suitable CO_2 pressure and rate of pressure reduction, we simply mixed the CO_2 into the water/glass-bead sludge by rocking the sample chamber back and forth. Prior to pressurization and mixing, the headspace in the sample holder was purged with CO_2. The technique of using soluble gases can also be conducted in a manner where the sludge is disturbed minimally. To accomplish this, the supernatant liquid can be recirculated through the sludge with a pump until the sludge is uniformly mixed with supernatant liquid containing dissolved gas.[a] A few experiments described in Section 3.5 were conducted with the recirculation apparatus. In all the experiments discussed here, CO_2 was used as the soluble gas and deionized water was the liquid (interstitial and supernatant). In the majority of experiments, spherical glass beads were used to represent waste sludge particles, and in each experiment approximately 125grams ($\sim$75 mL bead pack) of glass beads were mixed with about 40 mL of water. To test the effect of particle density on the bubble transition height, an experiment was conducted with 71 μm nominal diameter PMMA plastic particles (ρ = 1.21 g/mL versus ρ = 2.55 g/mL for glass) using comparable sludge volumes.

Figure 3.6 depicts a bubble growth experiment schematically. The figure shows an initial settled slurry and the same slurry after bubble nucleation and growth has caused slurry growth. Some measurements that are taken during a bubble retention experiment are also shown in Figure 3.6. The levels of the liquid surface and the settled beads are recorded as a function of time; the pressure is also recorded.

In many situations, the bubble shape (dendritic, round, or fracture) can be identified qualitatively by careful visual observation. While only the bubbles near the wall of the test vessel can be observed, these bubbles are typically representative of the bubbles that are completely inside the sludge. The volume of gas retained within the sludge by all mechanisms at any given time is determined by measuring the difference between the initial and final (current) heights of the supernatant liquid level. Because dendritic bubbles displace slurry liquid from the sludge and do not affect the overall sludge layer height, changes in the sludge height reflect gas retained as bubbles that have displaced the slurry particles (e.g., round bubbles or large fracture bubbles). The quantity of gas retained by dendritic bubbles is then deduced from the difference in the level changes of the supernatant liquid and the sludge surfaces.

3.5 Results and Discussion

Bubble retention experiments were conducted for a range of CO_2 pressures, pressure reduction rates, and glass bead diameters; sludges of PMMA particles were also studied to investigate the role of particle density. Pressures are reported as absolute pressure in Pascals (Pa) except where noted. In general, the mechanisms of bubble retention depicted in Figures 3.3 and 3.6 were observed: dendritic

---

(a) In a related project, an apparatus for conducting this type of recirculation experiment that minimizes waste disturbance has been assembled as part of PNL's Hydrogen Mitigation Project. The successful development and testing of this apparatus is described in Rassat and Gauglitz (1995).

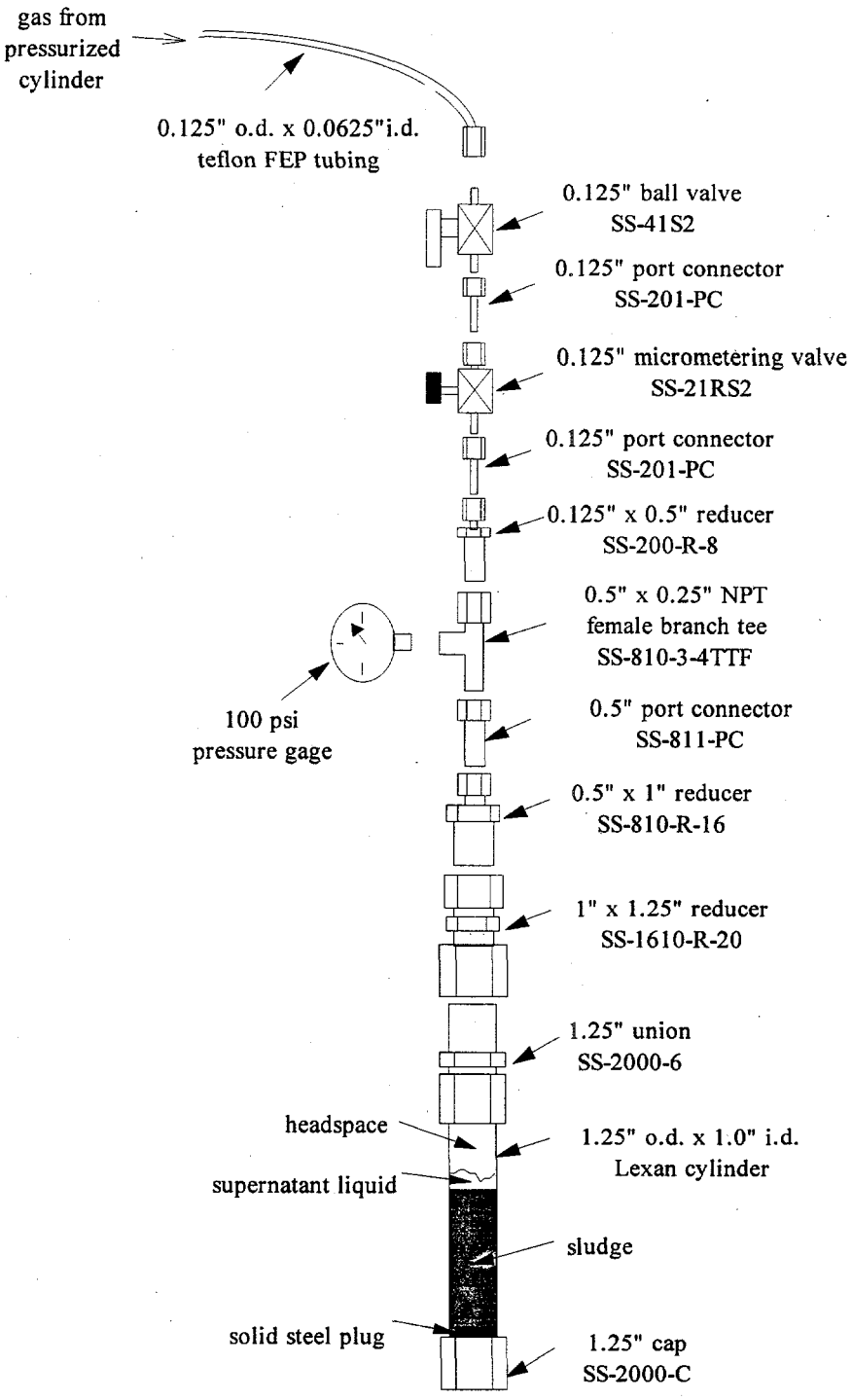

Figure 3.5. Exploded View of Bubble Retention Apparatus (specific Swagelok fittings are identified)

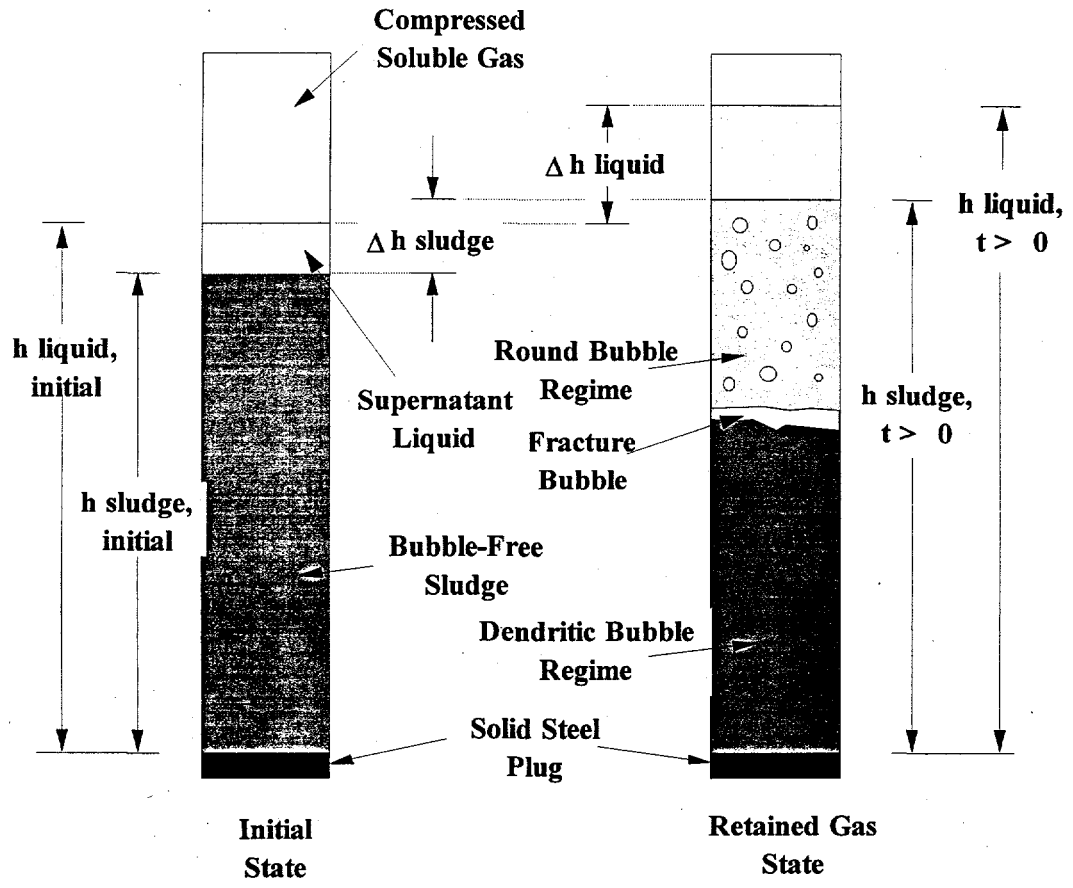

Figure 3.6. Schematic Representation of Changes in Supernatant Liquid and Sludge Heights During a Bubble Retention Experiment (in the initial state the liquid and sludge levels are at a minimum; at some later time, when dendritic, round, and/or fracture bubbles have formed, new liquid and sludge heights indicate the mechanism of bubble retention)

bubbles were seen in a lower region of the settled slurry, round bubbles displaced particles in the upper region, and fractures often occurred at the transition between the two regimes. The results of the specific experiments are described below. Appendix A contains tables of all the bubble retention data.

3.5.1 Initial Pressure

The experiments described here spanned a range of initial pressures (20, 35, and 50 psig) that, after mixing, gave final equilibrium pressures of 1.7×10^5, 2.5×10^5, and 3.4×10^5 Pa (10, 22, and 34 psig). Figure 3.7 shows the levels of the supernatant liquid as a function of time for experiments conducted at the three equilibrium CO_2 pressures. In these three experiments, the pressure was reduced at about 6900 Pa/min (1 psi/min), and the slurry was 90-micron glass beads in water. For the lowest pressure, the liquid level rose about 1.5 cm, which we believe is insufficient for accurately observing the

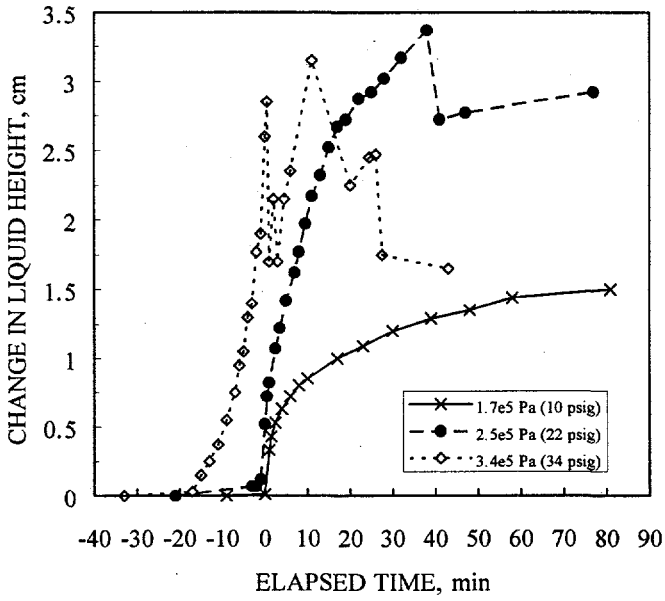

Figure 3.7. Effect of Initial Equilibrium CO_2 Pressure on Rate of Overall Gas Retention Within Sludge for 0.09-mm Nominal Diameter Glass Beads in Water (system was depressurized at ~6900 Pa/min [1 psi/min] for all experiments, and elapsed time is measured from the point at which atmospheric pressure was achieved on depressurization)

various bubble retention mechanisms. For the two higher pressures, the rise in the liquid level was more acceptable. With these higher initial pressures, the curves in Figure 3.7 show a very rapid, but similar, rise in the levels. The rapid drops in heights result from gas bubble release from the sludge.

A useful technique for evaluating these bubble retention experiments is to compare the growth of the levels of the supernatant liquid and settled sludge. If only dendritic bubbles are present the settled sludge does not grow, because liquid is displaced from the spaces between the particles. In contrast, when bubbles displace the sludge, both the sludge and supernatant levels increase. Figure 3.8 shows the relationship between the growth in the settled sludge and supernatant for the three initial pressures. The three curves generally overlap, indicating that the bubble retention mechanisms are not affected by the initial pressure. In general, the lowest CO_2 pressure that provides suitable bubble nucleation and growth is the best choice for conducting experiments, because the bubble nucleation and growth progresses in a more controlled manner. Based on the set of experiments depicted in Figures 3.7 and 3.8, the most suitable equilibrium pressure for CO_2, water, and 0.09-mm glass beads is about 2.4×10^5 Pa (20 psig).

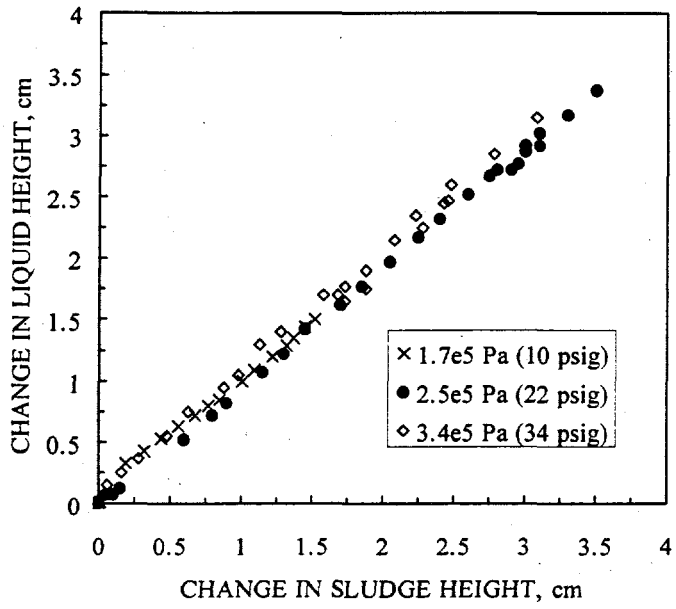

Figure 3.8. Effect of Initial Equilibrium CO_2 Pressure on Change in Supernatant Liquid Height Relative to Change in Sludge Level for 0.09-mm Nominal Diameter Glass Beads in Water (system was depressurized at ~6900 Pa/min [1 psi/min] for all experiments)

Figure 3.8 shows essentially no difference between experiments; however, when experiments are conducted with different diameter beads to vary the predominant bubble retention mechanisms, the relationship between liquid level and slurry level growth is noticeably different. This will be shown in Section 3.5.3.

The most suitable CO_2 pressure (2.4×10^5 Pa or 20 psig) can be used to estimate the pressure of ammonia necessary to conduct similar experiments on real waste. Based on the Henry's constant data reported in Table 3.1, we estimate that an equilibrium of 1600 Pa gauge (0.23 psig) will be acceptable for ammonia experiments with real waste at 50°C. This assumes the pertinent temperature of real waste studies is about 50°C. For lower temperatures, the ammonia solubility is greater, and an even lower pressure would be required.

3.5.2 Pressure Reduction Rate

The rate of pressure reduction controls how quickly the bubbles nucleate and grow. Experimental results show that if the pressure is reduced too quickly, bubble growth occurs too fast to allow reasonable observation of the experiment. When the pressure reduction rate is sufficiently slow, nucleation and retention of the bubbles occur over a period of 20 to 60 minutes. The physical process of bubble nucleation and growth does depend on the method and time scale driving bubble formation. Many of the issues pertinent to bubble growth in porous media have been addressed recently in connection with studies of gas-bubble formation in oil reservoirs (solution gas drive) and boiling in porous media (Li and Yortsos

1995; Satik and Yortsos 1991; Yortsos and Parlar 1989), and a model of bubble growth by diffusion has been reported by Allemann (1990a). Bubble nucleation and growth are complex due to the interaction of nucleation, diffusion, heat transfer (in boiling), and viscous forces. However, a few general observations can be gleaned from these studies. First, very slow bubble growth favors fewer but larger bubbles that are widely spaced (dissolved gases diffuse to the bubble that can expand most easily). Second, very fast bubble growth favors closely spaced smaller bubbles. Here, the dissolved gases will nucleate a new bubble rather than diffuse over a long distance to a more favorable bubble. In contrast to the oil reservoir and boiling problems, within typical tank waste many bubbles capable of growing exist. In this case, the pre-existing distribution of bubbles dominates the number and size of bubbles that grow. Accordingly, for bubble growth in typical tank waste, it is likely that the rate of bubble growth will not play a major role.

Figure 3.9 shows the level of the supernatant liquid as a function of time for pressure reduction rates of $>6.9 \times 10^4$, 6900, and 1400 Pa/min (>10, 1, and 0.2 psi/min). These experiments were conducted with a CO_2 equilibrium pressure of about 2.4×10^5 Pa (20 psig) and with water and 90 micron glass beads as the slurry. For the fastest pressure reduction rate of $>6.9 \times 10^4$ Pa/min (>10 psi/min), complete slurry growth occurred over a period of a few minutes, which was too fast for making easy observations. The intermediate rate of 6900 Pa/min (1 psi/min) resulted in slurry growth over a 20-60 minute period and provided an acceptable experiment. The slowest rate of pressure reduction also provided an easy experiment to observe.

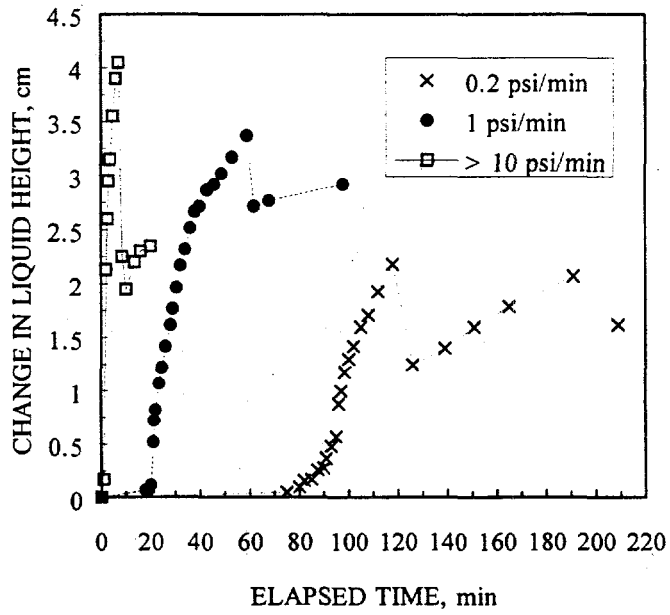

Figure 3.9. Effect of System Depressurization Rate on Rate of Overall Gas Retention In Sludge for 0.09-mm Nominal Diameter Glass Beads in Water (initial [equilibrium] CO_2 pressure $\sim 2.4 \times 10^5$ Pa [20 psig]; elapsed time was measured from start of depressurization)

Figure 3.9 shows that the pressure reduction rate affects the ultimate bubble retention before the level drops due to bubble release. To understand the importance of this effect, it is helpful to consider the relative growth of the supernatant liquid and settled slurry levels, which is a good diagnostic for the mechanism of bubble retention. Figure 3.10 shows this relationship for the three pressure reduction rates. Interestingly, the curves are nearly the same regardless of the pressure reduction rate; however, the fastest pressure reduction rate resulted in bubble growth that occurred too quickly for easy observation. For the intermediate and slowest pressure reduction rates, the bubble generation and retention appeared equivalent, so there is no need to conduct the experiment this slowly. Thus it appears that the best pressure reduction rate is 6900 Pa/min (1 psi/min).

3.5.3 Particle Diameter and Buoyancy

Figure 3.11 shows the liquid surface level as a function of time for four slurries covering a range of bead sizes. In these experiments, the pressure reduction rate was 6900 Pa/min (1 psi/min), and the higher CO_2 pressure of 3.2×10^5 Pa (32 psig) was used. The results show that the different size beads gave different rates and ultimate levels of growth. Figure 3.12, which relates the rise in the surface liquid and settled slurry levels for the same experiments, provides a more interesting comparison. For the largest beads ($\sim$1.0 mm), the liquid level rose faster than the slurry; this indicates predominantly

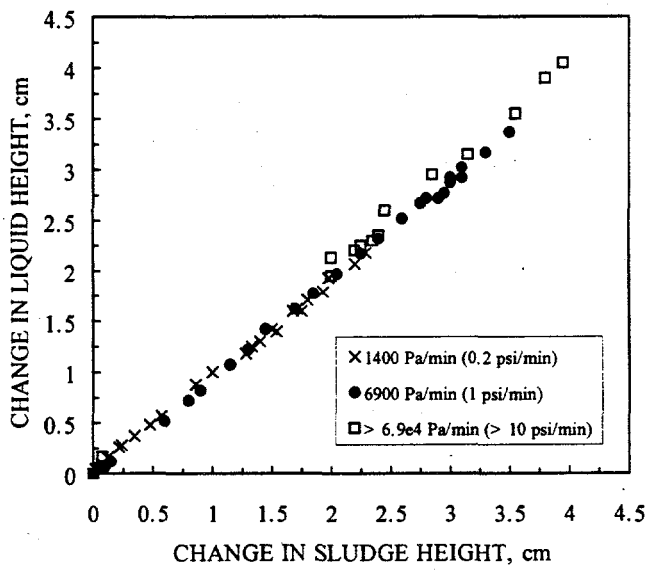

Figure 3.10. Effect of System Depressurization Rate on the Change in Supernatant Liquid Height Relative to Change in Sludge Level for 0.09-mm Nominal Diameter Glass Beads in Water (initial equilibrium CO_2 pressures $\sim 2.4 \times 10^5$ Pa [20 psig] for all experiments)

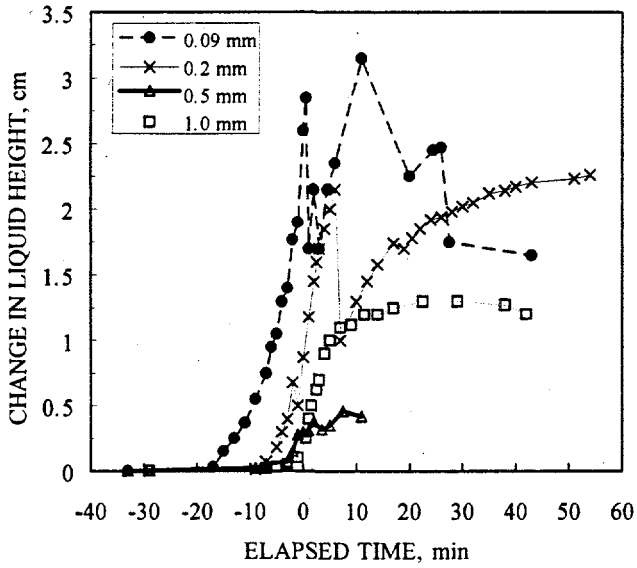

Figure 3.11. Effect of Nominal Glass Bead Diameter on Rate of Overall Gas Retention in Water-Based Sludges (initial [equilibrium] CO_2 pressures ~3.1 x 10^5 Pa [30 psig]; system depressurized at ~6900 Pa/min [1 psi/min]); elapsed time measured from point at which atmospheric pressure was achieved on depressurization)

dendritic bubbles displacing the liquid between the particles. For the smaller beads (90 and 200 microns) the surface liquid and slurry levels rise about equally, indicating that the retained bubbles are displacing the slurry particles, causing a growth in the slurry level. In this situation, bubbles are retained predominantly as round or fracture bubbles. As seen in Figure 3.12, the relative contributions of round and dendritic bubbles are intermediate for the 0.5-mm beads, as is expected based on bead size. However, the maximum growth in the 0.5-mm bead sludge was much less than expected, and we believe this is due to surface contamination of the beads.

Figure 3.13 shows the results for a 75:25 (wt/wt) mixture of 1.0-mm and 90-micron beads compared with the results for single-size beads. The mixture results fall between those for single-size beads. Interestingly, the mixture shows initial growth with dendritic bubbles, then shifts its behavior and grows by displacing the slurry particles.

Visual observations of the locations at which the bubble retention mechanism changed from dendritic to round bubbles were made in each of the bubble retention experiments. In many cases, the transition position could be identified by the formation of a fracture bubble in the particulate sludge. With continued gas generation, movement of gas within the sludge, and gas release events, the location of fractures within the sludge changed over time, probably due to localized changes in the strength of the sludge. For the Bond number correlation studies, the bubble retention mechanism transition height was obtained from the initial fracture location or from direct observation in the change in bubble type, and the height (depth) was measured from the surface of the particulate layer.

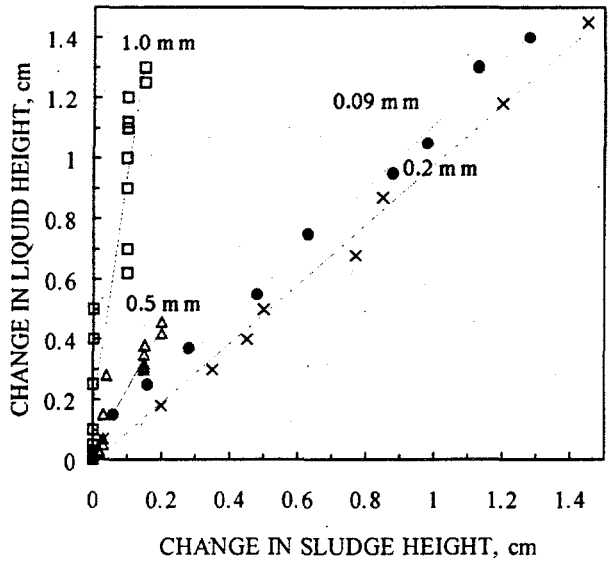

Figure 3.12. Effect of Nominal Glass Bead Diameter on Change in Supernatant Liquid Height Relative to Change in Sludge Level in Water-Based Sludges (initial [equilibrium] CO_2 pressures ~3.1 x 10^5 Pa [30 psig]; system depressurized at ~6900 Pa/min [1 psi/min])

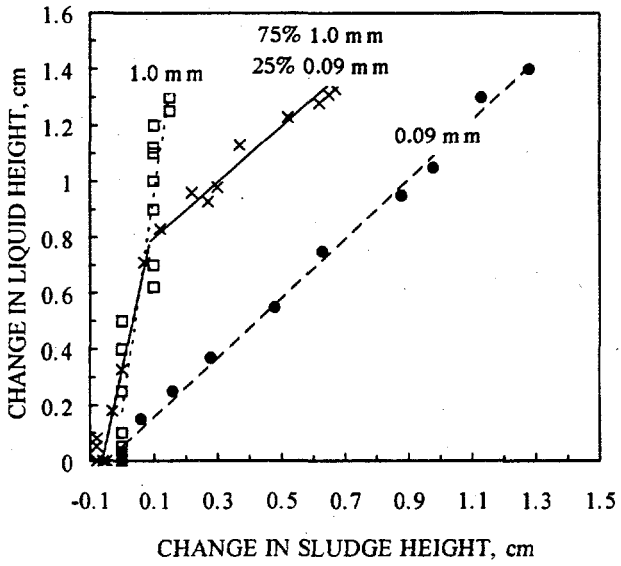

Figure 3.13. Effect of Sludge Particle Diameters on Change in Supernatant Liquid Height Relative to Change in Sludge Level In Water-Based Sludges for 0.09 mm, 1.0 mm, and 75% 1.0 mm/25% 0.09 mm (wt/wt) Mixture of Glass Beads (initial [equilibrium] CO_2 pressures ~3.1 x 10^5 Pa [30 psig]; system depressurized at ~6900 Pa/min [1 psi/min])

Figure 3.14 shows the measured transition heights for a series of glass bead experiments with nominal sizes ranging from 30 to more than 1000 μm; in each case the fluid consisted of water and dissolved CO_2 depressurized at a rate of ~6900 Pa/min (1 psi/min) to atmospheric pressure. For particles smaller than 90 μm the equilibrium pressure was ~2.4 x 10^5 Pa (20 psig), and for 90 μm and larger particles the pseudo-equilibrium pressure was ~3.1 x 10^5 Pa (30 psig). Numerous 90-μm glass bead experiments at a variety of equilibrium pressures and reduction rates indicated no systematic variability of the transition location with these variables. As predicted from the originally proposed Bond number correlation, Equation 3.1, the height of the measured transitions was observed to move deeper in the sludge layer as the particle diameter decreased. However, as shown in Figure 3.14, the simple Bond number result (Equation 3.1, dashed line) over-predicts the transition depth for the glass bead samples, particularly for the smaller bead sizes. Figure 3.14 shows that the modified Bond number correlation (Equation 3.2), which includes a term to account for the effect of sludge strength on gas bubble retention, provides a much better fit to the glass bead data. Details of the Bond number correlation modeling efforts are addressed in the following section.

The bubble retention experiments for all particles less than 90 μm were conducted in a recirculating fluid bubble retention apparatus conceptually similar to that shown in Figure 3.14 (Rassat and Gauglitz 1995). The alternative apparatus was needed to overcome sludge hang-up in the fittings of the simpler apparatus when the sample was rocked back and forth.

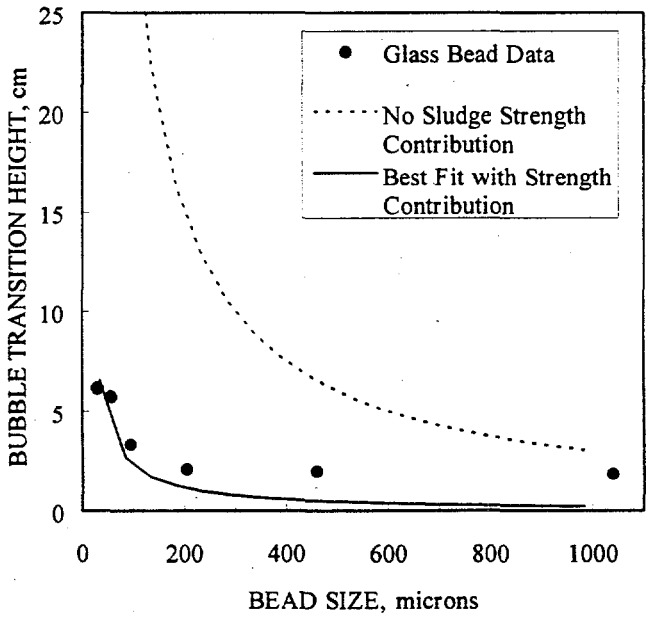

Figure 3.14. Measured Bubble Retention Mechanism Transition Heights for Glass Beads as a Function of Particle Size (predicted transition heights for the original Bond number correlation and the best fit of the modified Bond number correlation are also presented)

The Bond number scaling laws indicate the dependence of the bubble transition height on the difference in density between the sludge (particles, interstitial liquid, and gas bubbles) and the supernatant liquid phase. This buoyancy dependence was investigated experimentally using a PMMA particulate sludge in water, which was pressurized with CO_2 to an equilibrium gas pressure of about 2.4 x 10^5 Pa (20 psig). The bubble transition height of this sample was about 9.4 cm below the sludge surface, considerably deeper than even the 30-micron glass bead system (h= 6.1 cm). This difference is readily attributable to the density differences in the two systems: the glass bead sludge density was ~1.98 g/mL and the PMMA sludge density was about 1.13 g/mL, giving $\Delta\rho$ values of 0.98 and 0.13 g/mL, respectively. In computing the sludge densities, the pore volume fraction for all bead sizes and types was assumed to be 0.37, the gas fraction was assumed to be negligible, and water and glass densities of 1.0 and 2.55 g/mL were used.

3.6 Bond Number Scaling

Glass bead bubble retention transition height data of Figure 3.14 and the 71 μm PMMA experiment transition height are plotted together in Figure 3.15. To allow these data points to be compared on the same plot, the particle diameter is scaled by the density difference (sludge-supernatant liquid). Also shown in Figure 3.15 is a series of parametric curves derived from the modified Bond number transition height (Equation 3.4), where the ratio of areas A_2/A_1 is used as the adjustable parameter. To obtain these curves, a water-CO_2 gas surface tension of 70 dyne/cm was used, the pore throat diameter was assumed equal to the particle diameter, and a value of the constant τ_s° ($=\tau_s D_p$) was estimated from shear and tensile strength data of 90 μm glass beads (Section 5.3.1). At the time of initial fracture formation in the packed sludges, the overall gas retention within the sludge was small; gas fractions of about 0.05 or less were common at the point at which the transition height was identified. From the glass bead shear and tensile strength data (Figure 5.5), a sludge strength (τ_s) on the order of 10 kdyne/cm^2 at 5% gas fraction was estimated. It is also valid to lump the terms $\tau_s^\circ A_2/A_1$ into a single adjustable parameter and obtain results similar to those presented in Figure 3.15.

In Figure 3.15, the curve for A_2/A_1 = 0 reflects the originally formulated Bond number scaling model in which there is no contribution to gas retention from the sludge yield strength. The curves with A_2/A_1 = 2 and 3 are bounding cases for the measured transition data, and the plot of A_2/A_1 = 2.8 represents the best fit of Equation 3.4 to the glass bead data shown in Figure 3.14. In total, the best fit yield strength correction term ($\tau_s^\circ A_2/[4\gamma A_1]$) has a value of about 0.9. A value of 0 for this term indicates no strength contribution, and a value of 1 represents a limit where the sludge is so strong that round bubbles never form and dendritic bubbles dominate. This result shows that some round bubbles form but only in a smaller region near the top of the settled sludge.

The PMMA and glass bead data in Figure 3.15 cross the best fit line but do not follow it exactly. The distinctly flat slope of the measured data indicates a transition height dependence somewhat different from the $1/D$ dependence reflected in the parametric curves. The source of this unpredicted dependence is not understood. One consideration is the effect of particle size distribution on the gas retention mechanism. In support of this, it was demonstrated in Figure 3.13 that bubble retention in a two-sized mixture of glass beads behaved like the larger bead fraction in the initial stages of the experiment. Another area that deserves continued attention is understanding the effect of particle size on the yield strength of particulate sludges. In developing Equation 3.4, the strength was assumed to scale as $1/D_p$ as suggested in the literature. Limited data (Gauglitz et al. 1994a and Section 5.3.1) for shear strengths

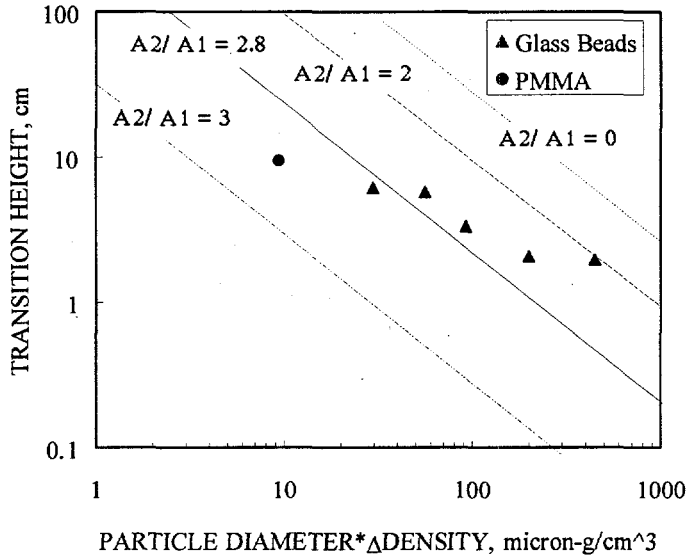

Figure 3.15. Predicted Dendritic/Round Bubble Transition Heights as a Function of a Scaled Particle Size and the Relative Importance of Sludge Strength Contributions (A_2/A_1) (the measured transition points for various glass bead sizes and PMMA are also shown)

of moist agglomerates suggest that this strength contribution scales as $(1/D_p)^{0.6\text{-}0.7}$. Future work should focus on shear and tensile strength measurements in the critical near-liquid-saturation regime, where, unfortunately, measurements are more difficult to obtain. We have also assumed that the strength of the bubbly PMMA slurry is identical to a glass bead slurry. Finally, interactions of the sludge with the wall also warrant consideration. In tensile strength determinations of moist glass beadpacks by extrusion (Section 5.3.1), strong frictional resistance between the beadpacks, particularly those with high gas contents, and the plastic extrusion tube walls were observed. However, since the fraction of gas retained is low at the point at which the transition height is identified in bubble retention experiments, wall effects may be negligible.

4.0 Viscosity of Bubbly Slurries

Tank waste containing bubbles generally has up to about 20 vol% gas bubbles (Allemann et al. 1993), so the range of interest in measuring the bubbly slurry viscosity is at lower gas fractions. Settled tank sludge is essentially at its maximum packing fraction in solid particulate, which is the point at which the suspension viscosity increases rapidly with solids loading (Barnes et al. 1989).[a] Therefore, a simulated slurry to be representative of tank waste, we believe the particle volume fraction should be about the same as the maximum packing fraction, and the gas volume fraction should range from 0 to 20 vol%.

As mentioned previously, very few data exist on the effect of both bubbles and solids on the rheological behavior of slurries. The few data reported in the literature came from studies on the use of foams to improve the pipeline transport of coal slurries or crude oils mixed with reservoir sand. Thondavadi and Lemlich (1985) investigated the ability of foams with relatively high gas fractions (about 90 vol%) to carry fine particles (see also Thondavadi 1983). Solids loading was up to 35 wt%, but this actually represents less than 2 vol% particles. Kundu and Peterson (1987) also investigated slurry transport with foams and measured the viscosity of bubbly slurries, but only with solids fractions up to 2.5 vol% and very high gas fractions ranging from 30–60 vol%. Okpobiri and Ikoku (1983) studied the flow properties of gas/particle/liquid slurries but only at high gas fractions (64 to 99 vol%). In a study of an analogous system of oil droplets and sand particles suspended in water, Jamaluddin et al. (1994) measured the viscosity of suspensions, but only for solids fractions from 0–5 vol%.

In most cases, increasing the solids or gas-bubble volume fraction is expected to increase the viscosity of the slurry (Gauglitz et al. 1994b). However, the viscosity of a bubbly slurry can be less than that of the bubble-free slurry if the gas bubbles distort without resistance, as can occur when viscous forces are large compared with surface tension forces. This behavior may occur with very viscous supernatant liquid when bubbles are large compared with the particles or if surface tension is negligible. For the experimental slurries we investigated, the bubbles increased the viscosity of the slurry.

4.1 Viscosity Measurement by Capillary Rheometry

The advantage of a capillary rheometer is that the viscosity of any time-independent fluid (excluding thixotropic suspensions) can be obtained from flow-rate versus pressure-drop data. In a recent report, Gauglitz et al. (1994b) described the theory for using a capillary rheometer to measure the viscosity of bubbly slurries. Additional discussions of capillary rheometry are given by Nguyen and Boger (1992), Macosko (1994), and Barnes et al. (1989). The theoretical analysis results in equations giving viscosity as a function of shear rate without assuming any model for the fluid; the analysis gives the following expression for the shear rate $\dot{\gamma}_w$ at the capillary wall. The analysis also assumes the slurry is homogeneous and that the slurry can be characterized by a viscosity that depends on shear rate.

(a) The maximum packing fraction is also discussed in a letter report by L. A. Mahoney and D. S. Trent, *Correlation Models for Waste Tank Sludges and Slurries*, PNLWTSFG95.12, Pacific Northwest Laboratory, Richland, Washington, April 1995.

$$\dot{\gamma}_w = \frac{4\,(Q - \pi R^2\, V_w)}{\pi R^3}\left(\frac{3}{4} + \frac{1}{4}\,\frac{d\,\ln\,(Q - \pi R^2 V_w)}{d\,\ln\,\tau_w}\right) \tag{4.1}$$

Here, Q is the volumetric flow through the capillary, V_w is the slip velocity, and R is the tube radius. The shear stress at the capillary wall, τ_w, which by convention is positive, is defined by

$$\tau_w = \frac{R}{2}\left(\frac{-\Delta P}{L}\right) \tag{4.2}$$

where $\Delta P/L$ is the pressure drop per length of tubing. The viscosity at the capillary wall is the ratio of the shear stress to the shear rate

$$\eta_w = \frac{\tau_w}{\dot{\gamma}_w} \tag{4.3}$$

Although the shear rate, and therefore the viscosity, of the material varies over the cross section of a capillary, the capillary rheometer method results in a viscosity measurement at a position (capillary wall) where the shear rate can be determined. To calculate the viscosity as a function of shear rate, a log-log plot of pressure drop (plotted as τ_w) as a function of flow rate is developed. The slope is determined at each flow, giving the last term in Equation 4.1 (assuming $V_w = 0$), and the shear rate is determined with Equation 4.1. The viscosity is then determined with Equation 4.3. To determine these slopes and $\dot{\gamma}_w$, we use a modification of the numerical algorithm described previously (Gauglitz et al. 1994b). The improved algorithm is described in Appendix B with an example that compares the numerical algorithm with an exact analytic solution. We assume the slip velocity is zero ($V_w = 0$) for the data we analyze in the following sections (see the results section (4.3) for a discussion of how neglecting wall slip affects the reported viscosity data).

4.2 Experimental Method and Materials

4.2.1 Apparatus and Procedure

Figure 4.1 gives a schematic of the capillary rheometer apparatus for measuring the viscosities of bubbly slurries. The apparatus consists of a flow loop with connections for measuring the pressures at the inlet and exit of the loop and a pump that controls the flow of the bubbly slurry. The flow loop also includes transparent cells for observing the bubbly slurry. A detailed description of this apparatus can be found in Gauglitz et al. (1994b). For bubbly slurry experiments, we used tubes with diameters ranging from 0.635 to 1.27 cm ID (3/8–5/8 in. nominal size) and lengths from 83 to 305 cm. The tube diameters were confirmed by completely filling the tubes with water and weighing the resulting system. The tubes were made of clear polyvinyl chloride (PVC), which allowed the bubbles to be viewed within the tubes. Pressures on the inlet and outlet of the tube were measured using one absolute pressure transducer (Paroscientific model 245a-101) with a range of 0–310 kPa (0–45 psia) and a 0.01% accuracy (0.0045 psia) traceable to NIST standards. The accuracy of the pressure difference is 62 Pa (0.009 psia).

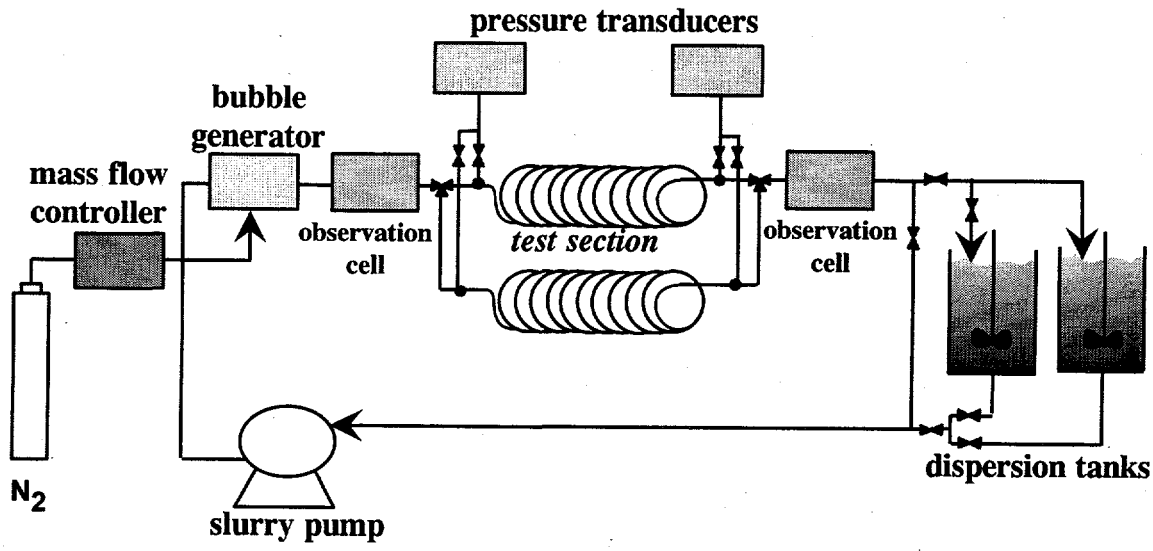

Figure 4.1 Capillary Rheometer Apparatus for Measuring the Viscosity of Bubbly Slurries

The pressure transducer was connected to a Digiquartz Pressure Computer, which included a temperature compensation feature as part of the pressure transducer calibration. The capillary rheometer apparatus was automated for data acquisition and control with LabVIEW® for Windows™ software operating on a 486 PC.

The procedure for conducting an experiment was to first fill the inlet of the pump cavity with a bubbly slurry, then slowly pump the slurry through the tubes of the rheometer. Pumping the fluid too rapidly caused extraneous gas bubbles to be pumped into the lines. Once the bubbly slurry was fully contained in the lines, the flow loop was closed and viscosity measurements initiated. The closed loop recirculation kept the intentionally entrained gas bubbles from escaping. For each bubbly slurry, the pump was adjusted to span the desired range in flow. At each flow, the pressure difference across the flow loop was measured for approximately 5–6 minutes before adjusting the flow to a new setting. The test fluid was displaced through the test section with a progressing cavity pump (Robbins & Meyers Moyno, single screw rotary pump) capable of delivering 1.2 mL/s. The pump was driven with a ¼ hp dc electric motor rated for 1725 rpm at 90 VDC and attached to a 50:1 gear reducer. All experiments were conducted at ambient temperature, which typically ranged from 20 to 27°C.

Prior to making viscosity measurements, the flow delivered by the slurry pump through the rheometer system was calibrated over a range of revolutions per minute (rpm) settings. (The pump was equipped with a speed controller that maintained the pump at selected rpm settings.) The fluid at each setting (rpm) was collected for a period of time in a graduated cylinder and weighed. Assuming a density of 1.0 g/mL for water and a measured density of 1.14 g/mL for the 66 wt% glycerol/34 wt% water solution, the flow delivered by the pump was linear with rpm setting.

4.2.2 Test of the Capillary Rheometer

To test the capillary rheometer and our procedures, we first measured the viscosities of Newtonian fluids–water and mixtures of water and glycerol. The viscosity of the 66 wt% glycerol in 34 wt% water mixture was measured for a range of shear rates on the capillary rheometer and a conventional rotational viscometer (Haake M5 system, RV-20 controller, MV-2 probe assembly). The viscosity of a Newtonian fluid does not depend on shear rate, and the capillary viscometer gave a constant viscosity of 0.02 Pa*s (20 cP) for the glycerol water mixture over a shear rate range of 40 to 400 s^{-1}. Appendix C gives the data from the capillary rheometer. The rotational viscometer gave viscosities that ranged from 0.017–0.020 Pa*s (17–20 cP) for an identical mixture for shear rates between 30 and 140 s^{-1}, which agrees well with the capillary rheometer results. This test confirmed that the capillary rheometer was operating correctly.

4.2.3 Bubbly Slurry Preparation

In all the slurry experiments, a mixture of 66 wt% glycerol in 34 wt% water was used as the suspending fluid. This mixture had a 0.02 Pa*s viscosity (20 cP) and was chosen to be representative of the supernatant liquid in double-shell tank (DST) waste, such as that of Tank 241-SY-101 (Tingey et al. 1994). For the solid phase, 71 μm PMMA particles (1.21 g/mL) were used because of their nearly neutral buoyancy in the supernatant liquid (1.14 g/mL) and because many slurry particles in real waste are of similar size. Real tank waste, of course, contains a very wide range of particle sizes, and micron-size particles are common.

Bubbly slurries were made for viscosity testing by mixing high-gas-fraction foams (up to 90 vol% gas in liquid) into a stock slurry (typically 58 vol% particles). By adjusting the gas fraction of the foam being mixed with the stock slurry, bubbly slurries could be prepared with a range of gas and particle fractions. Stock slurries were built by slowly adding known volumes of PMMA particles to 66 wt% glycerol/34 wt% water supernatant liquid stock solution. By carefully mixing the PMMA particles with the glycerol/water mixture, we produced a stock slurry generally containing less than 2 vol% gas (which was accounted for in slurry preparation). Adding approximately 0.2 vol% Triton X-100 surfactant to the glycerol/water solution allowed the liquid to wet the PMMA particles better, causing less gas to be entrained in the slurry. Stock slurries were prepared in batches of one gallon to ensure well-characterized and reproducible bubbly slurries. Bubbly slurries with less than 16 vol% gas were prepared from a stock slurry of less than 2 vol% gas. When preparing bubbly slurries with gas content higher than 16 vol%, high-gas-fraction stock slurries were used. These slurries were prepared by vigorously adding solids to the liquid, an action that entrained additional gas between the particles and thus increased the gas content of the stock slurry. During our tests, we mixed stock slurry compositions up to 12 vol% gas.

Figure 4.2 depicts the apparatus for creating the high-gas-fraction foams for mixing with the PMMA particles. A mass flow controller metered nitrogen, and a syringe pump delivered the glycerol/water solution to an inline mixer. This mixer created gas bubbles with diameters of approximately 50–150 microns. The bubbles were stabilized by adding approximately 1 wt% Joy® detergent. The foams of desired gas fraction were injected below the surface of the stock slurry and mixed. The gas content in the stock slurries was monitored daily since gas bubbles were observed to escape from the stock slurry.

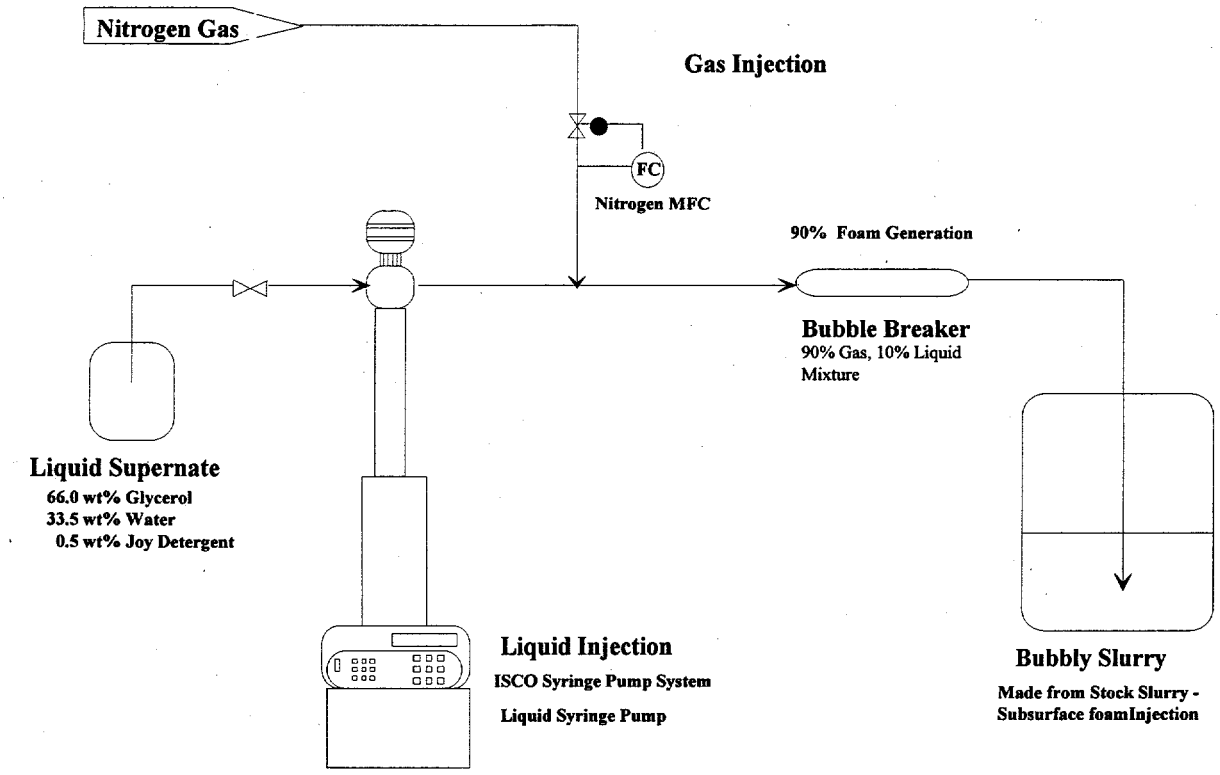

Figure 4.2. Apparatus for Generating Bubbly Slurries

4.2.4 Gas Content Measurement

To check the consistency of the bubbly slurries, the actual gas content and density of each slurry were measured before and after flow tests with the rheometer. The density was determined by collecting a slurry sample of known volume in a graduated cylinder and measuring its mass. The gas content of the slurries was calculated from these density measurements.

For direct measurement of the gas content, a change in slurry volume was measured by dislodging and removing the gas bubbles from the slurry. Graduated cylinders containing bubbly slurries were placed in a vacuum desiccator and periodically tapped. For thick slurries with greater than 46 vol% solids, a known volume of water was added to thin the slurry. In most cases, a wet foam with small bubbles rose to the top of the slurry, and a few drops of antifoaming agent were added to cause these bubbles to coalesce. The difference in slurry volume with and without bubbles was used to calculate the gas fraction as follows:

$$\phi_g=(V_2-V_1)/V_i \tag{4.4}$$

where ϕ_g is the fractional gas content in the slurry, V_1 is the volume of slurry after gas removal (but after water addition, if necessary), V_2 is the volume of slurry before gas removal (but after water addition, if necessary), and V_i is the initial slurry volume before gas removal and water addition. The reported gas content for each sample is based on this measurement.

4.2.5 Experimental Design

Two groups of viscosity experiments were performed to investigate the effects of gas bubbles and solid particles on the viscosities of bubbly slurries. The selection of experiments was based on the Concentrated Bubbles-as-Particles Suspension Model described by Gauglitz et al. (1994b). For this model, the predicted relationship between the slurry viscosity η and the particle loading and gas content is given thus:

$$\frac{\eta}{\eta_f} = \left(1 - \frac{\phi_p}{\phi_m}\right)^{\frac{-5\phi_m}{2}} \left(1 - \frac{\phi_g}{(1-\phi_p)}\right)^{-\frac{5}{2}} \tag{4.5}$$

where η_f is the viscosity of the suspending fluid, ϕ_p is the particle volume fraction, ϕ_m is the maximum packing fraction (Barnes et al. 1989), and ϕ_g is the volume fraction of gas bubbles. Equation 4.5 is expected to be valid for dilute slurries and slurries with both high particle fractions (ϕ_p near ϕ_m) and gas fractions (ϕ_g near 1- ϕ_p). The first group of experiments, which is listed in Table 4.1, maintained a constant solids fraction and varied the gas fraction. Accordingly, the first term on the right side of Equation 4.5 was constant, and only the gas bubble term varied. In the second group of experiments, which is listed in Table 4.2, the solid particle fraction was varied. The gas fraction was also adjusted to keep the second group of terms on the right side of Equation 4.5 constant. As we will see in the following sections, the data suggest that the exponent on the gas fraction term in Equation 4.5 depends on shear rate.

4.3 Results and Discussion

Figure 4.3 shows the viscosity results for the group of experiments in which the effect of gas fraction was investigated; each subplot presents data for a different gas fraction. The actual pressure and flow rate data and the calculated values of viscosity and shear rates are given in Appendix C. In Figure 4.3A to E, the slurry viscosity without gas bubbles is shown for reference. The lines through the data are from the correlation that is developed in the following section. As shown in Table 4.1, these tests were performed at a constant particle content. The results show two important effects. First, the viscosity of the bubbly slurry increased with the addition of gas bubbles. For the highest gas fraction, 20 vol%, the bubbles increased the viscosity about seventy-five-fold at the lower shear rates. Because each of these experiments had 48 vol% particles, the volume of liquid within the slurry decreased as the gas fraction increased. Increased viscosity with increased gas fraction was expected based on the bubbles-as-particles model given in Section 4.2.5.

Table 4.1. Bubbly Slurry Viscosity Tests at 48 Vol% Solids Fraction

Solids Content Vol%	Gas Content Vol%	Liquid Content Vol%	Tube Dimensions
48%	0%	52%	0.635 cm ID, 302 cm long
48%	5%	47%	0.635 cm ID, 302 cm long; 0.952 cm ID, 254.2 cm long
48%	12%	40%	0.635 cm ID, 302 cm long; 0.952 cm ID, 254.2 cm long
48%	16%	36%	0.635 cm ID, 302 cm long; 0.952 cm ID, 254.2 cm long 1.27 cm ID, 305 cm long
48%	18.2%	33.8%	0.635 cm ID, 302 cm long; 0.975 cm ID, 254.2 cm long
48%	20%	32%	0.952 cm ID, 254.2 cm long; 1.27 cm ID, 305 cm long

Table 4.2. Bubbly Slurry Viscosity Tests with Varying Particle Fraction

Solids Content Vol %	Gas Content Vol %	Liquid Content Vol %	Tube Dimensions
38%[(a)]	23%[(a)]	39%	0.635 cm ID, 302 cm long; 0.952 cm ID, 254.2 cm long[(b)]
43%	18%	39%	0.635 cm ID, 302 cm long; 0.952 cm ID, 254.2 cm long[(b)]
46%	17%	37%	0.635 cm ID, 302 cm long; 0.952 cm ID, 254.2 cm long
48%	16%	36%	0.635 cm ID, 302 cm long; 0.952 cm ID, 254.2 cm long 1.27 cm ID, 305 cm long
50%	17%	33%	0.635 cm ID, 82.6 cm long; 0.952 cm ID, 123.2 cm long

(a) Too much gas was added to the slurry mixture; desired composition was 40% solids, 19% gas, 41% liquid.
(b) Data collected on 0.952 cm tubes are not reported because the bubbles completely separated from the slurry and collected at the top of the tube.

The second characteristic of the viscosity data is that the slurry is shear thinning, and the degree of shear thinning increased with gas bubble content. For example, the viscosity of the slurry at the lowest gas content, 5 vol%, increases with decreasing shear rate, but the increase is not very large. At 20 vol%, the viscosity increases dramatically with decreasing shear rate. The bubbles-as-particles model given in Section 4.2.5 does not give any shear rate dependence and thus needs modification. The yield stress was also estimated by extrapolating the wall shear stress (see Eq. 4.3) to zero shear rate. The estimated yield stresses for the slurries are quite small; the largest yield stress of 4 Pa $\pm$ 4 Pa was estimated for the slurry with 20% gas and 48% particles.

Figure 4.4 shows the effect of the solid particle fraction on the viscosity of bubbly slurries, and each subplot shows data for a different particle fraction. In these experiments, the gas fraction was varied slightly to keep the second term on the right side of Equation 4.5 constant. Again, the lines through the data in Figure 4.4 are from the correlations developed in the following section. The results show that the viscosity increases with increasing particle fraction, although the range in particle fraction for this group of experiments was rather narrow. While the viscosity data for the bubbly slurry with 43 vol% particles shown in Figure 4.4A does not show shear thinning behavior, the majority of the data show shear thinning for those bubbly slurries. This agrees with the results shown in Figure 4.3

The viscosity measurements were performed with tubes of different diameters to allow a wide range of shear rates to be investigated. As seen in Figures 4.3 and 4.4, the viscosities measured with different diameter tubes are not identical. Generally, the larger-diameter tubes gave higher viscosities than the smaller tubes, which is an indication of wall slip or that some other diameter-dependent mechanism is affecting the viscosity measurements (see Gauglitz et al. [1994b] and Macosko [1994]) for discussions of wall slip). In the presence of wall slip, which becomes more important in smaller-diameter tubes, the measured viscosity is less than the actual viscosity; this agrees with the smaller tubes having lower measured viscosities. While it is likely that the bubbly slurry had an appreciable wall slip, bubble separation also occurred to a greater extent in the larger-diameter tubes despite the efforts to avoid this. This bubble separation may also explain the viscosity measurements being affected by the tube diameter. Our attempts to determine wall slip following the formal procedure of Mooney (1931) (see also *Macosko*, 1994) have not been successful, and the reason for this is unclear. Again, bubble segregation is a possible cause of the problem. Because we have not corrected the viscosity data for both wall slip and bubble segregation, the measured viscosities are apparent viscosities.

4.4 Correlations of Bubbly Slurry Rheology

A variety of relationships can be used to represent the data in Figures 4.3 and 4.4. In a recent report, Mahoney and Trent summarized a large number of possible models.[a] Although the focus of their rheological correlations was particulate slurries, many of the reported correlations could be modified to include the effect of gas bubbles. However, Equation 4.5 gives a functional form for the effect of gas bubbles on viscosity.

(a) Mahoney, L. A., and D. S. Trent. April 1995. *Correlation Models for Waste Tank Sludges and Slurries*. Letter Report PNLWTSFG95.12, Pacific Northwest Laboratory, Richland, Washington.

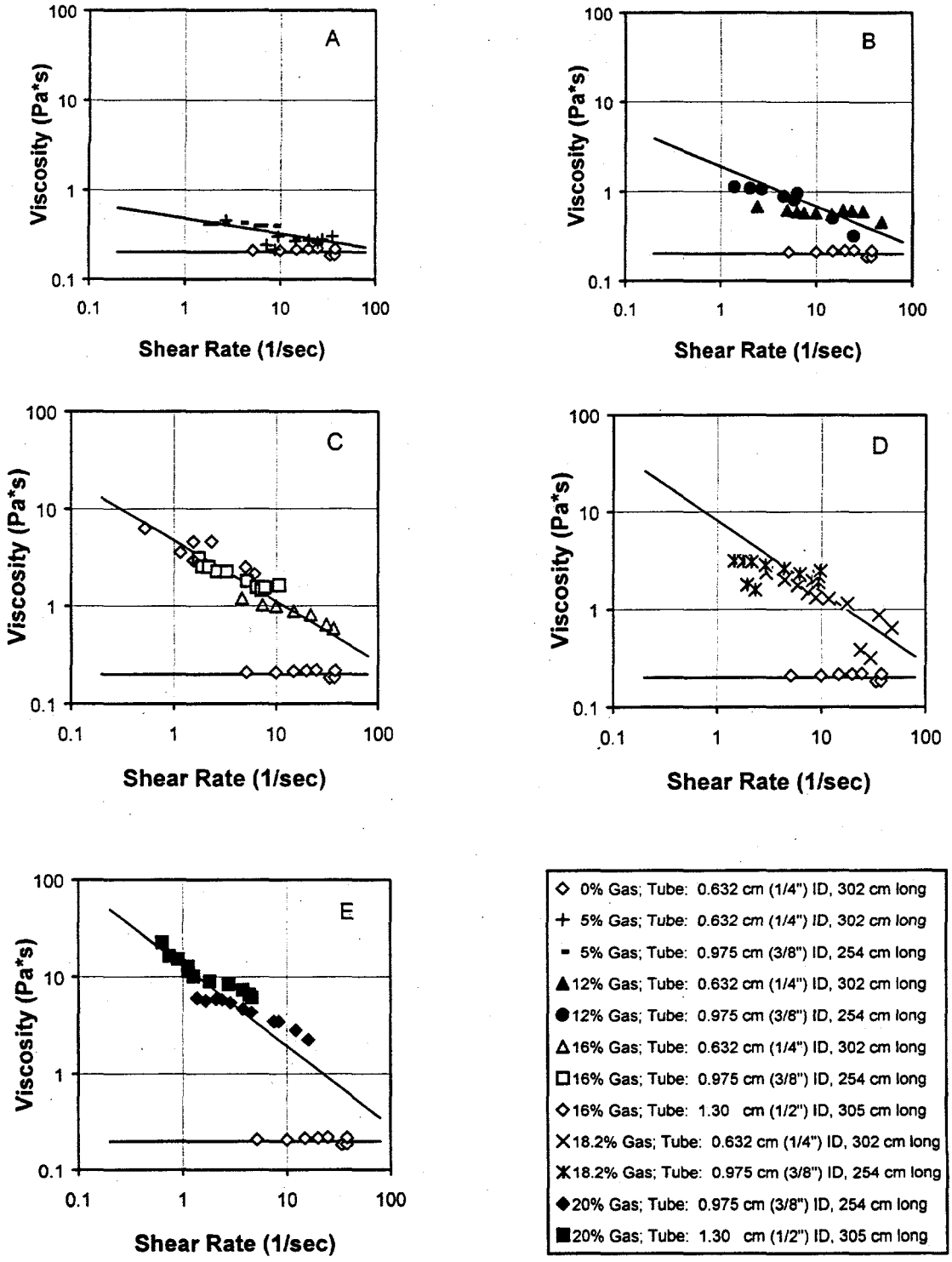

Figure 4.3. Effect of Gas Volume Fraction on the Viscosity of a Slurry Containing 48 Vol% PMMA Particles (the lines are from the correlation developed in Section 4.4)

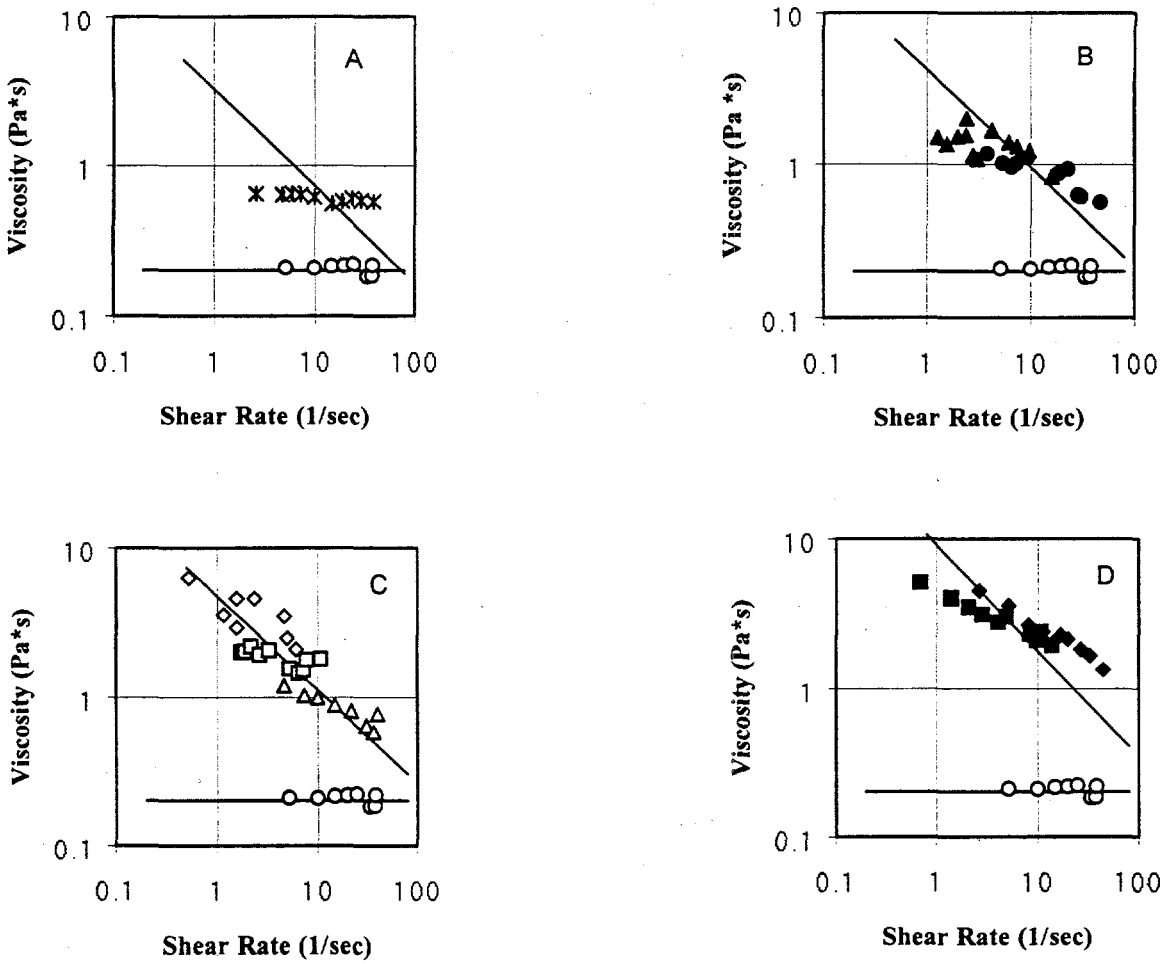

○	0% Gas, 48% Solids; Tube: 0.975 cm (3/8") ID, 302 cm long
✱	18% Gas, 43% Solids; Tube: 0.632 cm (1/4") ID, 302 cm long
●	17% Gas, 46% Solids; Tube: 0.632 cm (1/4") ID, 302 cm long
▲	17% Gas, 46% Solids; Tube: 0.975 cm (3/8") ID, 254 cm long
△	16% Gas, 48% Solids; Tube: 0.632 cm (1/4") ID, 302 cm long
□	16% Gas, 48% Solids; Tube: 0.975 cm (3/8") ID, 254 cm long
◇	16% Gas, 48% Solids; Tube: 1.295 cm (1/2") ID, 305 cm long
◆	17% Gas, 50% Solids; Tube: 0.975 cm (3/8") ID, 83 cm long
■	17% Gas, 50% Solids; Tube: 1.295 cm (1/2") ID, 123 cm long

Figure 4.4. Effect of Solid Particle Volume Fraction on the Viscosity of a Bubbly Slurry (the lines are from the correlation developed in Section 4.4)

As mentioned in Section 4.3, bubbly slurries are shear thinning; and the viscosities depend on shear rate. To develop a correlation for the data in Figures 4.3 and 4.4, the Bubbles-as-Particles Suspension Model (see Equation 4.5) was then modified to include shear thinning as follows:

$$\frac{\eta}{\eta_f} = \left(1 - \frac{\phi_p}{\phi_m}\right)^{\frac{-5\phi_m}{2}} \left(1 - \frac{\phi_g}{(1 - \phi_p)}\right)^{-f(\dot{\gamma})} \tag{4.6}$$

where the shear rate dependence is included in the exponent on the term representing the gas bubble contribution. By selecting a suitable form for this exponent, the data in Figures 4.3 and 4.4 can be reasonably represented. Tables 4.3 and 4.4 show the reduced viscosity (η/η_f) for a number of shear rates. These viscosity values were taken from lines drawn through the data in Figures 4.3 and 4.4. The exponent $f(\dot{\gamma})$ that best fit the data was determined at each shear rate, and the following form for the exponent was found to give a reasonable model for the effect of shear rate:

$$f(\dot{\gamma}) = A + B\ln(\dot{\gamma}) \tag{4.7}$$

An interesting aspect of using the shear rate dependence in Equation 4.7 is that the shear rate dependence is equivalent to that for a power-law fluid without a yield stress. That is, a log-log plot of viscosity versus shear rate is a straight line, and the slope of the line depends on the constant B.

To apply the correlation given by Equations 4.6 and 4.7, the following parameters must be specified or determined:

η_f = suspending fluid viscosity
ϕ_m = maximum packing fraction
A = fitting parameter
B = fitting parameter

Table 4.3. Effect of Gas Fraction on the Viscosity of Bubbly Slurries at Specific Shear Rates (slurries contained 48 vol% particles)

Gas Content	Reduced Viscosity (η/η_f) at Particular Shear Rates					
	1 sec^{-1}	3 sec^{-1}	5 sec^{-1}	8 sec^{-1}	10 sec^{-1}	20 sec^{-1}
0 vol%	10	10	10	10	10.5	11
5 vol%	21	20	20	17.5	16	15.5
12 vol%	56	45	35	32.5	30	30
16 vol%	160	120	100	75	75	40
20 vol%	750	350	250	175	150	100

Table 4.4. Effect of Particle Fraction on the Viscosity of Bubbly Slurries at Specific Shear Rates

Solids Content	Reduced Viscosity (η/η_f) at Particular Shear Rates					
	1 sec^{-1}	3 sec^{-1}	5 sec^{-1}	10 sec^{-1}	20 sec^{-1}	40 sec^{-1}
38 vol%	25	25	24	22.5	22.5	20
43 vol%	33.5	34	33.5	30.5	28.5	30
46 vol%	85	75	65	50	40	30
48 vol%	200	105	85	65	42.5	30
50 vol%	235	175	165	115	95	75

Generally, the suspending fluid viscosity and maximum packing fraction are either known or can be measured. Thus, only the two constants A and B need to be determined.

The Bubbles-as-Particles Suspension Model given by Equations 4.6 and 4.7 was fit to the data given in Figure 4.4. The parameter values that best fit the data are $A = 8.606$ and $B = -1.708$, with the measured value of $\eta_f = 0.02$ Pa*s, and $\phi_m = 0.62$. The measured value of ϕ_m was 0.65, and the slight adjustment of ϕ_m was made to fit the viscosity data for the bubble-free slurry with 48 vol% particles. The best fit parameters were determined using a multivariable nonlinear least square technique provided in the software package Macsyma®. For the best fit parameters A and B, χ^2 test of the fit was 0.596. The lines shown in Figures 4.4 and 4.5 are generated with the correlation given by Equations 4.6 and 4.7 and the constants given above. As seen in the figures, the correlation is typically within a factor of two of the data and represents the effect of gas and solid content on slurry viscosity fairly well. A notable discrepancy is apparent in Figure 4.4, particularly in 4.4A, 4.4B, and 4.4D, where the slurries are less shear thinning than predicted by the correlation. The cause of this consistent difference is not known. Figure 4.5 summarizes the predicted viscosities for a bubbly slurries with 48 vol% particles and a range of gas fractions. This figure gives a direct comparison to highlight how the viscosity increases with increasing gas fraction and how the bubbly slurries become more shear thinning with increasing gas fraction.

An alternative approach to correlating the data is to model the shear thinning behavior. For example, the biviscous or power law models described by Mahoney and Trent[(a)] could be used by allowing the fitting parameters to depend on the particle and gas fractions.

(a) Mahoney, L. A., and D. S. Trent. April 1995. *Correlation Models for Waste Tank Sludges and Slurries*. Letter Report PNLWTSFG95.12, Pacific Northwest Laboratory, Richland, Washington.

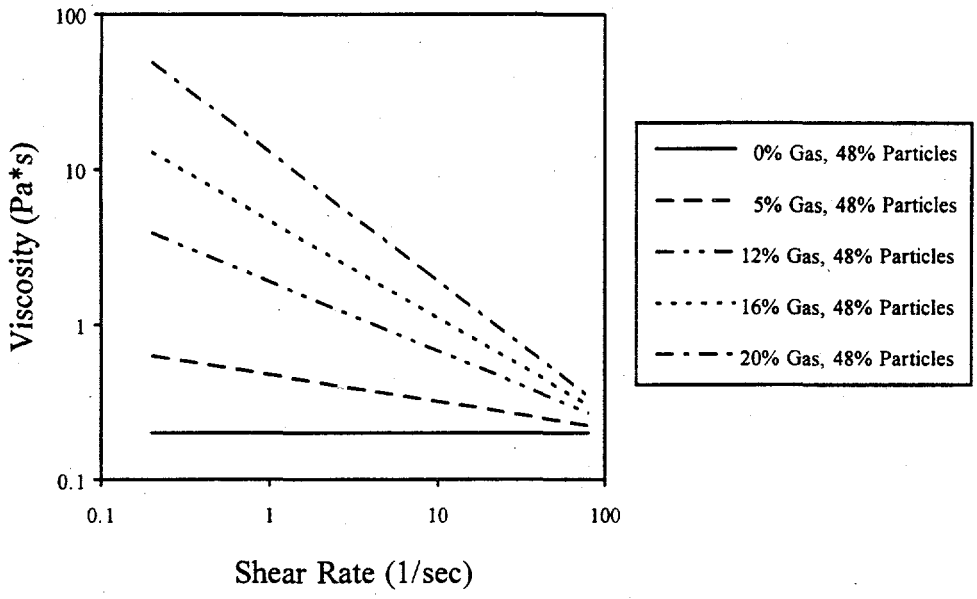

Figure 4.5. Predicted Viscosity for a Bubbly Slurry Using the Correlation given by Equations 4.6 and 4.7 with A = 8.606, B = -1.708, η_f = 0.02 Pa*s, and ϕ_m = 0.62 (the bubbly slurry has 48 vol% particles and a range of gas fractions)

5.0 Shear and Tensile Strengths of Bubbly Slurries

This section describes experiments performed to determine the relationships between shear strength, tensile strength, and bubble morphology for different types of sludge simulants. A technique for measuring the tensile strength of sludge-like materials was identified and a prototype tensiometer constructed. Brief discussions of the tensile and shear strength measurement techniques and the simulants used are given below. Following this discussion, the results of the testing are presented.

The shear strength and tensile strength data presented in Section 5.3 are generally consistent with those cited by Gauglitz et al. (1994a). Increases in the water content (below saturation) of simulants bonded by pendular and capillary forces were observed to result in increases in both shear and tensile strengths. Increasing the gas content of cohesive simulants resulted in proportional decreases in shear and tensile strengths; this implies that bubble surface tension effects are of relatively minor importance for the cohesive simulants tested.

5.1 Shear and Tensile Strength Measurement Theory

Described in this section are the technical bases for selecting a vertical extrusion technique for tensile strength measurements and a shear vane technique for shear strength measurements. The mathematical relationships between the measurements taken and the computed strengths are also given.

5.1.1 Tensile Strength Measurement

A variety of techniques have been employed for measuring the tensile strength of materials. For many materials (e.g., steel) tensile strength measurement is a relatively simple operation. The opposite ends of a piece of material are gripped and a tensile load applied until failure occurs in a region of the sample that has been purposely thinned. This method cannot always be employed when testing sludge-like materials (e.g., wet soils) because it is difficult to grip the sample ends and shape samples too weak to hold their shapes unsupported. The methods that have been used to measure soil tensile strengths can be conceptually divided into direct and indirect tests, and they are described in the following paragraphs.

5.1.1.1 Direct Tensile Testing

Direct tensile strength measurements are similar to the techniques used to measure the tensile strength of standard construction materials. That is, opposite ends of a sample of known dimensions is subjected to a pulling force that results in the separation of the sample into two halves. The force required to induce failure divided by the area over which the failure occurred equals the tensile strength.

The major obstacles to the successful use of a direct tensile test are the difficulties of gripping the sample ends and of avoiding imposing a nonuniform stress field on the sample (Al-Hussaini and Townsend 1973). Several techniques have been attempted for attaching the force application mechanism to the ends of soil samples. Hasegawa and Ikeuti (1966) used hooks embedded in the sample as it was prepared. The exposed ends of the hooks were connected to the force application mechanism. Thorne et al. (1980) used wax that was allowed to permeate into the sample a few centimeters to provide an adhesion between the sample and the metal plates of the tensiometer. Several researchers (Ajaz and Parry

1974; Tschebotarioff et al. 1953; Bishop and Garga 1969) have chosen to carefully fashion their samples into hourglass-like shapes that could be gripped by clamps at the ends. The hourglass shape results in the tensile failure occurring within the thinned region of the sample rather than near the gripping clamps.

In addition to the end-gripping problem, direct tensile strength measurements on soils is complicated by the sensitivity of the test to any misalignment of the applied tensile stress with the sample axis. Misalignment induces bending moments within the sample that concentrate the tensile stresses in one region, which can result in the measured tensile strength being significantly lower than that measured in the absence of bending moments. Most direct tension devices are designed to minimize the opportunity for sample misalignment, but it is difficult to eliminate. Hasegawa and Ikeuti used a self-aligning design that involved floating the sample being tested in a pool of liquid mercury. A sketch of their device is shown in Figure 5.1. This approach was not considered for the present testing due to concerns about the health hazards of mercury.

Another technique for performing a direct tension measurement is known as vertical extrusion. This is the method that was used to generate the tensile strength data given in this report. The vertical extrusion method involves extruding a cylindrical segment of sample vertically downward until failure occurs (Figure 5.2). The mass of the piece that breaks free (M_v), gravitational acceleration (g), and the tube diameter (D_t) are used to calculate the tensile strength directly using the equation:

$$S_t = \frac{4 M_v g}{\pi D_t^2} \tag{5.1}$$

Advantages of this technique are that the need for an end-gripping mechanism is eliminated and the forces applied to the sample are primarily tensile (i.e., the applied force is axially downward and perpendicular to the expected failure plane). No assumptions about the elastic stress-strain behavior of the sample need to be made.

The vertical extrusion method is limited in the range of tensile strengths it can measure. As the tensile strength of the material being tested is increased, the length of sample that must be extruded before failure occurs increases in direct proportion. For this reason, the vertical extrusion method is limited to the measurement of tensile strengths less than about 20 kPa (200 kdyne/cm^2). A sample with a tensile strength of about 20 kPa will need to be extruded to a length of 1-1.5 m to induce failure. If the material is too weak, the length of extruded material at failure is short, which limits the vertical extrusion method to tensile strengths larger than about 5 kdyne/cm^2. Other limitations of the vertical extrusion method include susceptibility of the sample to drying in the air as it is extruded, possible sample disruption from wall friction, and bending moments that result when the extrusion is not perfectly vertical.

Measuring tensile strength with the vertical extrusion approach was selected for this study in part because of the adaptability of this technique to hot cell use. Tank waste samples are routinely extruded horizontally into pans in the hot cell. This design of the hot cell sample extruder will require modification to accommodate vertical extrusion, prevent splashing, and measure the mass of the piece that breaks free. The extent and cost of the required changes have yet to be evaluated.

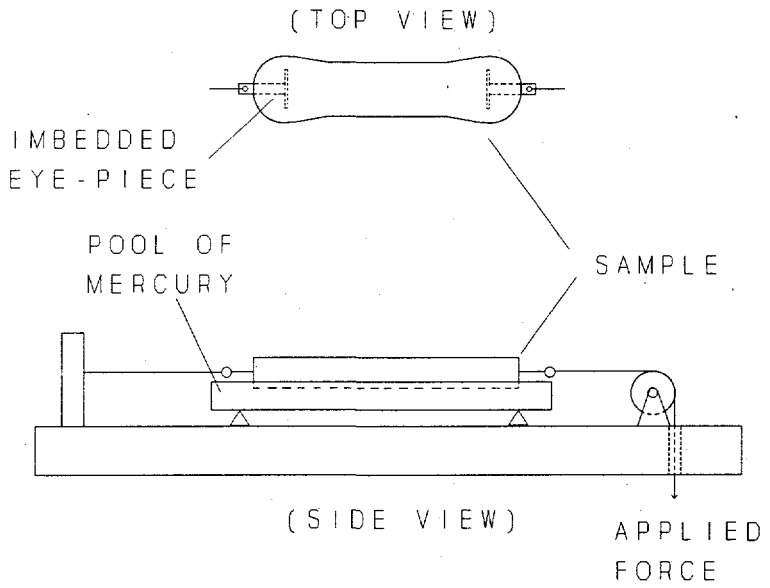

Figure 5.1. Tensile Strength Apparatus (Hasegawa and Ikeuti 1966)

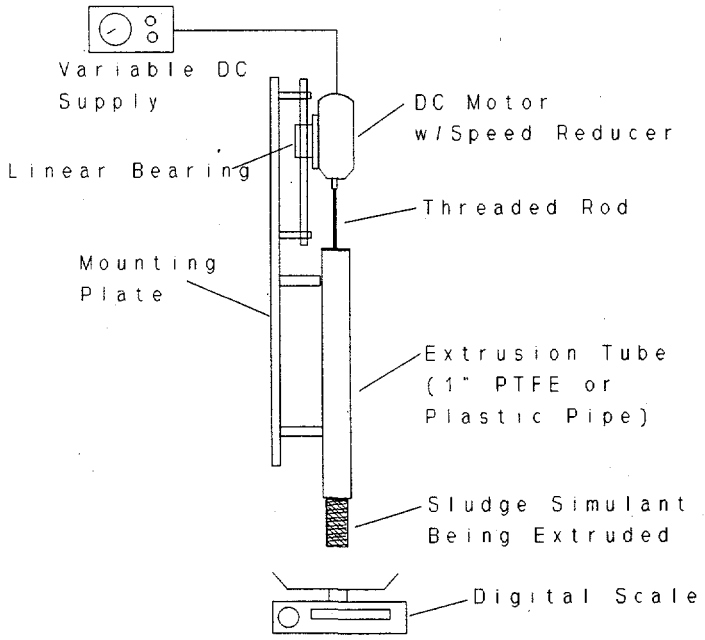

Figure 5.2. Vertical Extrusion Tensiometer Schematic

The vertical extrusion technique for measuring tensile strength should be applicable to materials with the consistency of Hanford tank sludge. Problems may result if there is significant disruption of the sample as it is removed from the tank or as it is pushed out of the core sampling extrusion tube. The sludge simulants used in this test program are relatively insensitive to these types of disruptions, so it is not expected that sample disruption affected the measured shear and tensile strengths.

The primary advantage of the direct tension measurements over the indirect methods is that no assumptions need be made about the stress-strain behavior of the sample. The tensile strength is easily calculated based on the force required to induce failure and the area of the failure plane. For this reason, a direct tension measurement is the preferred method of tensile strength measurement when working with samples of unknown stress-strain behavior. Tank sludge is just such a material.

5.1.1.2 Indirect Tensile Testing

The tensile strength of materials can also be determined by measuring the force required to induce sample failure in response to an applied force that is not purely tensile. These techniques usually require that something be known or assumed about the stress-strain relationship of the sample and are often based on the theoretical rather than observed behavior of ideal materials. The stress distributions present in samples undergoing indirect tensile tests are complicated and can include simultaneous tensile, shear, and compressive forces. For this reason, indirect tensile tests must be employed cautiously. For the present testing, it was decided that efforts would be concentrated on the direct vertical extrusion method. If tensile strength measurements on actual waste cannot be obtained from direct methods, it may be necessary to resort to an indirect technique.

5.1.2 Shear Strength Measurement Theory

Shear vanes are routinely used in soil science to measure the shear strength of soils. A multi-bladed vane is inserted into the sample, then a slowly increasing torque is applied to the vane until the sample is no longer able to resist the shear forces along the edges of the vane. At this point the sample fails in shear along a cylinder defined by the top, bottom, and sides of the vane. The torque required to induce failure is recorded and, along with the vane dimensions, is used to calculate the shear strength.

Because the stresses involved are primarily shearing, shear vane tests can be categorized as a type of direct, rather than indirect, shear strength measurement. To estimate the sample shear strength, we assumed that vane insertion results in negligible disruption of the sample and that the failure zone is confined to a narrow region surrounding the cylindrical volume defined by the shear vane rotation. These assumptions hold to varying degrees depending upon the nature of the samples being tested.

Shear vane tests can be performed either with the vane fully submerged or submerged just until the top of the vane is level with the sample surface. Fully submerged testing requires that the vane be inserted to a depth of at least three vane heights below the surface to ensure that the sample shears along the top edge of the vane. As a result of this requirement, fully submerged vane tests require relatively large sample volumes. Smaller volumes can be tested by inserting the vane until its top edge is even with the sample surface. In this case, the sample shears along the vane sides and bottom; the top of the vane makes no contribution to the measured torque. The shear strengths reported in this document were measured by inserting the vane only until the top edge was even with the simulant surface.

The equation that relates peak vane torque to sample shear strength for the case where the vane top is even with the sample surface is derived from a moment balance and is given by Das (1983) as

$$\tau_s = \frac{T_{peak}}{\pi\left(\frac{D_v^2 H_v}{2} + \frac{D_v^3}{12}\right)} \tag{5.2}$$

where D_v is the vane diameter, H_v is the vane height, and T_{peak} is the peak measured vane torque. Heath (1982) has discussed using shear vanes for measuring the shear strength of sludges inside waste tanks.

5.2 Experimental

The simulant preparation and measurement methods used in this study are described in this section. The operation of the vertical extrusion tensiometer is discussed first. Descriptions of the shear strength measurement techniques and the simulant preparation steps are also provided.

5.2.1 Sludge Vertical Extrusion Tensiometer

The vertical extrusion tensiometer consists of a motor-driven plunger assembly, an aluminum mounting plate, and tensiometer tubes approximately 2.64 cm (1.04 in.) in diameter. A schematic of the tensiometer was shown in Figure 5.2. The motor is a variable-speed, dc motor with a speed-reducing gear assembly affixed to the motor output shaft. The reduced-speed output of the gear assembly is connected to a threaded rod, which actuates a rubber plunger vertically downward. The sludge simulant is pushed down through the extrusion tube by the plunger at about 5.3 mm/min for the glass bead simulants and 23.1 mm/min for the bentonite simulants.[a] Once a piece of the extruded simulant detaches and falls into a collection pan, the weight of the detached piece is recorded and used to estimate the tensile strength. The extrusion tube of the sludge tensiometer is shown in Figure 5.3.

As each sample was extruded, the test operator carefully noted the length of the extruded segment. The segment length at failure was recorded along with the mass of the collected segment. Using these data and the known inside diameter of the extrusion tube, it was possible to calculate both the tensile strength of the sample and the average density of the extruded segment. Direct measurements of the segment densities were needed only for the clay-based simulant tests in which the gas content was slowly changing with time. The average pre-extrusion sample density was also calculated from the sample mass and length in the extrusion tube. Figure 5.4 shows a vertical extrusion test in progress.

(a) The glass bead samples were extruded at a slower rate because their apparent tensile strength was expected to increase with increasing extrusion rate. The slow extrusion rate was judged to provide a better measure of the true, static tensile strength. Bentonite simulants were extruded at a faster rate to decrease the time required for testing. Bentonite tensile strengths are not expected to be a strong function of extrusion rate, and tests were performed at slow and fast extrusion rates to verify this.

5.2.2 Sludge Shear Strength Measurements

Shear strength measurements were made using a shear vane. Vane shear strength measurements are routinely used in soil science to quantify the shear strength of soils. Shear vanes have also been used to measure the shear strength of sludge samples from Hanford waste tanks. The shear strengths of the glass bead simulants were measured using a hand-held shear vane identical to that used in a previous study of glass bead simulants (see Gauglitz et al. 1994a). The clay-based simulants required greater sensitivity of torque measurement, so a shear vane attached to a Haake (Karlsruhe, Germany) Rotovisco model M5 viscometer was used for the clay-based simulants.

The shear strength is calculated based on the shear vane dimensions and the peak torque required to initiate vane rotation within the sample. The Haake viscometer was adjusted to rotate the vane at 0.3 rpm, and the hand-held shear vane was turned slowly by hand. For a description of the theory behind shear strength measurements using shear vanes, see Das (1983).

5.2.3 Experimental Method and Materials

Two distinctly different types of sludge simulants were used. The first series of tests was performed using various mixtures of glass beads and water. The water content was varied and the resultant shear and tensile strengths measured. The second test series used a cohesive sludge simulant prepared from bentonite clay, water, and small amounts of hydrogen peroxide. The hydrogen peroxide was used to generate bubbles within the simulant. The shear and tensile strengths of the cohesive simulants were measured in response to changes in gas content and clay weight fraction. The qualitatively different nature of these two types of simulants necessitated differences in the shear and tensile strength measurement techniques. The techniques used to prepare and test each type of simulant are discussed below.

5.2.3.1 Noncohesive Sludge: Glass Bead Simulants

The glass bead simulants were prepared by mixing together carefully weighed quantities of glass beads and water. The glass beads used for this study were of two different size distributions, both obtained from Jaygo, Inc. (Union, New Jersey). The 1- to 60-micron beads have a nominal size of 30 microns, and the 80- to 110-micron beads have a nominal size of 90 microns. The water and beads were mixed by vigorously shaking them inside a plastic container and stirring the mixture with a steel rod.

Once mixed, a portion of the glass bead simulant was packed into the bottom 15 cm (6 in.) of the tensiometer extrusion tube. We had intended to nearly fill the 90-cm extrusion tube with simulant before extruding, but preliminary tests revealed that the glass bead simulant would not extrude when the tube was packed with more than about 20 cm of simulant. This was attributed to the tendency of high-particle-fraction simulants to expand slightly in response to an applied strain. This property, known as dilatancy, caused an increase in the friction between the simulant and the extrusion tube whenever extrusion was attempted. This problem was largely avoided by loading only about 15 cm of simulant into the tube.

Shear strength measurements were made using a hand-held shear vane. A portion of the prepared simulant was first packed into a suitable container before the shear vane was inserted and subsequently twisted.

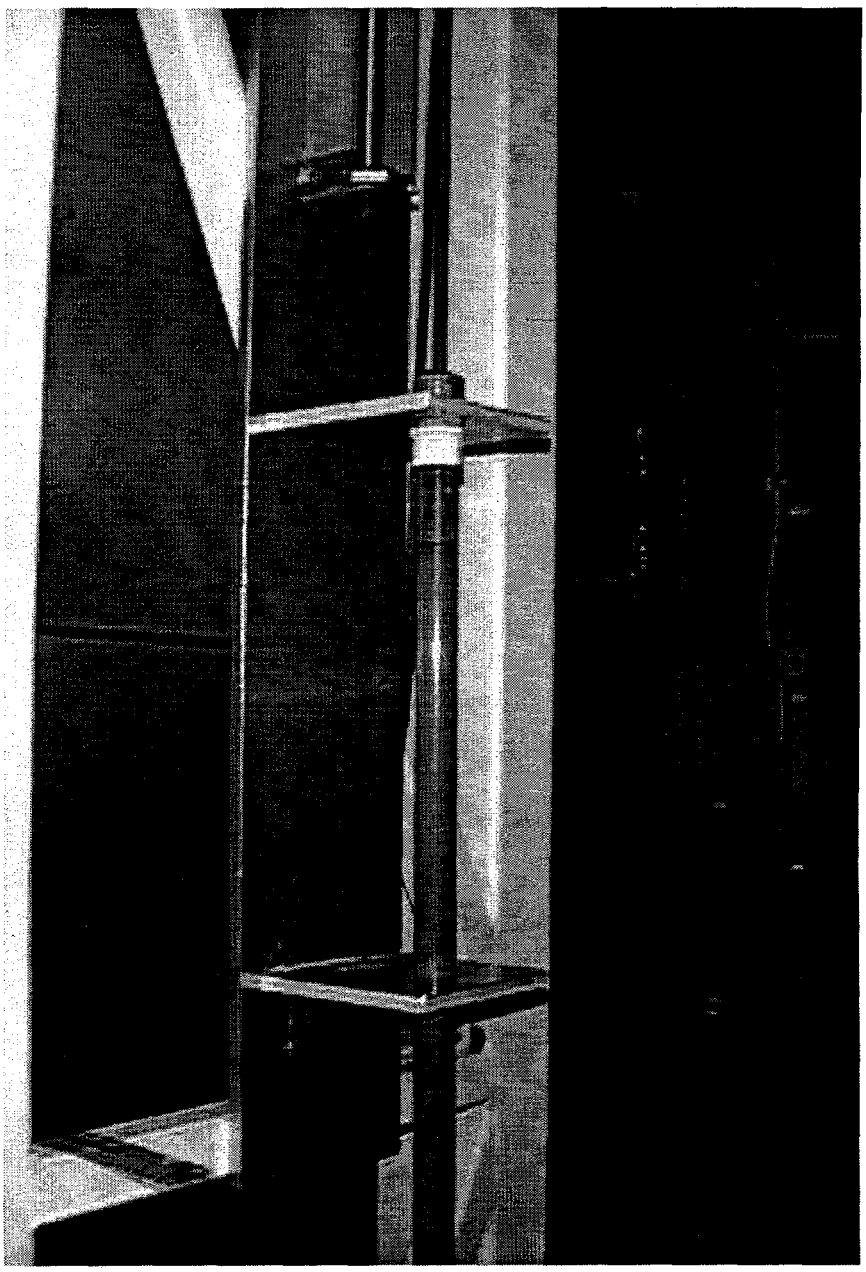

Figure 5.3. Vertical Extrusion Tensiometer

Figure 5.4. Vertical Extrusion Test in Progress

5.2.3.2 Cohesive Sludge: Bentonite Clay Simulants

The cohesive simulant was developed for investigating the shear and tensile strength properties of materials that are held together by colloidal forces between particles rather than interfacial tension and friction, as is the case for the glass bead simulants. Several techniques were considered for creating a clay-based simulant with variable gas content. The decomposition reaction of hydrogen peroxide was ultimately employed because of its simplicity and similarity to tank waste gas generation (i.e., gas is generated uniformly throughout the simulant liquid phase and subsequently collects into small gas bubbles). Dilute hydrogen peroxide solutions are usually quite stable, but the combination of favorable bentonite surface chemistry and high surface area results in nearly complete decomposition over a period of several days (see Schumb et al. 1955).

The cohesive simulants were prepared by mixing the required quantities of water and bentonite clay until a homogenous mixture formed. The required small quantity of 3 wt% hydrogen peroxide solution was then added while mixing continued. After several minutes of mixing, a portion of the simulant was transferred to a large syringe-like device that was used to fill the clear plastic extrusion tubes. Another portion of the simulant was placed into 100-mL plastic beakers for shear strength measurement. The mass of simulant added to the extrusion tube was recorded.

Table 5.1 shows the composition of bubbly clay simulants used in shear and tensile strength experiments. The table indicates the as-is weight fraction of the bentonite clay and the percentage of 3% hydrogen peroxide (H_2O_2) solution. The balance of the mixture was cool tap water. The clay was added to the water and mixed well (15-30 minutes) in a one-gallon-capacity kitchen mixer, after which the H_2O_2 was mixed in for 5–10 minutes. A typical batch mass was about 1800 grams (1500 mL target). The oven-dry weight fractions of clay in the experimental sludges, corrected for the measured clay solids content (92.1% at 443K for 18 hours), are also indicated in Table 5.1. The maximum gas volume percent shown in the table is based on complete conversion of the peroxide (assuming 3 wt% in water) to oxygen gas and liquid water, where the gas-free sludge volume is determined assuming a clay density of 2.72 $\pm$ 0.02 g/mL (Lambe and Whitman 1969) and a water density of 1.0 g/mL. The target gas volume percentages, about 70% of the maximum estimated gas content, were typically achieved two to four hours after H_2O_2 was added to the clay.

As gas generation proceeded over a period of several hours after hydrogen peroxide addition, the volume of the sample within the extrusion tube increased. When the extent of the volume increase indicated that the target gas fraction was met, the shear and tensile strength measurements were conducted simultaneously (or nearly so). Efforts were made to ensure that the shear strength samples (in 100-mL plastic beakers) and the simulant in the extrusion tube were exposed to the same ambient air temperature. This was done to maintain similar rates of gas generation in both the extrusion tubes and the shear strength samples.

Table 5.1. Bubbly Clay Simulant Compositions and Gas Contents

As Is Wt% Clay	Oven Dry Wt% Clay	Wt% H_2O_2 Solution	Maximum Gas Volume %	Target Gas Volume %
17.5	16.1	0	0	0
20.8	19.1	0	0	0
24.0	22.1	0	0	0
27.2	25.1	0	0	0
17.5	16.1	1.03	10.2	7
20.8	19.1	1.02	10.3	7
24.0	22.1	1.00	10.3	7
17.5	16.1	2.01	18.1	13
20.8	19.1	1.96	18.1	13
24.0	22.1	1.86	17.6	13
17.5	16.1	3.00	24.8	18
20.8	19.1	2.93	24.7	18

As a double-check on the sample gas fractions, the length and mass of the extruded segments were recorded during the tensile strength tests. The length was obtained from a measuring tape affixed to the rear side of the extrusion tube (see Figure 5.3), and the mass was determined using a digital balance accurate to $\pm$ 0.02 grams. These data, along with the measured inside diameter of the extrusion tube, allow the direct calculation of the sample density, which, in turn, allows the calculation of the average gas fraction.

5.3 Results and Discussion

The shear and tensile strength data show that the shear strength of the bentonite clay sludge simulant decreases with gas content according to a simple relationship. The clay simulant tensile strength, however, exhibits a stronger and possibly more complex dependence on gas fraction. The shear and tensile strengths of the glass bead simulants are consistent with the expected trends as described by Gauglitz et al. (1994a).

5.3.1 Noncohesive Sludge: Glass Bead Simulants

Shear and tensile strength measurements were obtained for various glass bead samples vigorously mixed with air and water and then packed. At water addition levels less than those required to completely fill the pores in the glass beads (the liquid saturation point), these mixtures mimic dendritic bubbles in sludge.

Figure 5.5 shows the measured shear strengths for 30 μm nominal diameter (1-60 μm range) and 90 μm (80-110 μm range) glass beads as a function of the pore space gas fraction (gas saturation, ϕ_{gs}). The packed 30- μm bead mixtures (at intermediate saturation levels) were found to have a porosity (pore volume/sample volume) of 0.44, and the 90-μm mixtures were about 40% porous. The error bars shown in Figure 5.5 indicate the 95% confidence level (evaluated based on multiple measurements) in strength measurements. The 90-μm bead shear strength data presented in Figure 5.5 are in excellent agreement with the data reported by Gauglitz et al. (1994a) for the same size glass beads. As expected, the peak shear strength of the material increases (from 41 to 83 kdyne/cm^2) as the particle diameter decreases. In similar shear strength experiments with glass beads and silica particles of various sizes, Gauglitz et al. (1994a) scaled shear strength data by the ratio $(\gamma/D_p)^k$, where γ is the liquid/gas surface tension, D_p is the particle diameter, and k is a fitting parameter, and they found that $k \sim 0.7$ gave the best fit to their data. The two data sets depicted in Figure 5.5 are best correlated, by visual observation, with $k \sim 0.6$ and using the glass bead supplier's stated mid-range bead diameters (30 and 95 μm). Since sludge strength is bead-size-dependent, a more rigorous investigation would take into consideration the effects of bead-size distribution. For example, if the predominant size bead in the 1–60 μm sample is 50 μm rather than 30 μm, then the shear strength data in Figure 5.5 would scale simply as $1/D_p$ ($k = 1$). Alternatively, more nearly monodisperse samples could be used in shear strength determinations to better understand the relationship of particle size and sludge strength.

The tensile strengths of 90-μm glass bead/water/air sludges are compared with the shear strengths of similar mixtures in Figure 5.6. Gauglitz et al. (1994a) presented historical tensile strength data for moist agglomerates of limestone and showed that the data were best fit by a function that summed pendular and capillary strength contributions, giving rise to curves with primary and secondary strength maxima. The tensile strength data of Figure 5.6 show this type of behavior. A primary maximum

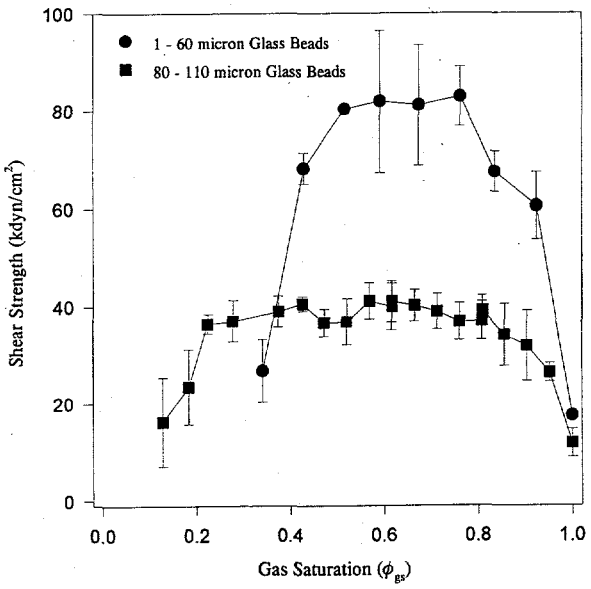

Figure 5.5. Shear Strength Versus Glass Bead Size

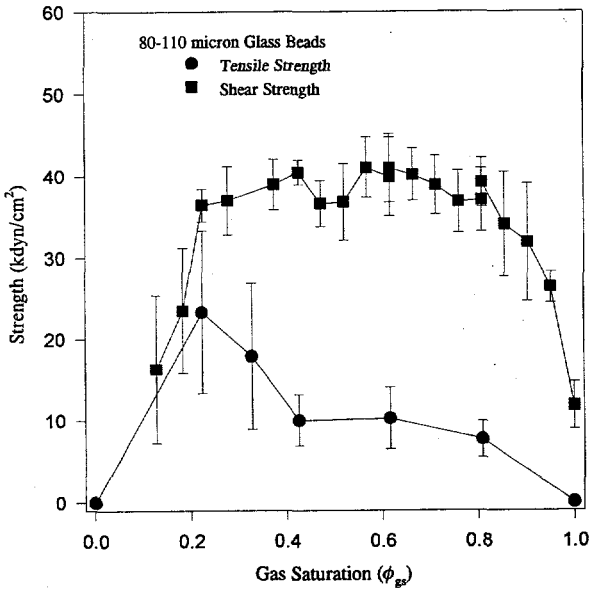

Figure 5.6. Shear and Tensile Strengths of 80-110 Micron Glass Beads

associated with capillary pressure strength appears to occur at a gas saturation of ≤ 0.23. The secondary maximum associated with pendular strength due to liquid bridging is not well defined by the current data but is expected to occur at very high gas saturation (>0.9). Previous investigators (Gauglitz et al. 1994a) suggested that shear and tensile strengths of moist agglomerates might scale by a proportionality constant. The shear and tensile strength data of Figure 5.6 do not support this concept for glass bead sludges, although a much more complete tensile strength data set, particularly at low gas saturation, is needed to better understand the relationship.

The presence of relatively small amounts of gas in the particulate sludge, as shown in Figure 5.6, results in increased sludge tensile strength; at complete liquid saturation of the pore space (0% gas), the tensile strength for the noncohesive beads is expected to be negligible, and at a pore space gas fraction of 0.23, the dendritic bubble sludge had a measured tensile strength of about 23 kdyne/cm^2. In contrast, the tensile strengths of bentonite clay simulants were found to decrease with increasing gas content, as discussed in Section 5.3.2. Thus the effect of gas bubbles on waste strength is dependent on the physical characteristics of the waste.

Tensile strength determination for glass beadpacks by the extrusion technique was found to be experimentally difficult. At high gas content (low liquid saturation), the sample in the extrusion tube apparently compressed radially, increasing the friction between the sludge and the wall. In turn, the sample would often hang up on the wall momentarily and then break free, giving a pulsed extrusion rather than the desired continuous flow. The mechanical shock of this pulsing often gave rise to premature sample fracture. Figure 5.6 includes only the data where the extrude process was essentially continuous rather than pulsed. At the other extreme, sludge of relatively low gas content (<0.3 pore space gas fraction) contained sufficient water to reduce the wall frictional effects to such an extent that the entire sludge pack would often slide out of the tube ahead of the piston face, giving unreasonably high tensile strength readings. These extreme cases were also neglected in the data presented in Figure 5.6. Attempts were made to minimize the wet sample free fall by creating a vacuum resistance within the tube through better sealing between the piston and the tube wall. This technique was sometimes successful.

5.3.2 Cohesive Sludge: Bentonite Clay Simulants

The shear and tensile strengths were measured for each of the cohesive sludge simulants listed in Table 5.1. The data are presented in Figure 5.7 through Figure 5.9 as shear and tensile strengths versus gas fraction. The dependence of both shear and tensile strength on gas fraction appears to be nearly linear over the range tested. However, it is not expected that this linear relationship will continue throughout all higher gas fractions. The lines shown in Figure 5.9, for example, would predict that a sample of this simulant would have zero tensile strength and a 17.7 kdyne/cm^2 shear strength at a gas fraction (ϕ_g) of 0.20. This is clearly unrealistic. It is expected that the slope of the tensile strength versus ϕ_g curve increases (i.e., becomes flatter) as ϕ_g is increased above about 0.15.

The vertical error bars shown on all plots in this section are the estimated 95% confidence intervals for the mean of multiple shear and tensile strength measurements. The horizontal error bars shown represent the estimated 95% confidence intervals for the gas fraction measurements. The shear and tensile strength confidence intervals were estimated based on multiple measurements and the assumption of random, normally distributed errors. The gas fraction confidence intervals were estimated based on a consideration of the expected accuracies of the measurements (sample length, mass, particle density, etc.) used to calculate gas fraction.

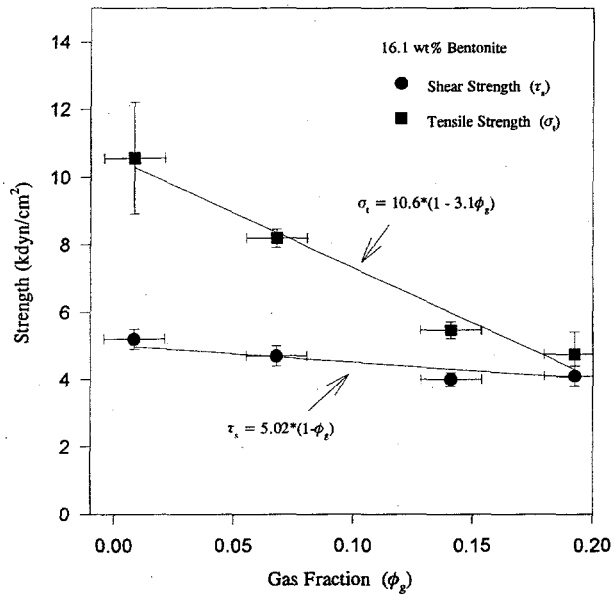

Figure 5.7. Shear and Tensile Strengths Versus Gas Fraction for 16.1 wt% Bentonite

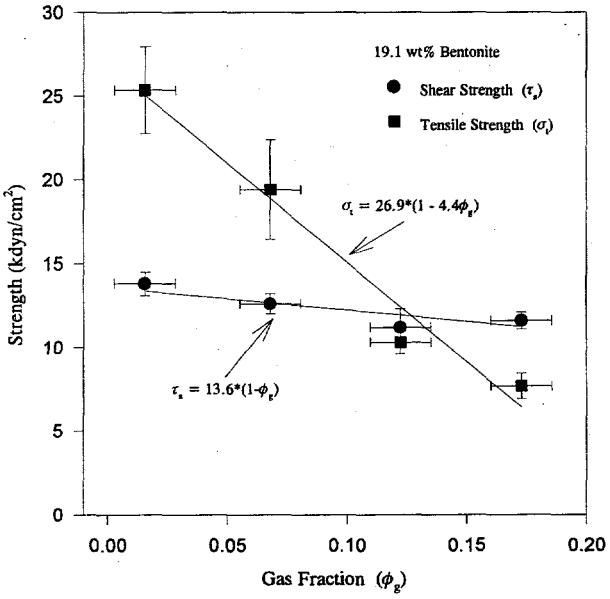

Figure 5.8. Shear and Tensile Strengths Versus Gas Fraction for 19.1 wt% Bentonite

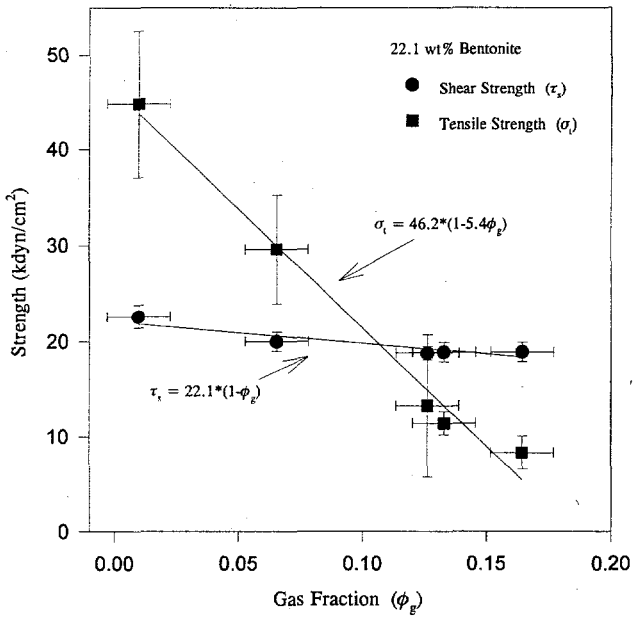

Figure 5.9. Shear and Tensile Strengths Versus Gas Fraction for 22.1 wt% Bentonite

At low gas contents, the sludge simulant tensile strengths were found to be greater than their respective shear strengths. This is consistent with experimental data gathered previously using both vertical extrusion and a split-cell technique to measure tensile strength (Powell 1995b).

The shear-strength versus gas-fraction data are compiled in Figure 5.10. The shear strength data are seen to be reasonably fit by a simple linear relationship. This relationship can be derived starting with the assumption that the shear strength is directly proportional to the fraction of area in the failure plane (i.e., the cylinder defined by the rotation of the shear vane) that is occupied by clay (i.e., not occupied by gas bubbles). It can be shown that a randomly placed intersecting plane that passes through a sludge containing randomly-distributed bubbles of a single size will intersect bubbles such that the fraction of intersecting area that is occupied by gas bubbles is equal to ϕ_g. Thus the fraction of the intersecting area *not* occupied by gas is equal to $1-\phi_g$. The expected relationship between shear strength (τ_s) and gas fraction is

$$\tau_s = (\tau_s|_{\phi=0})(1-\phi) \qquad (5.3)$$

We can see in the plots that the shear strength data for all three bentonite wt% solids concentrations can be fit by this equation.

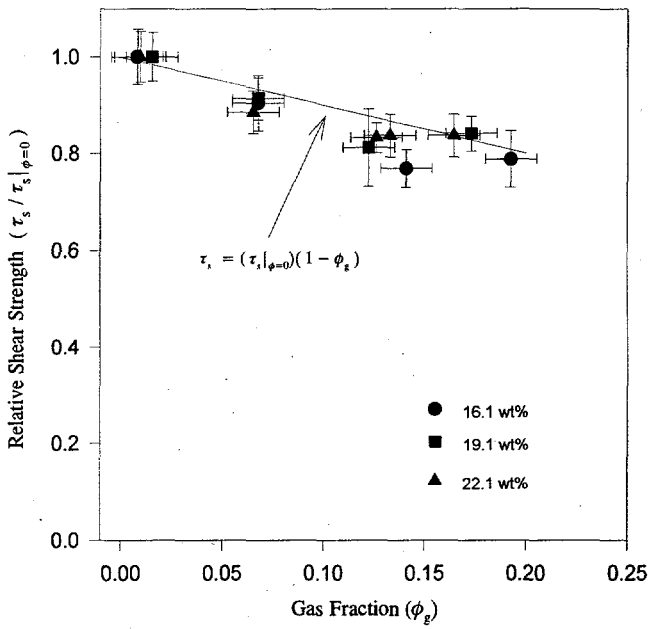

Figure 5.10. Relative Shear Strength Versus Gas Fraction in Clay

The tensile strength data, however, clearly do not follow the same simple relationship. Figure 5.11 shows the dependence of tensile strength on ϕ_g. As ϕ_g increases, the tensile strength decreases in a nearly linear manner. As noted above, this linear relationship is not expected to continue much beyond the highest gas fraction tested (about 0.20). Also evident from the lines shown in Figure 5.11 is the trend of decreasing slope as the wt% bentonite is increased. The slope of the σ_t versus ϕ_g line for the 16.1 wt% simulant is -3.1. The slopes for the 19.1 wt% and 22.1 wt% simulants are -4.4 and -5.4, respectively. If the tensile strength followed the same relationship as shear strength, these slopes would be equal to -1.0. Clearly, the dependence of tensile strength on gas fraction differs from that of shear strength.

A satisfying explanation of the tensile strength data has not yet been developed, but several hypotheses have been advanced. Several possible explanations are addressed here. It has been suggested that the dependence of tensile strength on ϕ_g may be stronger than that of shear strength because of the differences in failure plane positioning. In the shear strength tests, the location of the shear vane determines the cylindrical failure plane. The shear vane position is effectively random; thus, the shear vane measurement determines the shear strength along a randomly placed shear plane. The vertical extrusion tensile strength tests, by contrast, allow the sample to fail at its weakest point. If increasing

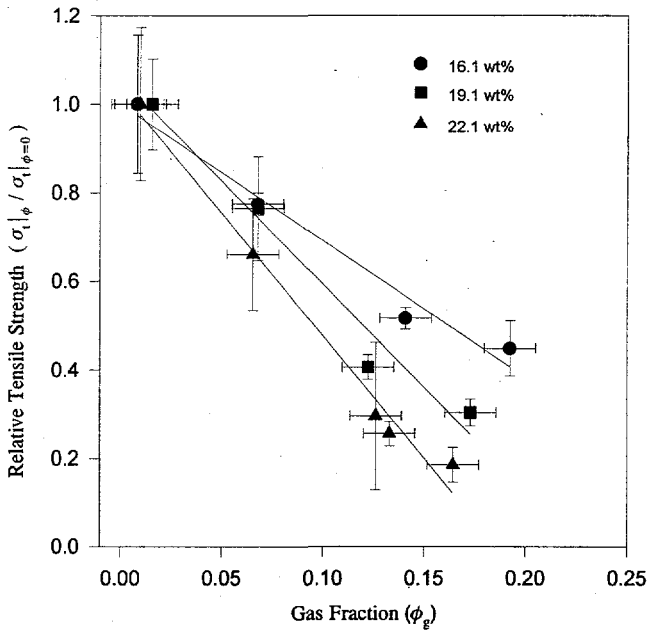

Figure 5.11. Relative Tensile Strength Versus Gas Fraction in Clay

gas fraction results in progressively greater axial variations in the tensile strength of the extruding segments, then it would be expected that increases in gas fraction would result in greater decreases in tensile strength than would be expected from the simple cross-sectional area equation given above.[a]

Consider a 5-cm (2-in.)-long segment of bubbly sludge simulant that is 2.5 cm (1 in.) in diameter. Assuming a gas fraction of 0.20 and 1 mm diameter bubbles, a total of 5000 bubbles are present in the segment. Figure 5.12 shows a two-dimensional representation of 5000 randomly placed bubbles within a segment of sludge. This plot shows that randomly placed bubbles result in regions that are significantly higher in bubble concentration and other regions that are significantly lower. To illustrate this point, Figure 5.13 was prepared. Using the data given in Figure 5.12 (which were randomly generated using a computer program), 1-mm thick-cross sections were applied to the hypothetical 2.5-cm-long segment. The number of bubbles captured by each cross section was tallied and plotted in Figure 5.13. It is seen that the number of bubbles per 1-mm section varies considerably along the length of the segment from a low of 79 to a high of about 124. Based on this, it would be expected that the vertical extrusion tensile

(a) Axial variations in bubble concentration will result in lower tensile strength measurements if the cross-sections containing high bubble concentrations are not separated by more than a couple of centimeters. If the high bubble concentration regions (low strength) are separated by larger distances, the effect of the local concentration variations would be to increase the variation in the measured tensile strengths without significantly affecting the mean tensile strength.

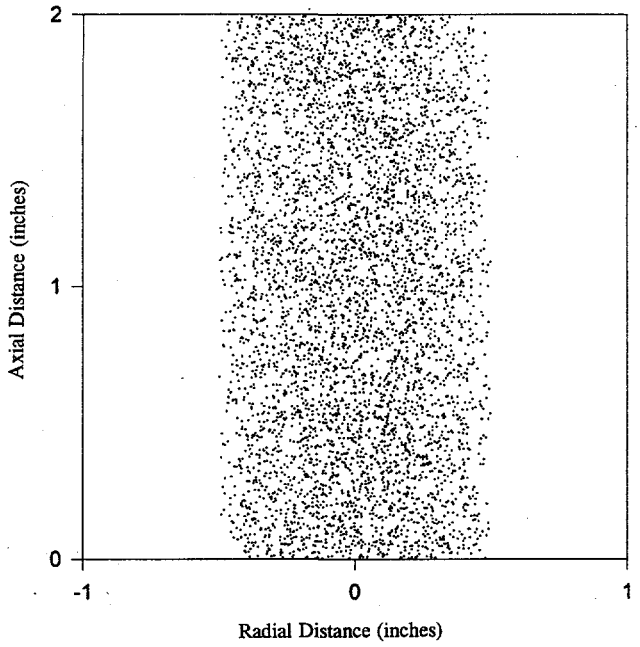

Figure 5.12. Bubble Locations in a 1-in. Diameter, 2-in.-Long Cylindrical Segment Containing 5000 1-mm-Diameter Bubbles (ϕ_g = 0.20)

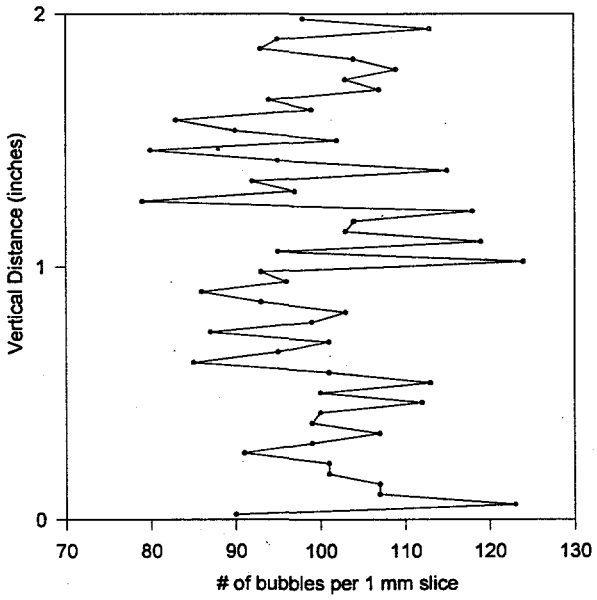

Figure 5.13. Number of Bubbles Present in 1-mm-Thick Sections of Hypothetical Sludge Segment

strength of this hypothetical sample would be approximately 20% to 30% lower than what would be predicted using the simple equation given earlier (with the average gas fraction used for ϕ_g). Thinner cross-sections, of course, result in even larger variations in bubble concentration.

A 20 to 30% reduction is not sufficient to account for the observed dependence of tensile strength on gas fraction; a much larger reduction is required. For example, the 22.1 wt% bentonite data shown in Figure 5.9 show that at $\phi_g = 0.15$ the tensile strength is about 8.8 kdyne/cm^2. If the tensile strength followed a $1-\phi_g$ relationship like shear strength, then a tensile strength of 39.3 kdyn/cm^2 would be predicted for $\phi_g = 0.15$. A 30% reduction in this prediction still leaves the predicted tensile strength too high at 27.5 kdyne/cm^2. It seems unlikely that sample inhomogeneity resulting from random bubble distribution can account for the observed strong dependence of tensile strength on gas fraction.

Another problem with this hypothesis is that bubble distribution within the sample is not truly random. In fact, the bubbles are likely to be more evenly distributed than random placement would suggest. The bubble nucleation sites probably are randomly distributed throughout the sample, but bubble growth is controlled by the local concentration of dissociating hydrogen peroxide. As a bubble grows, the region surrounding the bubble becomes depleted in oxygen (generated by hydrogen peroxide). Thus it is unlikely that two bubbles of average size would form and continue to grow in proximity. Considered another way, it is also unlikely that a sizeable region would be devoid of bubbles, because the oxygen generated in that region would then need to diffuse an improbable distance to reach the nearest bubble. These forces have the effect of creating a more uniform distribution of bubbles throughout the sample than would be expected from a purely random distribution.

Another possible explanation for the tensile strength data is stress concentration. In the region near a bubble surface, the applied forces are magnified by the disruption of the stress field that results from the bubble. The result of the stress concentrations is that the bubbly samples will fail at lower stresses. It is not known whether stress concentrations alone can account for the magnitude of tensile strength reductions observed in this study.

A potential problem with the stress-concentration hypothesis is that the stress concentrations would be expected to affect the shear as well as the tensile strength. The relative importance of the effect may be different for shear and tension, but the fact that the shear strength data can be explained without invoking stress concentration effects is troubling. To help resolve whether stress concentration effects can account for the shear and tensile strength data, we recommend examining the relevant literature.

Results from percolation theory were also used to examine the tensile strength data in an effort to understand the dependence of tensile strength on gas fraction. Percolation theory was developed to model the properties of large, random mixtures of conducting and nonconducting links. An example for mechanical problems would be an array of a large number of randomly interconnected springs. Percolation theory can be used to model changes in the physical properties of the array as springs are randomly removed. If a bubbly sludge simulant is considered to be made up of randomly interconnected regions of sludge surrounding void regions (gas bubbles), then percolation theory can be applied to model the sludge mechanical properties (Arbabi and Sahimi 1990; Stauffer 1985)[(a)]

(a) Applying percolation concepts to mechanical behavior of bubbly sludges was discussed in a letter report by P. A. Gauglitz entitled, *An Approach to Modeling Bubble Retention and Release from Tank Waste*, July 1993, Pacific Northwest Laboratory, Richland, Washington.

The dependence of Young's modulus on gas fraction can be predicted for an elastic material using percolation theory. If the assumption is made that tensile failure occurs in a bubbly sludge at a given strain (regardless of ϕ_g), then the tensile strength is directly proportional to Young's modulus. Making this assumption, percolation theory predicts that the tensile strength should depend on gas fraction according to an equation of the form

$$\sigma_t = \sigma_{t,0} \frac{(1-\phi_g-\phi_c)^z}{(1-\phi_c)^z} \tag{5.4}$$

where $\sigma_{t,0}$ is the tensile strength at $\phi_g = 0$, ϕ_c is the solids fraction at which the tensile strength goes to zero, and z is a constant. There are theoretical and experimental justifications in the literature for selecting a z of 3.3, and ϕ_c is usually about 0.1 to 0.2 (Benguigui 1984; Deptuck et al. 1985).

The tensile strength data for 22.1 wt% bentonite versus ϕ_g are compared to the percolation model predictions in Figure 5.14. The data are well fit by the percolation model when $z = 3.3$ and $\phi_c = 0.6$ are used. Comparably good fits of the tensile strength data for the 16.1 wt% and 19.1 wt% simulants are obtained using slightly different values for ϕ_c and the same value for z.

It is possible that the dependence of the σ_t versus ϕ_g curves on wt% bentonite can be explained in terms of percolation theory and the assumption that the strain required to induce failure decreases with increasing wt% bentonite. The relationship between failure strain and wt% bentonite was not investigated during the shear and tensile strength testing. Alderman et al. (1991) measured the rheological properties of bentonite gels and reported that the gel yield strain decreases sharply as the wt% of bentonite is increased. Changes in yield strain are expected to be indicative of changes in failure strain. It seems plausible that this decrease in failure strain with increasing wt% bentonite is at least partially responsible for the dependence of relative tensile strength on wt% bentonite shown in Figure 5.11.

The percolation theory model may be a powerful tool for understanding the effects of gas fraction on sludge strength, but this is uncertain. The tensile strength data collected in this study are consistent with percolation theory in some respects, but not in all. For example, it is unclear how to reconcile the percolation model predictions with the observation that the bubbly sludge shear strength decreases in proportion to $1-\phi_g$. Changes in Young's modulus with increasing ϕ_g would be expected to result in nearly proportional changes in the shear modulus.[a] A further problem with the percolation theory predictions is that an unusually-high value for ϕ_c must be selected to obtain a reasonable fit of the experimental data. As described earlier, a ϕ_c of 0.6 was used to fit the data in Figure 5.13 even though ϕ_c values are typically 0.10 to 0.20. Selection of ϕ_c=0.6 cannot currently be defended.

(a) Shear modulus is equal to Young's modulus divided by $2(1+\mu)$ where μ is Poisson's ratio. Typical values for μ range from 0.25 to 0.50.

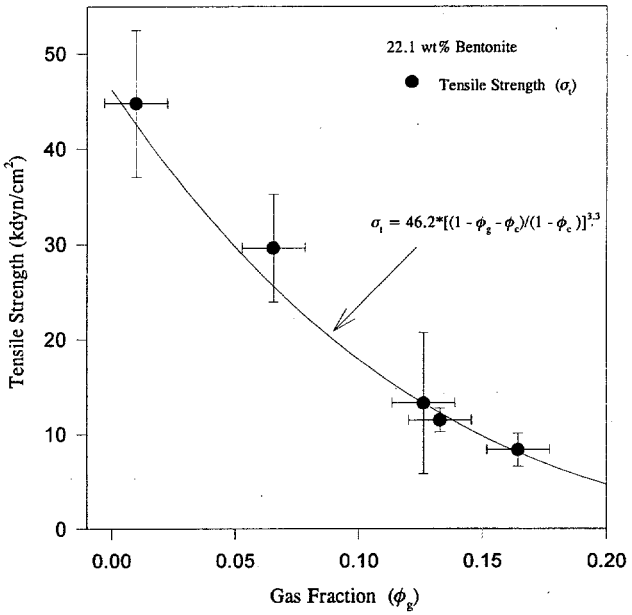

Figure 5.14. Tensile Strength Data Fit by Percolation Theory Equation

Regardless of why the tensile strength decreases rapidly with ϕ_g, the test data imply that bubble-laden cohesive sludge may be more vulnerable to failure in tension than in shear. The modes of failure involved in flammable gas release events are not presently understood well enough to determine whether shear or tensile forces dominate. The shear strength and tensile strength data gathered during this study will assist future gas release modeling efforts. The models include assumptions for the dependence of sludge physical properties on gas fraction, and the data from this study will help to validate and improve these assumptions.

6.0 Conclusions

Several of the underground nuclear waste storage tanks at Hanford have been placed on the Flammable Gas Watch List because the waste is either known or suspected to generate, store, and episodically release flammable gases. Bubble retention, the effect of retained bubbles on the waste physical properties, and the release of bubbles from the waste are critical aspects of the episodic releases of flammable gases from Hanford waste tanks. This research added to our understanding of bubble retention mechanisms and the effect bubbles have on the viscosity and tensile and shear strengths of simulated wastes. Following are the specific conclusions of this work:

- A new approach has been developed and evaluated for creating bubbles in sludge; it involves dissolving a soluble gas into the supernatant liquid at an elevated pressure, mixing the liquid containing dissolved gas through the sludge, then reducing the pressure to allow bubbles to nucleate and grow. The technique has been successful for studies with CO_2 as the soluble gas in slurries of water and glass beads. Experimental results show that an equilibrium CO_2 pressure of 2.4×10^5 Pa (20 psig) was sufficient to create good bubble nucleation and growth, and a pressure reduction rate of 6900 Pa/min (1 psi/min) provided for a controllable experiment. A modification of this approach, in which a vacuum is applied to the sample to enhance bubble nucleation and growth following a dosage of radiation sufficient to create a small volume of gas, should provide a suitable method of measuring bubble retention in real waste samples.

- Results for the transition between dendritic and round bubbles show that the transition moved deeper into a slurry with decreasing particle size and decreasing density difference between the supernatant liquid and particles. The observed location of the transition agrees reasonably well with the Bond number scaling when the Bond number is modified to account for the sludge strength. Bubble retention occurs in three regimes: dendritic bubbles were seen in a lower region of the settled slurry; round bubbles displaced particles in the upper region; and, in most cases, very large bubbles appear to fracture simulated sludges at the transition between dendritic and round bubbles.

- The viscosities of bubbly slurries were measured with a capillary rheometer for bubbly slurries composed of PMMA particles in glycerol/water/nitrogen mixtures. Viscosity results were obtained for shear rates generally ranging between 1 and 30 s^{-1}, gas fractions ranging from 0 to 20 vol% bubbles, and particle fractions ranging from 43 to 50 vol%. The viscosity of the bubbly slurries increased with increasing gas fraction and increased with increasing particle fraction, as expected. A model for correlating the viscosity of bubbly slurries that fits the experimental data fairly well was developed to account for the effect of shear rate and gas and particle volume fractions on the slurry viscosity. Important attributes of the viscosity data are that the gas content had a more pronounced effect than expected and that the bubbly slurries become more shear thinning with increasing gas-bubble fraction.

- Tensile and shear strength of bubbly sludge and slurry simulants were measured to quantify the effect of gas bubbles on and to improve the understanding of the relationships between shear and tensile strengths for gas-containing sludges and slurries. Tensile strength measurements were made using a vertical extrusion tensiometer, and shear strength measurements were made using a shear vane for slurries composed of glass particles and water and sludges composed of clays dispersed in water. The vertical extrusion tensiometer was chosen because it can be adapted to hot cell experiments on actual samples. For the sludge simulants (clay-based), results show that the shear strength decreased proportional to the gas content. For the tensile strength, however, the gas fraction had a more dramatic role, and the tensile strength decreased proportional to the third power of the gas content. For slurry simulants, in contrast, the shear and tensile strengths were larger in the presence of gas bubbles. This dramatic difference between slurry and sludge simulants highlights the need to perform measurements on real waste samples.

- Viscosity measurements have not been taken on bubbly slurries with very small particles (compared with the bubbles). For bubbly clay-based sludges such as this, the tensile and shear strength measurements show that the bubbles decreased the strength of the material. It is expected that the viscosity of this type of sludge will also decrease with increasing gas fraction, in contrast to the measurements on bubbly slurries with bubbles and particles of similar size.

- A model was developed to determine how bubbles of different morphology are distributed within a waste tank, based on the Bond number scaling (Appendix E). Gas was allowed to migrate within the tank when the gas fraction was sufficiently large to allow gas bubbles to connect. With this model, calculations show how the different regimes of bubble retention evolve following a series of rollover events and how a series of rollovers is affected by bubble distributions and morphology.

7.0 References

Arabi, S., and M. Sahimi. 1990. "Test of Universality for Three-Dimensional Models of Mechanical Breakdown in Disordered Solids." *Physical Rev. B*, 41(1):772-775.

Ajaz, A., and R. H. G. Parry. 1974. "An Unconfined Direct Tension Test for Compacted Clays." *Journal of Testing and Evaluation*, 2(3):163-172.

Al-Hussaini, M. M., and F. C. Townsend. 1973. *Tensile Testing of Soils: A Literature Review*. Miscellaneous Paper S-73-24. U. S. Army Engineer Waterways Experiment Station. Vicksburg, Mississippi.

Alderman, N. J., G. H. Meeten, and J. D. Sherwood. 1991. "Vane Rheometry of Bentonite Gels." *Journal of Non-Newtonian Fluid Mechanics*, Vol. 39, pp. 291-310.

Allemann, R. T., Z. I. Antoniak, W. D. Chvala, L. E. Efferding, J. G. Fadeff, J. R. Friley, W. B. Gregory, J. D. Hudson, J. J. Irwin, N. W. Kirch, T. E. Michener, F. E. Panisko, C. W. Stewart, and B. M Wise. 1994. *Mitigation of Tank 241-SY-101 by Pump Mixing: Results of Testing Phases A and B*. PNL-9423, Pacific Northwest Laboratory, Richland, Washington.

Allemann, R. T., Z. I. Antoniak, J. R. Friley, C. E. Haines, L. M. Liljegren, and S. Somasundaram. 1990a. *Mechanistic Analysis of Double-Shell Tank Gas Release--Progress Report, November*. PNL-7657, Pacific Northwest Laboratory, Richland, Washington.

Allemann, R. T., Z. I. Antoniak, J. R. Friley, C. E. Haines, L. M. Liljegren, and S. Somasundaram. 1990b. *Collection and Analysis of Existing Data for Waste Tank Mechanistic Analysis--Progress Report, December*. PNL-7658, Pacific Northwest Laboratory, Richland, Washington.

Allemann, R. T., Z. I. Antoniak, L. L. Eyler, and L. M. Liljegren. 1991. *Conceptual Models for Waste Tank Mechanistic Analysis--Status Report, January*. PNL-8011, Pacific Northwest Laboratory, Richland, Washington.

Allemann, R. T., T. M. Burke, D. A. Reynolds, and D. E. Simpson. 1993. *Assessment of Gas Accumulation and Retention--Tank 241-SY-101*. WHC-EP-0576, Westinghouse Hanford Company, Richland, Washington.

Barnes, H. A., J. F. Hutton, and K. Walters. 1989. *An Introduction to Rheology*. Elsevier, New York.

Benguigui, L. 1984. "Experimental Study of the Elastic Properties of a Percolating System." *Phy. Rev. Lett.*, 53(21):2028-30.

Bishop, A. W., and V. K. Garga. 1969. "Drained Tension Tests on London Clay." *Geotechnique*, Vol. 19, pp. 309-313.

Bryan, S. A., and L. R. Pederson. 1994. *Composition, Preparation, and Gas Generation Results from Simulated Wastes of Tank 241-SY-101*. PNL-10075, Pacific Northwest Laboratory, Richland, Washington.

Bryan, S. A., L. R. Pederson, J. L. Ryan, R. D. Scheele, and J. M. Tingey. 1992. *Slurry Growth, Gas Retention, and Flammable Gas Generation by Hanford Radioactive Waste Tanks: Synthetic Waste Studies, FY 1991*. PNL-8169, Pacific Northwest Laboratory, Richland, Washington.

Das, B. M. 1983. *Advanced Soil Mechanics*. Hemisphere Publishing Corporation, New York.

Deptuck, D., J. P. Harrison, and P. Zawadski. 1985. "Measurement of Elasticity and Conductivity of a Three-Dimensional Percolating System." *Phy. Rev. Lett.*, 54(9):913-16.

Gauglitz, P. A., L. A. Mahoney, D. P. Mendoza, and M. C. Miller. 1994a. *Mechanisms of Gas Bubble Retention*. PNL-10120, Pacific Northwest Laboratory, Richland, Washington.

Gauglitz, P. A., R. R. Shah, and R. L. Davis. 1994b. *Gas Distribution Effects on Waste Properties: Viscosity of Bubbly Slurries*. PNL-10112, Pacific Northwest Laboratory, Richland, Washington.

Hall, M. N. 1993. *Tank 101-SY Hydrogen Mitigation by Low Frequency Vibration–Rheological Analysis and Feasibility Assessment*. WHC-SD-WM-ER-164, Westinghouse Hanford Company, Richland, Washington.

Hasegawa, H., and M. Ikeuti. 1966. "On the Tensile Strength Test of Disturbed Soils." *Rheology and Soil Mechanics Symposium: International Union of Theoretical and Applied Mechanics,* pp. 405-412.

Herting, D. L. 1991. *Laboratory Characterization of Samples Taken in May 1991 from Hanford Waste Tank 241-SY-101*. WHC-SD-WM-DTR-024 Rev. 0, pp. 3-5. Westinghouse Hanford Company, Richland, Washington.

Jamaluddin, A. K. M., C. T. Bowen, R. Gillies, M. Small, and T. W. Nazarko. 1994. "Characteristics of Heavy-Oil-in Water Emulsions Containing Produced Sand." *The Canadian Journal of Chemical Engineering*, Vol. 72, pp. 380-383.

Kundu, N., and G. P. Peterson. 1987. "Transmission of Solid Particulates Using a Two-Phase Medium." *Journal of Energy Resources Technology*, Vol. 109, pp. 35-39.

Lambe, T. W., and R. V. Whitman. 1969. *Soil Mechanics*. John Wiley and Sons, New York.

Lee, C. C., and H. Y. Sohn. 1985. "Experimental Investigation and Mathematical Modeling of the Ignition of an Oil Shale Bed with Hot Air." *Ind. Eng. Chem. Process Des. Dev.*, Vol. 24, pp. 753-761.

Li, X., and Y. C. Yortsos. 1995. "Theory of Multiple Bubble Growth in Porous Media by Solute Diffusion." *Chemical Engineering Science*, 50 (8):1247-1271.

Macosko, C. W. 1994. *Rheology: Principles, Measurements, and Applications*. VCH Publishers, New York.

Mooney, M. 1931. *J. Rheology*, Vol. 2, p. 210.

Nguyen, Q. D., and D. V. Boger. 1992. "Measuring the Flow Properties of Yield Stress Fluids." *Annu. Rev. Fluid Mech.*, 24:47-88.

Norton, J. D., and L. R. Pederson. 1994. *Ammonia in Simulated Hanford Double-Shell Tank Wastes: Solubility and Effects on Surface Tension.* PNL-10173, Pacific Northwest Laboratory, Richland, Washington.

Okpobiri, G. A., and C. U. Ikoku. 1983. "Experimental Determination of Friction Factors for Mist and Foam Drilling and Well Cleanout Operations." *Transactions of the ASME*, Vol. 105, pp. 542-553.

Perry, J. H. 1950. *Chemical Engineer's Handbook.* McGraw-Hill, New York.

Powell, M. R., G. R. Golcar, C. R. Hymas, and R. L. McKay. 1995a. *Fiscal Year 1993 1/25-Scale Sludge Mobilization Testing.* PNL-10464, Pacific Northwest Laboratory. Richland, Washington.

Powell, M. R. C. M. Gates, C. R. Hymas, M. A. Sprecher, and N. J. Morter. 1995b. *Fiscal Year 1994 1/25-Scale Sludge Mobilization Testing.* PNL-10582, Pacific Northwest Laboratory, Richland, Washington.

Rassat, S. D., and P. A. Gauglitz. 1995. *Bubble Retention in Synthetic Sludge: Testing of Alternative Gas Retention Apparatus.* PNL-10661, Pacific Northwest Laboratory, Richland, Washington.

Reynolds, D. A. 1992. *Tank 101-SY Window C Core Sample Results and Interpretation.* WHC-EP-0589, Westinghouse Hanford Company, Richland, Washington.

Satik, C., and Y. C. Yortsos. 1991. "Percolation Models for Boiling and Bubble Growth in Porous Media at Low Superheats." Presented at the Third Symposium on Multiphase Transport in Porous Media, Atlanta, Georgia, ASME Winter Annual Meeting, December 1-6, 1991.

Schumb, W. C., C. N. Satterfield, and R. L. Wentworth. 1955. *Hydrogen Peroxide.* Reinhold Publishing Corporation. New York.

Stauffer, D. 1985. *Introduction to Percolation Theory.* Taylor and Francis, London.

Tennant, R. A., E. C. Sams, and J. P. Piccola, Jr. 1993. *Simulation and Rheological Analysis of Hanford Tank 241-SY-101.* LA-UR-93-3800, Los Alamos National Laboratory, Los Alamos, New Mexico.

Thondavadi, N. N. 1983. *Flow Properties of Foam with and Without Solid Particles*. Ph.D. Thesis, University of Cincinnati, Cincinnati, Ohio.

Thondavadi, N. N., and R. Lemlich. 1985. "Flow Properties of Foam With and Without Solid Particles." *Ind. Eng. Chem. Process Des. Dev.*, Vol. 24, pp. 748-753.

Thorne, C. R., N. K. Tovey, and R. Bryant. 1980. "Recording Unconfined Tension Tester." *Journal of the Geotechnical Engineering Division ASCE.*, 106(GT11):1269-1273.

Tingey, J. M., P. R. Bredt, and E. H. Shade. 1994. *The Effects of Heating and Dilution on the Rheological and Physical Properties of Tank 241-SY-101*. PNL-10198, Pacific Northwest Laboratory, Richland, Washington.

Tschebotarioff, G. P., E. R. Ward, and A. A. DePhillippe. 1953. "The Tensile Strength of Disturbed and Recompacted Soils." *Proc. 3rd International Conference on Soil Mechanics and Foundation Engineering*, Vol. 1, pp. 207-210.

Yaws, C., H-C. Yang, and X. Pan. November 1991. "Henry's Law Constants for 362 Organic Compounds in Water." *Chemical Engineering*, pp. 179-185.

Yortsos, Y. C., and M. Parlar. 1989. "Phase Change in Binary systems in Porous Media: Application to Solution-Gas Drive." SPE 19697, presented at the 64th Annual Meeting of the Society of Petroleum Engineers, San Antonio, Texas, October 8-11, 1989.

Appendix A

Bubble Retention Data

Table A.1. Levels of Settled Sludge and Supernatant Liquid as a Function of Elapsed Time from Start of Depressurization for 90-Micron Glass Beads in Water (initial [equilibrium] CO_2 pressure 1.7 x 10^5 Pa [10 psig]; pressure reduction rate was 6900 Pa/min [1 psi/min])

Elapsed Time, min.	Sludge Height, cm	Sludge Height, cm	Liquid Height, cm	Liquid Height, cm	Gauge Pressure, psig
0	14.16	0	16.47	0	10.2
9	14.17	0.01	16.48	0.01	0
10	14.35	0.19	16.8	0.33	0
10.5	14.48	0.32	16.9	0.43	0
11.5	14.6	0.44	17	0.53	0
13	14.72	0.56	17.1	0.63	0
15	14.84	0.68	17.19	0.72	0
17	14.93	0.77	17.27	0.8	0
19	15.01	0.85	17.32	0.85	0
26	15.17	1.01	17.47	1	0
32	15.25	1.09	17.56	1.09	0
39	15.38	1.22	17.67	1.2	0
48	15.48	1.32	17.76	1.29	0
57	15.53	1.37	17.82	1.35	0
67	15.61	1.45	17.91	1.44	0
90	15.68	1.52	17.97	1.5	0

Table A.2. Levels of Settled Sludge and Supernatant Liquid as a Function of Elapsed Time from Start of Depressurization for 90-Micron Glass Beads in Water (initial [equilibrium] CO_2 pressure 2.5 x 10^5 Pa [22 psig]; pressure reduction rate 6900 Pa/min [1 psi/min])

Elapsed Time, min.	Sludge Height, cm	Sludge Height, cm	Liquid Height, cm	Liquid Height, cm	Gauge Pressure, psig
0	14	0	16.78	0	22
18	14.05	0.05	16.85	0.07	4
19	14.1	0.1	16.85	0.07	2
20	14.15	0.15	16.9	0.12	2
21	14.6	0.6	17.3	0.52	0
21.5	14.8	0.8	17.5	0.72	0
22	14.9	0.9	17.6	0.82	0
23.5	15.15	1.15	17.85	1.07	0
24.5	15.3	1.3	18	1.22	0
26	15.45	1.45	18.2	1.42	0
28	15.7	1.7	18.4	1.62	0
29	15.85	1.85	18.55	1.77	0
30.5	16.05	2.05	18.75	1.97	0
32	16.25	2.25	18.95	2.17	0
34	16.4	2.4	19.1	2.32	0
36	16.6	2.6	19.3	2.52	0
38	16.75	2.75	19.45	2.67	0
40	16.8	2.8	19.5	2.72	0
43	17	3	19.65	2.87	0
46	17	3	19.7	2.92	0
49	17.1	3.1	19.8	3.02	0
53	17.3	3.3	19.95	3.17	0
59	17.5	3.5	20.15	3.37	0
62	16.9	2.9	19.5	2.72	0
68	16.95	2.95	19.55	2.77	0
98	17.1	3.1	19.7	2.92	0

Table A.3. Levels of Settled Sludge and Supernatant Liquid as a Function of Elapsed Time from Start of Depressurization for 90-Micron Glass Beads in Water (initial [equilibrium] CO_2 pressure 3.4 x 10^5 Pa [34 psig]; pressure reduction rate 6900 Pa/min [1 psi/min])

Elapsed Time, min.	Sludge Height, cm	Sludge Height, cm	Liquid Height, cm	Liquid Height, cm	Gauge Pressure, psig
0	14.92	0	17.75	0	34
16	14.92	0	17.78	0.03	18
18	14.98	0.06	17.9	0.15	16
20	15.08	0.16	18	0.25	14
22	15.2	0.28	18.12	0.37	12
24	15.4	0.48	18.3	0.55	10
26	15.55	0.63	18.5	0.75	8
27	15.8	0.88	18.7	0.95	6
28	15.9	0.98	18.8	1.05	6
29	16.05	1.13	19.05	1.3	4
30	16.2	1.28	19.15	1.4	4
31	16.65	1.73	19.52	1.77	2
32	16.8	1.88	19.65	1.9	2
33	17.4	2.48	20.35	2.6	0
33.5	17.7	2.78	20.6	2.85	0
34	16.5	1.58	19.45	1.7	0
35	17	2.08	19.9	2.15	0
36	16.6	1.68	19.45	1.7	0
37.5	17	2.08	19.9	2.15	0
39	17.15	2.23	20.1	2.35	0
44	18	3.08	20.9	3.15	0
53	17.2	2.28	20	2.25	0
57.5	17.35	2.43	20.2	2.45	0
59	17.38	2.46	20.22	2.47	0
60.5	16.8	1.88	19.5	1.75	0
76	16.65	1.73	19.4	1.65	0

Table A.4. Levels of Settled Sludge and Supernatant Liquid as a Function of Elapsed Time from Start of Depressurization for 90-Micron Glass Beads in Water (initial [equilibrium] CO_2 pressure 2.4 x 10^5 Pa [20.5 psig]; pressure reduction rate 1400 Pa/min [0.2 psi/min])

Elapsed Time, min.	Sludge Height, cm	Sludge Height, cm	Liquid Height, cm	Liquid Height, cm	Gauge Pressure, psig
0	14.8	0	17.4	0	20.5
75	14.82	0.02	17.45	0.05	5
80	14.87	0.07	17.5	0.1	4
82	14.92	0.12	17.56	0.16	3
85	14.93	0.13	17.57	0.17	3
87.5	15.02	0.22	17.66	0.26	2
90	15.04	0.24	17.68	0.28	2
91	15.15	0.35	17.77	0.37	1
93	15.28	0.48	17.88	0.48	1
95	15.37	0.57	17.97	0.57	1
96	15.66	0.86	18.28	0.88	0
97	15.8	1	18.4	1	0
98.5	16.08	1.28	18.58	1.18	0
100	16.2	1.4	18.7	1.3	0
102	16.3	1.5	18.82	1.42	0
105	16.48	1.68	19	1.6	0
108	16.6	1.8	19.11	1.71	0
112	16.78	1.98	19.33	1.93	0
118	17.09	2.29	19.58	2.18	0
126	16.13	1.33	18.65	1.25	0
139	16.34	1.54	18.8	1.4	0
151	16.55	1.75	19	1.6	0
165	16.73	1.93	19.19	1.79	0
191	17	2.2	19.47	2.07	0
209	16.51	1.71	19.02	1.62	0

Table A.5. Levels of Settled Sludge and Supernatant Liquid as a Function of Elapsed Time from Start of Depressurization for 90-Micron Glass Beads in Water (initial [equilibrium] CO_2 pressure 2.5 x 10^5 Pa [22 psig]; pressure reduction rate > 6.9 x 10^4 Pa [> 10 psi/min])

Elapsed Time, min.	Sludge Height, cm	Sludge Height, cm	Liquid Height, cm	Liquid Height, cm	Gauge Pressure, psig
0	14.3	0	16.95	0	22
1	14.38	0.08	17.12	0.17	10
2	16.3	2	19.08	2.13	0
2.5	16.75	2.45	19.55	2.6	0
3	17.15	2.85	19.9	2.95	0
3.5	17.45	3.15	20.1	3.15	0
4.5	17.85	3.55	20.5	3.55	0
6	18.1	3.8	20.85	3.9	0
7	18.25	3.95	21	4.05	0
8.5	16.55	2.25	19.2	2.25	0
10	16.3	2	18.9	1.95	0
13.5	16.5	2.2	19.15	2.2	0
16	16.65	2.35	19.25	2.3	0
20	16.7	2.4	19.3	2.35	0

Table A.6. Levels of Settled Sludge and Supernatant Liquid as a Function of Elapsed Time from Start of Depressurization for 0.2-mm Glass Beads in Water (initial [equilibrium] CO_2 pressure 3.2 x 10^5 Pa [31 psig]; pressure reduction rate 6900 Pa/min [1 psi/min])

Elapsed Time, min.	Sludge Height, cm	Sludge Height, cm	Liquid Height, cm	Liquid Height, cm	Gauge Pressure, psig
	15.05	0	17.5	0	27
22	15.05	0	17.51	0.01	9
24	15.08	0.03	17.57	0.07	7
26	15.25	0.2	17.68	0.18	5
27	15.4	0.35	17.8	0.3	3
28	15.5	0.45	17.9	0.4	3
29	15.82	0.77	18.18	0.68	1
30	15.55	0.5	18	0.5	1
31	15.9	0.85	18.37	0.87	0
32	16.25	1.2	18.68	1.18	0
33	16.5	1.45	18.95	1.45	0
33.5	16.65	1.6	19.1	1.6	0
34	16.8	1.75	19.2	1.7	0
35	16.9	1.85	19.35	1.85	0
36	17	1.95	19.5	2	0
37	17.15	2.1	19.65	2.15	0
38	16.15	1.1	18.5	1	0
41	16.35	1.3	18.8	1.3	0
43	16.5	1.45	18.95	1.45	0
45	16.65	1.6	19.08	1.58	0
48	16.8	1.75	19.24	1.74	0
50	16.8	1.75	19.2	1.7	0
51.5	16.9	1.85	19.28	1.78	0
53	16.95	1.9	19.35	1.85	0
55	17.02	1.97	19.42	1.92	0
57	17.05	2	19.44	1.94	0
59	17.1	2.05	19.48	1.98	0
61	17.15	2.1	19.52	2.02	0
63	17.18	2.13	19.55	2.05	0
66	17.25	2.2	19.62	2.12	0
69	17.28	2.23	19.64	2.14	0
71	17.3	2.25	19.67	2.17	0
74	17.32	2.27	19.7	2.2	0
82	17.38	2.33	19.73	2.23	0
85	17.4	2.35	19.76	2.26	0

Table A.7. Levels of Settled Sludge and Supernatant Liquid as a Function of Elapsed Time from Start of Depressurization for 0.5-mm Glass Beads in Water (initial [equilibrium] CO_2 pressure 3.3 x 10^5 Pa [33 psig]; pressure reduction rate 6900 Pa/min [1 psi/min])

Elapsed Time, min.	Sludge Height, cm	Sludge Height, cm	Liquid Height, cm	Liquid Height, cm	Gauge Pressure, psig
0	15.2	0	17.2	0	33
24	15.22	0.02	17.22	0.02	9
26	15.22	0.02	17.23	0.03	7
26	15.23	0.03	17.25	0.05	5
30	15.23	0.03	17.27	0.07	3
31	15.23	0.03	17.35	0.15	1
32	15.24	0.04	17.48	0.28	1
33	15.35	0.15	17.5	0.3	0
34	15.35	0.15	17.51	0.31	0
35	15.35	0.15	17.58	0.38	0
36.5	15.35	0.15	17.52	0.32	0
38	15.35	0.15	17.55	0.35	0
40.5	15.4	0.2	17.66	0.46	0
44	15.4	0.2	17.62	0.42	0

Table A.8. Levels of Settled Sludge and Supernatant Liquid as a Function of Elapsed Time from Start of Depressurization for 1.0-mm Glass Beads in Water (initial [equilibrium] CO_2 pressure 3.1 x 10^5 Pa (30 psig); pressure reduction rate 6900 Pa/min [1 psi/min])

Elapsed Time, min.	Sludge Height, cm	Sludge Height, cm	Liquid Height, cm	Liquid Height, cm	Gauge Pressure, psig
0	15.5	0	17.5	0	30
22	15.5	0	17.52	0.02	8
24	15.5	0	17.53	0.03	6
26	15.5	0	17.55	0.05	4
28	15.5	0	17.6	0.1	2
29.5	15.5	0	17.75	0.25	0
30	15.5	0	17.9	0.4	0
30.5	15.5	0	18	0.5	0
31.5	15.6	0.1	18.12	0.62	0
32	15.6	0.1	18.2	0.7	0
33	15.6	0.1	18.4	0.9	0
34	15.6	0.1	18.5	1	0
36	15.6	0.1	18.6	1.1	0
38	15.6	0.1	18.62	1.12	0
40.5	15.6	0.1	18.7	1.2	0
43	15.6	0.1	18.7	1.2	0
46	15.65	0.15	18.75	1.25	0
51.5	15.65	0.15	18.8	1.3	0
58	15.65	0.15	18.8	1.3	0
67	15.65	0.15	18.77	1.27	0
71	15.65	0.15	18.7	1.2	0

Table A.9. Levels of Settled Sludge and Supernatant Liquid as a Function of Elapsed Time from Start of Depressurization for Mixture of 75 wt% 1.0-mm and 25 wt% 90-Micron Glass Beads in Water (initial [equilibrium] CO_2 pressure was 3.2×10^5 Pa [31 psig]; pressure reduction rate was 6900 Pa/min [1 psi/min])

Elapsed Time, min.	Sludge Height, cm	Sludge Height, cm	Liquid Height, cm	Liquid Height, cm	Gauge Pressure, psig
0	11.78	0	16.22	0	31
4	11.73	-0.05	16.22	0	27
6	11.72	-0.06	16.22	0	25
8	11.7	-0.08	16.22	0	23
18	11.7	-0.08	16.27	0.05	13
20	11.7	-0.08	16.3	0.08	11
22	11.75	-0.03	16.4	0.18	9
24	11.78	0	16.55	0.33	7
26	11.85	0.07	16.93	0.71	5
28	11.9	0.12	17.05	0.83	3
29	12.05	0.27	17.15	0.93	1
30	12.08	0.3	17.2	0.98	1
31	12	0.22	17.18	0.96	0
32	12.15	0.37	17.35	1.13	0
33	12.3	0.52	17.45	1.23	0
34	12.4	0.62	17.5	1.28	0
35	12.43	0.65	17.53	1.31	0
36	12.45	0.67	17.55	1.33	0
38.5	12.15	0.37	17.25	1.03	0
42	12.12	0.34	17.3	1.08	0
51	12.2	0.42	17.35	1.13	0
75	12.35	0.57	17.33	1.11	0

Table A.10. Levels of Settled Sludge and Supernatant Liquid as a Function of Elapsed Time from Start of Depressurization for 58-Micron Glass Beads in Water (initial [equilibrium] CO_2 pressure 2.4 x 10^5 Pa [20 psig]; pressure reduction rate 6900 Pa/min [1 psi/min])

Elapsed Time, min.	Sludge Height, cm	Sludge Height, cm	Liquid Height, cm	Liquid Height, cm	Gauge Pressure, psig
0	15.6	0	16.94	0	20
12	15.6	0	16.97	0.03	8
14	15.6	0	17	0.06	6
16	15.62	0.02	17.12	0.18	4
17	15.76	0.16	17.23	0.29	2
18	15.88	0.28	17.45	0.51	2
19	16.17	0.57	17.7	0.76	0
20	16.39	0.79	18.03	1.09	0
21	16.61	1.01	18.24	1.3	0
23	16.97	1.37	18.6	1.66	0
25	17.3	1.7	18.95	2.01	0
27	17.5	1.9	19.2	2.26	0
29.5	17.85	2.25	19.45	2.51	0
33	18.1	2.5	19.7	2.76	0
36	18.35	2.75	19.95	3.01	0
40	18.6	3	20.2	3.26	0
43	16.95	1.35	18.45	1.51	0

Table A.11. Levels of Settled Sludge and Supernatant Liquid as a Function of Elapsed Time from Start of Depressurization for 30-Micron Glass Beads in Water (initial [equilibrium] CO_2 pressure 2.4 x 10^5 Pa [20 psig]; pressure reduction rate 6900 Pa/min [1 psi/min])

Elapsed Time, min.	Sludge Height, cm	Sludge Height, cm	Liquid Height, cm	Liquid Height, cm	Gauge Pressure, psig
0	13.47	0	14.96	0	19.5
6	13.47	0	14.97	0.01	14
8	13.47	0	15	0.04	10
12	13.48	0.01	15.08	0.12	8
14	13.48	0.01	15.18	0.22	6
15	13.58	0.11	15.38	0.42	4
16	13.68	0.21	15.5	0.54	4
17	13.88	0.41	15.83	0.87	2
18	14	0.53	16	1.04	2
19	14.4	0.93	16.5	1.54	0
20	14.65	1.18	16.7	1.74	0
22	14.95	1.48	17.05	2.09	0
24	15.25	1.78	17.3	2.34	0
26	15.46	1.99	17.57	2.61	0
28	15.66	2.19	17.72	2.76	0
32	15.82	2.35	17.9	2.94	0
39	16.2	2.73	18.27	3.31	0
47	16.36	2.89	18.49	3.53	0
56	16.5	3.03	18.67	3.71	0
62	16.55	3.08	18.69	3.73	0

Table A.12. Levels of Settled Sludge and Supernatant Liquid as a Function of Elapsed Time from Start of Depressurization for 71-Micron Polymethylmethacrylate (PMMA) Beads in Water (initial [equilibrium] CO_2 pressure 2.4 x 10^5 Pa [20 psig]; pressure reduction rate 6900 Pa/min [1 psi/min])

Elapsed Time, min.	Sludge Height, cm	Sludge Height, cm	Liquid Height, cm	Liquid Height, cm	Gauge Pressure, psig
0	14.8	0	16.72	0	20.3
6	14.8	0	16.75	0.03	14
10	14.8	0	16.8	0.08	10
12	14.85	0.05	16.87	0.15	8
14	14.85	0.05	16.95	0.23	6
16	15.05	0.25	17.15	0.43	4
17	15.2	0.4	17.4	0.68	2
18	15.4	0.6	17.55	0.83	0
19	15.85	1.05	18	1.28	0
20	16.15	1.35	18.25	1.53	0
22	16.75	1.95	18.9	2.18	0
24	17.3	2.5	19.45	2.73	0
26	17.7	2.9	19.8	3.08	0
28.5	18.3	3.5	20.35	3.63	0
30	18.8	4	20.75	4.03	0
32	19.6	4.8	21.6	4.88	0
36	17.15	2.35	19.4	2.68	0
38	17.35	2.55	19.7	2.98	0
40	18.3	3.5	20.4	3.68	0
43	18.8	4	20.85	4.13	0
45.5	19.3	4.5	21.25	4.53	0
48	18.7	3.9	20.45	3.73	0

Appendix B

Capillary Rheometry Data Analysis

Appendix B

Capillary Rheometry Data Analysis

To determine viscosity from flow rate and pressure drop data, the results given by Equations 4.1–4.3 are used (see also discussions by Nguyen and Boger [1992]; Macosko [1994]; and Barnes et al. [1989]). To determine the derivative of the flow (Q) versus pressure drop (as τ_w) data for use in Equation 4.1, we used a numerical algorithm rather than plotting the data. A three point for central difference relation for unequally spaced data was derived to calculate the slopes at each point within the highest and lowest flow rates. A three point forward/backward difference equation was derived to calculate the slope at the highest and lowest flow rates. The derivations followed the standard method of using Taylor series expansions to determine the difference expressions (Lapidus 1962). For a set of data (f_i, x_i) within the highest and lowest flow rate endpoints, Equation B.1 corresponds to the slope df/dx at x_i.

$$\frac{df(x_i)}{dx} = \frac{\frac{h_i}{h_{i+1}} f_{i+1} + \left[\frac{h_{i+1}}{h_i} - \frac{h_i}{h_{i+1}}\right] f_i - \frac{h_{i+1}}{h_i} f_{i-1}}{h_i + h_{i+1}} \qquad \text{(B.1)}$$

where $h_i = x_i - x_{i-1}$
$h_{i+1} = x_{i+1} - x_i$

At the highest and lowest flow data points, the central difference formula given by Equation B.1 cannot be applied. To include the end points in the data analysis, backward and forward difference equations must be applied. These equations have been derived. For the endpoint x_{i-1} at the lowest flow, the slope df/dx is given by Equation B.2.

$$\frac{df(x_{i-1})}{dx} = \frac{f(x_i) - f(x_{i-1})}{h_i} - \frac{h_i}{h_{i+1}^2}[f(x_{i+1}) - f(x_i)] + \frac{h_i}{h_{i+1}} \frac{df(x_i)}{dx} \qquad \text{(B.2)}$$

For the endpoint x_{i+1} at the highest flow, the slope df/dx is given by Equation B.3.

$$\frac{df(x_{i+1})}{dx} = \frac{f(x_{i+1}) - f(x_i)}{h_{i+1}} - \frac{h_{i+1}}{h_i^2}[f(x_{i-1}) - f(x_i)] + \frac{h_{i+1}}{h_i} \frac{df(x_i)}{dx} \qquad \text{(B.3)}$$

Both equations reduce to the standard three point difference relation for equally spaced data (Lapidus 1962). When analyzing real (inherently noisy) data using this technique, care must be taken, because point-by-point derivatives of noisy data can be misleading. Tests with simulated noisy data indicate that these three point difference formulas work reasonably well.

To test the numerical techniques, we have calculated flow rate as a function of pressure drop for a variety of non-Newtonian fluids. We refer to the results of these calculations as simulated data. We then use the numerical techniques for calculating the derivatives. The fluid viscosity as a function of shear rate is then determined with Equations 4.1 - 4.3. As an example of our test calculations, we will show the results for a Bingham Power-Law (BPL) model, which is the simplest expression combining shear thinning/thickening and a yield stress. Suspensions and slurries are generally shear thinning materials at lower shear rates. With the addition of bubbles, slurries are even more likely to be shear thinning, and this will affect the flow properties. The derivation of the flow pressure drop relation for a BPL fluid model is given below.

The BPL viscosity relation is a combination of the Power Law and Bingham Plastic models for fluids.

$$\eta = k \left| \frac{dv_z}{dr} \right|^{n-1} + \tau_o \left| \frac{dv_z}{dr} \right|^{-1} \tag{B.4}$$

The shear stress expression for the viscosity given by Equation B.4 is shown below.

$$\tau_{rz} = -k \left| \frac{dv_z}{dr} \right|^{n} + \tau_o = \frac{-\Delta P r}{2L} \tag{B.5}$$

Combining Equation B.5 for shear stress with the Cauchy momentum equation (Bird et al. 1960), assuming no wall slip, and solving the resulting differential equation gives the following velocity profile expression.

$$V_z = \frac{n+1}{n} \left[\frac{2kl}{\Delta P} \right] \left[\left(\frac{\tau_o}{k} + \frac{\Delta P R}{2kl} \right)^{\frac{n+1}{n}} - \left(\frac{\tau_o}{k} + \frac{\Delta P r}{2kl} \right)^{\frac{n+1}{n}} \right] \tag{B.6}$$

Finally, integrating the velocity profile over the cross-section of the cylindrical tube gives the volumetric flow rate shown in Equation B.7.

$$Q = 2\pi \left(\frac{n}{n+1}\right)\left(\frac{2kl}{\Delta P}\right) *$$

$$\left[\frac{R^2}{2}\left[\frac{\tau_o}{k} + \frac{\Delta PR}{2kl}\right]^{\frac{n+1}{n}} - n\left(\frac{2kl}{\Delta P}\right)^2 \left[\frac{\left(\frac{\tau_o}{k} + \frac{\Delta PR}{2kl}\right)^{\frac{3n+1}{n}}}{3n+1} - \frac{\left(\frac{\tau_o}{k}\right)\left(\frac{\tau_o}{k} + \frac{\Delta PR}{2kl}\right)^{\frac{2n+1}{n}}}{2n+1}\right]\right] \quad \text{(B.7)}$$

Equation B.7 includes both the Power Law and Bingham Plastic models; Equation B.7 correctly reduces to a Power Law model when the yield stress is zero (Equation B.8) and simplifies to the correct Bingham fluid expression when the power law index is set to 1 (Equation B.9).

$$Q = \pi\left(\frac{n}{3n+1}\right) R^{\frac{3n+1}{n}} \left(\frac{\Delta P}{2kL}\right)^{\frac{1}{n}} \quad \text{(B.8)}$$

$$Q = \frac{\pi \Delta P R^4}{8kl}\left[1 - \frac{4}{3}\left(\frac{r_o}{R}\right) + \frac{1}{3}\left(\frac{r_o}{R}\right)^4\right] \quad \text{(B.9)}$$

The capillary rheometry data analysis technique was tested with the Bingham Power Law (BPL) model. Figure B.1 shows simulated flow and pressure drop data for a Bingham-Power Law fluid; the filled squares represent the simulated data. The slope of these data gives the wall shear rate by application of Equation 4.1, and then the viscosity is calculated with Equation 4.3. Figure B.2 shows the viscosity calculated from the simulated data (symbols) and the exact result. As expected, the simulated data and exact result agree.

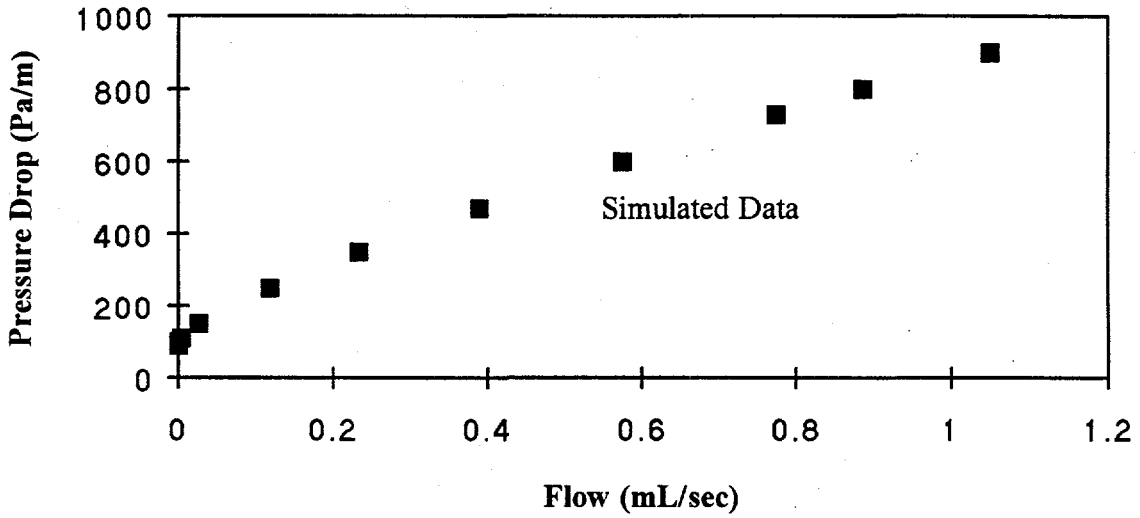

Figure B.1. Simlated Pressure Drop Versus Flow Data for a Bingham Power Law Fluid

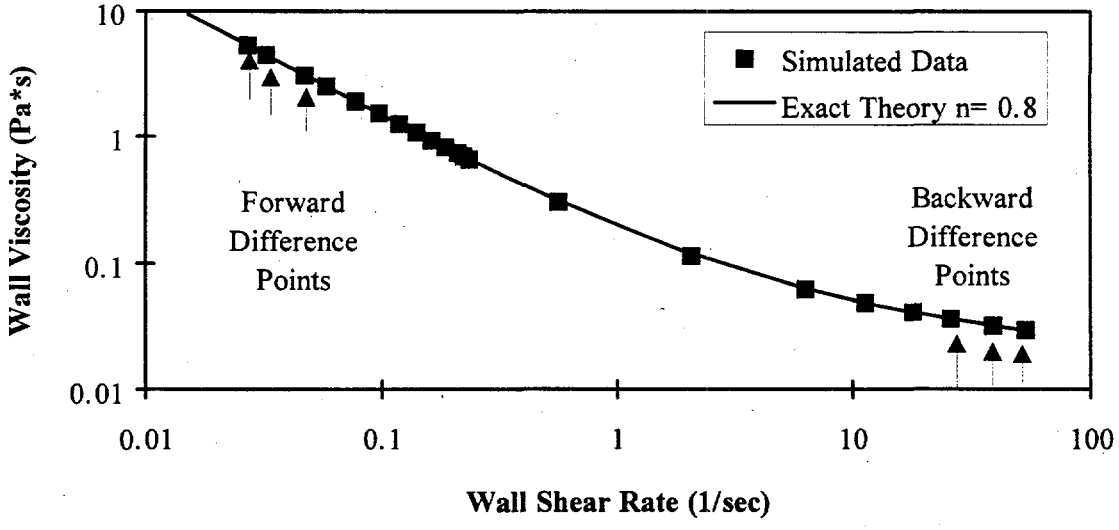

Figure B.2. Simulated and Exact Theoretical Viscosity Data for a Bingham Power Law Fluid

References

Barnes, H. A., J. F. Hutton, and K. Walters. 1989. *An Introduction to Rheology*. Elsevier, New York.

Bird, R. B., W. E. Stewart, and E. N. Lightfoot. 1960. *Transport Phenomena*. John Wiley & Sons, New York.

Lapidus, L. 1962. *Digital Computation for Chemical Engineers*. McGraw-Hill, New York.

Macosko, C. W. 1994. *Rheology: Principles, Measurements, and Applications*. VCH Publishers, New York.

Nguyen, Q. D., and D. V. Boger. 1992. "Measuring the Flow Properties of Yield Stress Fluids." *Annu. Rev. Fluid Mech.*, 24:47–88.

Appendix C

Capillary Rheometry Pressure and Flow Data

Appendix C

Capillary Rheometry Pressure and Flow Data

Table C.1. Capillary Rheometer Data for 0% Gas, 48% Solids, 52% Liquid (302.05-cm length with 0.63-cm internal diameter [1/4 in. tube])

Pressure Drop (Pa)	Flow Rate (cc/sec)	Shear Rate (1/sec)	Viscosity (Pa*sec)
2068.42	0.124557	5.171321	0.20920
3998.945	0.249113	10.02416	0.20865
6136.313	0.37367	14.91593	0.21517
8273.68	0.498226	19.92034	0.21723
10479.99	0.622783	24.78326	0.22117
11858.94	0.74734	33.74366	0.18381
13375.78	0.871896	37.65899	0.18577
15857.89	0.996453	38.04948	0.21798

Table C.2. Capillary Rheometer Data for 0% Gas, 48% Solids, 52% Liquid (396.24-cm length with 0.980-cm internal diameter [3/8 in. tube])

Pressure Drop (Pa)	Flow Rate (cc/sec)	Shear Rate (1/sec)	Viscosity (Pa*sec)
429.3819	0.123833	1.299685	0.204366
1033.342	0.248667	2.609866	0.244922
1599.254	0.373167	3.897026	0.253856
2278.64	0.497604	5.126364	0.27496
2860.095	0.622783	6.709583	0.263686
3427.184	0.74734	8.093146	0.261953
4062.381	0.871896	9.203266	0.27305
4774.286	0.99583	10.28669	0.287102

Table C.3. Capillary Rheometer Data for 5% Gas, 48% Solids, 47% Liquid (302.06-cm length with 0.63-cm internal diameter [1/4 in. tube])

Pressure Drop (Pa)	Flow Rate (cc/sec)	Shear Rate (1/sec)	Viscosity (Pa*sec)
2323.525	0.116513	2.676836	0.454006
3343.946	0.145642	7.272433	0.2405
3626.63	0.17477	8.802107	0.215502
5467.523	0.233027	9.588427	0.298249
7377.365	0.34954	14.52192	0.265713
10342.1	0.466053	20.03633	0.269977
12065.78	0.582567	24.88712	0.253581
14547.89	0.69908	27.74204	0.274282
20339.46	0.932107	35.58727	0.298937

Table C.4. Capillary Rheometer Data for 5% Gas, 48% Solids, 47% Liquid (253.59-cm length with 0.98-cm internal diameter [3/8 in. tube])

Pressure Drop (Pa)	Flow Rate (cc/sec)	Shear Rate (1/sec)	Viscosity (Pa*sec)
689.4733	0.145642	1.59879	0.414661
827.368	0.17477	1.918547	0.414661
1103.157	0.233027	2.535135	0.418411
1723.683	0.34954	3.917984	0.423021
2199.42	0.466053	5.417445	0.390374
2619.999	0.582567	6.437909	0.391312
3585.261	0.69908	8.753608	0.393822
4136.84	0.932107	13.96208	0.284895

Table C.5. Capillary Rheometer Data for 12% Gas, 48% Solids, 40% Liquid (302.06-cm length with 0.63-cm internal diameter [1/4 in. tube])

Pressure Drop (Pa)	Flow Rate (cc/sec)	Shear Rate (1/sec)	Viscosity (Pa*sec)
3102.63	0.059267	2.412725	0.672601
5860.523	0.118533	4.957471	0.618318
7101.575	0.148167	6.248206	0.594477
8273.68	0.1778	7.428437	0.582555
10893.68	0.237067	9.871782	0.577184
15168.41	0.3556	14.37521	0.551901
22201.04	0.474133	18.96778	0.612199
27303.14	0.592667	23.4617	0.608679
34956.3	0.7112	30.54656	0.598548
41713.14	0.948267	47.83065	0.456144

Table C.6. Capillary Rheometer Data for 12% Gas, 48% Solids, 40% Liquid (253.59-cm length with 0.98-cm internal diameter [3/8 in. tube])

Pressure Drop (Pa)	Flow Rate (cc/sec)	Shear Rate (1/sec)	Viscosity (Pa*sec)
1620.262	0.118533	1.38404	1.12565
2275.262	0.1778	2.017153	1.084574
2964.735	0.237067	2.679298	1.063975
4205.787	0.3556	4.559829	0.886881
4895.261	0.474133	5.872497	0.80153
6343.155	0.592667	6.340971	0.96187
7722.101	0.7112	14.73842	0.503792
8135.785	0.948267	24.65566	0.317285

Table C.7. Capillary Rheometer Data for 16% Gas, 48% Solids, 36% Liquid (302.06-cm length with 0.63-cm internal diameter [1/4 in. tube])

Pressure Drop (Pa)	Flow Rate (cc/sec)	Shear Rate (1/sec)	Viscosity (Pa*sec)
10617.89	0.116513	4.636234	1.197866
14478.94	0.17477	7.36272	1.02857
18994.99	0.233027	10.0046	0.993059
25096.83	0.34954	14.88179	0.882062
33784.19	0.466053	21.9228	0.806034
37921.03	0.582567	30.94904	0.640868
40816.82	0.69908	36.63817	0.582694
58812.07	0.932107	39.92377	0.770496

Table C.8. Capillary Rheometer Data for 15% Gas, 48.5% Solids, 36.5% Liquid (253.59-cm length with 0.95-cm internal diameter [3/8 in. tube])

Pressure Drop (Pa)	Flow Rate (cc/sec)	Shear Rate (1/sec)	Viscosity (Pa*sec)
3743.84	0.087385	1.744877	2.014741
4102.366	0.116513	1.893605	2.034285
5074.524	0.145642	2.181045	2.184728
5467.523	0.17477	2.650339	1.937117
7239.47	0.233027	3.277824	2.0739
8666.68	0.34954	5.233755	1.554913
10052.52	0.466053	6.471493	1.458603
11686.57	0.582567	7.212761	1.521431
14906.41	0.69908	7.818692	1.790217
20835.88	0.932107	10.77436	1.81588

Table C.9. Capillary Rheometer Data for 15% Gas, 48.5% Solids, 36.5% Liquid (304.8-cm length with 1.30-cm internal diameter [1/2 in. tube])

Pressure Drop (Pa)	Flow Rate (cc/sec)	Shear Rate (1/sec)	Viscosity (Pa*sec)
3081.946	0.116513	0.521901	6.274304
3888.63	0.17477	1.159677	3.562776
4274.735	0.233027	1.547338	2.935303
6722.365	0.34954	1.555066	4.593062
10080.1	0.466053	2.334325	4.588096
11714.15	0.582567	4.995853	2.491323
12148.52	0.69908	6.138277	2.102838
15306.31	0.932107	4.635311	3.508492

Table C.10. Capillary Rheometer Data for 20% Gas, 48% Solids, 32% Liquid (254.20-cm length with 0.98-cm internal diameter [3/8 in. tube])

Pressure Drop (Pa)	Flow Rate (cc/sec)	Shear Rate (1/sec)	Viscosity (Pa*sec)
8618.417	0.08875	1.368735	6.055663
9721.574	0.118333	1.64766	5.674431
12755.26	0.1775	2.080414	5.89648
14478.94	0.207083	2.382909	5.843629
16133.68	0.236667	2.861455	5.422504
18408.94	0.295833	3.788537	4.673159
20477.36	0.355	4.571795	4.307652
27303.14	0.591667	7.558321	3.474088
30474.72	0.71	8.429072	3.47707
36266.3	0.828333	12.30789	2.833824
37989.98	0.946667	16.2272	2.251536

Table C.11. Capillary Rheometer Data for 20% Gas, 48% Solids, 32% Liquid (304.8-cm length with 1.30-cm internal diameter [1/2 in. tube])

Pressure Drop (Pa)	Flow Rate (cc/sec)	Shear Rate (1/sec)	Viscosity (Pa*sec)
6377.628	0.059167	0.639647	10.5937
6894.733	0.08875	0.745768	9.822964
8549.469	0.118333	0.902296	10.06744
9032.101	0.147917	1.12048	8.564729
9652.627	0.1775	1.132801	9.053589
11445.26	0.236667	1.273923	9.545777
15168.41	0.355	1.826447	8.823931
18753.67	0.473333	2.764869	7.206771
20684.2	0.591667	3.778144	5.816867
22201.04	0.71	4.360207	5.409974
24131.57	0.828333	4.620008	5.549728
26131.04	0.946667	5.094475	5.449871

Table C.12. Capillary Rheometer Data for 17% Gas, 46% Solids, 37% Liquid (302.06-cm length with 0.63-cm internal diameter [1/4 in. tube])

Pressure Drop (Pa)	Flow Rate (cc/sec)	Shear Rate (1/sec)	Viscosity (Pa*sec)
8480.522	0.0889	3.788934	1.170687
10479.99	0.118533	5.374609	1.019881
12065.78	0.148167	6.548746	0.96368
14134.2	0.1778	7.291049	1.013951
19581.04	0.237067	9.302864	1.100917
30750.51	0.3556	18.48212	0.870234
34542.61	0.474133	28.68889	0.629763
35852.61	0.5334	30.32133	0.618455
40678.93	0.592667	22.85583	0.930911
51089.97	0.7112	46.82967	0.570624

Table C.13. Capillary Rheometer Data for 17% Gas, 46% Solids, 37% Liquid (254.20-cm length with 0.98-cm internal diameter [3/8 in. tube])

Pressure Drop (Pa)	Flow Rate (cc/sec)	Shear Rate (1/sec)	Viscosity (Pa*sec)
1978.788	0.059267	1.268402	1.496464
2185.63	0.0889	1.551281	1.351482
3102.63	0.118533	1.967233	1.512858
3309.472	0.148167	2.772406	1.145053
3461.156	0.1778	3.069883	1.081492
3847.261	0.207433	2.383143	1.548551
5033.155	0.237067	2.426424	1.989745
7377.365	0.3556	4.23229	1.672052
8963.153	0.474133	6.16912	1.393675
10080.1	0.592667	7.375514	1.310981
12307.1	0.7112	9.647695	1.223647
13789.47	0.948267	15.91672	0.831032

Table C.14. Capillary Rheometer Data for 23% Gas, 38% Solids, 39% Liquid (302.06-cm length with 0.63-cm internal diameter [1/4 in. tube])

Pressure Drop (Pa)	Flow Rate (cc/sec)	Shear Rate (1/sec)	Viscosity (Pa*sec)
2482.104	0.058257	2.61301	0.496838
3585.261	0.095005	4.040067	0.46416
4619.471	0.126673	5.184972	0.465995
5791.576	0.158341	6.275297	0.482723
7136.049	0.190009	7.722886	0.483297
9059.68	0.253345	10.57819	0.447957
13444.73	0.380018	15.05146	0.467206
18960.52	0.506691	21.06661	0.470751
22614.73	0.633364	30.41421	0.388911
24758.99	0.760036	36.63633	0.353473
32198.4	1.013382	41.6465	0.404382

Table C.15. Capillary Rheometer Data for 23% Gas, 38% Solids, 39% Liquid (254.20-cm length with 0.98-cm internal diameter [3/8 in. tube])

Pressure Drop (Pa)	Flow Rate (cc/sec)	Shear Rate (1/sec)	Viscosity (Pa*sec)
2187.009	0.126673	3.307153	0.637641
2275.262	0.158341	3.259475	0.673076
2413.157	0.190009	2.964661	0.784857
2792.367	0.253345	3.274977	0.822137
3716.261	0.380018	4.262304	0.840701
5267.576	0.506691	8.032859	0.632296
5639.892	0.633364	9.622993	0.56512
6494.839	0.760036	8.683454	0.7212
8411.575	1.013382	10.94276	0.741192

Table C.16. Capillary Rheometer Data for 17% Gas, 50% Solids, 33% Liquid (82.60-cm length with 0.63-cm internal diameter [1/4 in. tube])

Pressure Drop (Pa)	Flow Rate (cc/sec)	Shear Rate (1/sec)	Viscosity (Pa*sec)
6212.844	0.057155	2.653654	4.47802
9721.574	0.11431	5.184146	3.586734
11307.36	0.142887	8.115445	2.664948
11996.84	0.171465	9.922707	2.312472
14065.26	0.22862	11.27998	2.38495
17236.83	0.342929	15.43427	2.136049
19856.83	0.400084	16.72702	2.270551
22221.73	0.457239	19.87935	2.138038
25855.25	0.571549	26.92221	1.836868
28613.14	0.685859	32.90638	1.663127
31302.09	0.800169	44.7193	1.338808

Table C.17. Capillary Rheometer Data for 17% Gas, 50% Solids, 33% Liquid (123.20-cm length with 0.98-cm internal diameter [3/8 in. tube])

Pressure Drop (Pa)	Flow Rate (cc/sec)	Shear Rate (1/sec)	Viscosity (Pa*sec)
1765.052	0.057155	0.691263	5.079998
2806.156	0.11431	1.394136	4.004576
3661.103	0.171465	2.084043	3.495064
4447.103	0.22862	2.822384	3.134808
5660.576	0.342929	4.074307	2.764118
7377.365	0.457239	4.860467	3.019764
9866.363	0.571549	8.472452	2.316849
10515.16	0.685859	9.939363	2.104781
12920.73	0.800169	10.76088	2.388851
13686.05	0.914479	13.99455	1.945669

Table C.18. Capillary Rheometer Data for Water (304.8-cm length with 0.32-cm internal diameter [1/8 in. tube])

Pressure Drop (Pa)	Flow Rate (cc/sec)	Shear Rate (1/sec)	Viscosity (Pa*sec)
682.5786	0.058257	611.9409	0.0000915
1309.999	0.116513	1187.266	0.0000905
2757.893	0.233027	2325.237	0.0000973
5929.471	0.466053	4587.542	0.000106
13789.47	0.932107	9070.247	0.000125

Table C.19. Capillary Rheometer Data for Supernatant Solution of 66 wt% Glycerol, 34 wt% Water (243.84-cm length with 0.32-cm internal diameter [1/8 in. tube])

Pressure Drop (Pa)	Flow Rate (cc/sec)	Shear Rate (1/sec)	Viscosity (Pa*sec)
27385.88	1.25	401.8635	0.022183
22021.78	1	318.7682	0.022488
16437.04	0.75	240.7802	0.022222
11369.42	0.5	161.4595	0.022922
8707.359	0.38	121.2892	0.023369
5857.076	0.257	81.13403	0.023499
2895.788	0.133	41.29496	0.022827

Appendix D

Shear and Tensile Strength Data

Appendix D

Shear and Tensile Strength Data

Table D.1. Shear Strengths of 80-110 μm Glass Beads Mixed with Air and Water

Weights, g		Gas Saturation	Shear Strength, kdyn/cm^2		Replicates
Glass Beads	Water		Value	95% C. I.	
1000.0	224.8	0.128	16.3	9.1	3
1000.0	210.6	0.183	23.5	7.7	3
1000.0	200.1	0.224	36.4	2.0	3
1000.0	186.3	0.278	37.0	4.2	6
1000.0	161.3	0.374	39.0	3.1	5
1000.0	148.1	0.426	40.4	1.5	3
1000.0	136.2	0.472	36.6	2.8	5
1000.0	123.8	0.520	36.8	4.7	3
1000.0	111.4	0.568	41.0	3.7	3
1000.0	99.0	0.616	41.0	4.2	3
1000.0	99.0	0.616	39.9	4.8	4
1000.0	86.5	0.664	40.1	3.2	6
1000.0	74.2	0.712	38.9	3.6	3
1000.0	61.9	0.760	36.8	3.8	5
1000.0	49.6	0.808	37.0	3.9	3
1000.0	49.4	0.809	39.2	3.0	3
1000.0	37.2	0.856	34.1	6.4	3
1000.0	24.9	0.903	31.9	7.2	3
1000.0	12.4	0.952	26.4	1.9	3
1000.0	0.0	1.000	11.8	2.9	3

Table D.2. Tensile Strengths of 80-110μm Glass Beads Mixed with Air and Water

Weights, g		Gas Saturation	Tensile Strength, kdyn/cm^2		Replicates
Glass Beads	Water		Value	95 % C. I.	
1000.0	200.1	0.224	23.3	11.5	1
750.0	130.0	0.328	17.9	9.0	2
1000.0	148.1	0.426	10.0	3.2	7
1000.0	99.0	0.616	10.2	3.8	4
1000.0	49.4	0.809	7.7	2.2	4

Table D.3. Shear Strengths of 1-60μm Glass Beads Mixed with Air and Water

Weights, g		Gas Saturation	Shear Strength, kdyn/cm^2		Replicates
Glass Beads	Water		Value	95 % C. I.	
1000.0	202.8	0.341	26.8	6.5	4
1000.0	175.8	0.429	68.1	3.2	3
1000.0	149.2	0.516	80.3	0.6	3
1000.0	125.8	0.591	81.9	14.6	4
1000.0	100.3	0.674	81.1	12.4	4
1000.0	73.2	0.762	82.8	6.1	3
1000.0	50.5	0.836	67.4	4.2	3
1000.0	23.2	0.925	60.5	6.9	3
1000.0	0.0	1.000	17.5	0.5	3

Table D.4. Shear and Tensile Strengths of Bubbly Clay Sludges

Weight Fraction Bentonite Clay		Clay Sludge Densities, g/cm³		Gas Fraction	Shear Strength, kdyn/cm²		Tensile Strength, kdyn/cm²		
As Is	Oven Dry	No Gas, Estimated	With Gas, Measured		Value	95 % C.I.	Value	95 % C.I.	Replicates
0.175	0.161	1.1135	1.1041	0.008	5.2	0.3	10.6	1.6	5
0.175	0.161	1.1134	1.0378	0.068	4.7	0.3	8.2	0.3	3
0.175	0.161	1.1134	0.9565	0.141	4.0	0.2	5.5	0.3	12
0.175	0.161	1.1135	0.8992	0.192	4.1	0.3	4.7	0.7	6
0.208	0.191	1.1374	1.1196	0.016	13.8	0.7	25.3	2.6	3
0.208	0.191	1.1374	1.0599	0.068	12.6	0.6	19.4	3.0	3
0.208	0.191	1.1374	0.9982	0.122	11.2	1.1	10.3	0.7	6
0.208	0.191	1.1374	0.9403	0.173	11.6	0.5	7.7	0.8	5
0.240	0.221	1.1624	1.1510	0.010	30.5	1.2	44.8	7.7	2
0.240	0.221	1.1624	1.0863	0.066	20.0	1.0	29.6	5.7	2
0.240	0.221	1.1624	1.0157	0.126	18.8	0.7	13.3	7.5	2
0.239	0.220	1.1618	1.0074	0.133	18.9	1.0	11.4	1.2	3
0.239	0.220	1.1618	0.9708	0.164	18.9	1.0	8.3	1.7	5
0.272	0.251	1.1885	1.1707	0.015	35.0	0.7	54.6	19.8	2

Appendix E

Retained Bubble Distribution and Rollover Model

Appendix E

Retained Bubble Distribution and Rollover Model

L. A. Mahoney, Pacific Northwest Laboratory

Introduction

It is important to be able to predict the distribution of gas bubble shapes in waste tank sludge, together with the distribution of bubble sizes. The bubble shape and size potentially affect the sludge strength, the gas production rate, and the tendency of gas to percolate through the sludge rather than be trapped in it. These properties, in turn, affect the rollover behavior of the sludge -- its tendency to accumulate a buoyant underlayer as a result of gas generation and to become unstable as a result.

This model (which is named BOND6) was designed to calculate the distribution of bubble sizes and shapes in a bed of sludge and to estimate the effect of rollover occurrences on the bubble sizes. It also calculates the amount of gas released at each rollover.

Some of the phenomena this model includes are

- Sludge density variation because of gas fraction
- Bubble size that varies with depth in the sludge resettled after a rollover
- Gas generation rate that varies with depth
- Gas generation depending on the local liquid volume fraction in the sludge
- Rollover involving all the sludge down to the level at which the integrated net sludge weight is zero -- the sludge strength is assumed to have no effect on rollover timing
- Sludge weight and sludge yield strength are both included in the Bond number
- Sludge strength varying with depth and with time since the last disturbance (rollover); the gas content is assumed to have no direct effect on the sludge shear strength
- Percolation of gas out of sludge regions where the gas concentration has reached a percolation threshold
- Gas escape from sludge regions that have an uninterrupted percolation route to the supernatant
- A different percolation threshold for dendritic bubbles than for sludge-displacing bubbles.

Based on the results of modeling, it appears that the most important BOND6 input parameters, for the purpose of predicting rollover, are those that determine the vertical distribution of the sludge density. These include the supernatant liquid depth, the sludge depth, the liquid, solid and sludge densities, the retained gas fraction, and variation of gas generation rate with depth (which can be estimated from the temperature profiles). The bubble shape parameters, the yield strength, ductility, surface tension, pore size, and initial bubble size, pertain chiefly to predicting whether percolation occurs. Percolation may prevent rollover -- if gas is released through gas-filled paths, rather than accumulating -- or may permit faster gas release and higher gas concentrations in the dome space, if a group of large "fracture bubbles" are formed between an upper non-percolating layer and a lower percolating layer. Except for these situations, bubble shape does not directly affect rollover; it does change waste properties such as thermal conductivity, density, and so on that influence rollover.

BOND6 performs well in predicting the rollover behavior of Tank 241-SY-101 before December 1991. Its predictions do not provide such a good match after that time. Model predictions for other tanks have not been possible because of inadequate waste density characterization.

Problem Definition

For the model's purposes, a waste tank (or other system containing a wet agglomerate) is defined as a slab, or column, of a mixture of solid particles and interstitial liquid. There may be a layer of supernatant liquid on top of the sludge. Gas bubbles are initially present in the sludge and grow as the result of gas generation. The model considers only the depth dimension of this system, not any cross-sectional inhomogeneities.

Further, BOND6 treats the sludge as a solid, in that the sludge is assumed not to flow until some yield point is reached at rollover. Thus the model considers the statics, not the dynamics, of the system and does not account for the sludge rheological behavior.

Force balance around the bubble, and bubble shape

The central concept of BOND6 is that, if the size and environment of a bubble in sludge are known, its shape (theoretically) can be found by performing a force balance on the bubble. If the bubble's equivalent spherical diameter is greater than the sludge pore diameter, then the bubble cannot expand to a sphere without displacing sludge. Its internal pressure must supply the force required to support the sludge net weight and to yield the sludge. When the bubble can provide that force, it displaces sludge particles and takes on a roughly spherical shape (as seen in "Swiss-cheese sludge"); otherwise, the bubble fingers between the particles and assumes a dendritic shape. A dimensionless number akin to a Bond number can be derived to express the force balance and define the bubble shape.

As long as a bubble is small enough to fit within a pore of diameter D_p, it is spherical and can expand without either supporting sludge weight or displacing sludge volume in order to expand. It is only when the bubble's equivalent spherical diameter D is greater than D_p that it must either displace sludge or finger through the pores.

We want to estimate the force required for a single bubble to displace enough sludge to allow itself to become spherical. Such an estimate depends on knowing the shear strength τ_s of the sludge, the fractional strain ϵ_s at which the sludge "fails" (flows freely), and the distance from the bubble at which that "fractional failure strain" is reached as a result of bubble expansion. (The fractional linear strain is defined as the absolute strain divided by the original length.)

Consider a dendritic bubble attempting to expand and become a spherical one. It has to expand and displace sludge outward from the central point in the sphere, at the same time "pulling in its tentacles" from the dendritic extremities of the pore space it occupies. It expands from its initial volume, α of the volume contained in the final sphere occupied by the bubble, to 100% of that volume. That means that a volume fraction $(1 - \alpha)$ of the final bubble's volume is displaced during the expansion. (Here α is the void volume fraction in the sludge.)

To simplify, think of the bubble as a sphere of volume α that has expanded to a sphere of volume = 1.0; at the final spherical bubble surface, the expansion has caused a fractional linear strain that is equal to the added radius divided by the original radius. So the fractional linear strain at the bubble surface equals $([1/\alpha]^{1/3} - 1)$. At some distance from the bubble center corresponding to a diameter D_s the linear strain will have decreased to ϵ_s (and the stress will have decreased to τ_s). Assume that the volumetric strain is constant with distance from the bubble center. Then the fractional linear strain varies with distance from the bubble at a rate proportional to $1/r^2$, giving

$$D_s = D(\{[1/\alpha]^{1/3}-1\}/\epsilon_s)^{1/2} \qquad (E.1)$$

The stress at D_s is τ_s. This stress multiplied by the surface area of the D_s sphere gives the force at the spherical surface with diameter D_s, or

$$F_e = \tau_s\pi(D_s)^2 = \tau_s\pi D^2((1/\alpha)^{1/3}-1)/\epsilon_s \qquad (E.2)$$

This is the force that the bubble would have to supply to move the sludge and expand it.

However, the above only describes the effect of a single isolated bubble. What of the case where there is a significant void fraction α and more than one bubble at once is contained within any given sphere of diameter D_s? Because all these bubbles are within each other's sphere of influence (the sphere within which sludge yield occurs), the sludge displacement forces they exert will tend to add together and assist each other in displacing sludge. Then in each such volume of diameter D_s there will be a number of bubbles N_v roughly equal to

$$N_v = N_0(\pi D_s^3/6) = (\pi N_0 D^3/6)\ ((1/\alpha)^{1/3}-1)^{3/2} / \epsilon^{3/2} \qquad (E.3)$$

Here N_0 is the original, pregas-evolution number of bubbles per unit volume; this number density is assumed to remain constant throughout bubble growth. Treating the forces applied by all these bubbles within D_s as linearly additive, which is an extremely rough approximation, then the required sludge-displacement force F_{eb} per bubble is only F_e/N_v, or

$$F_{eb} = (6\tau_s\epsilon_s^{1/2}/N_0 D) / ((1/\alpha)^{1/3}-1)^{1/2} \qquad (E.4)$$

Note that the sludge displacement force does not depend on the depth of sludge. The disconcerting thing about the above expression is that the required force decreases with increasing bubble size D; this happens because larger bubbles have larger sludge displacement volumes that contain more other bubbles to help strain the sludge. Note that the change in sludge strength τ_s that would be expected to result from the presence of a significant void fraction is not included above. Presumably, the effect of dendritic bubbles on sludge strength would differ from that of sludge-displacing bubbles. If information on the dependence of the sludge strength and failure strain on void fraction were to become available, it could be added to the model fairly easily.

Gauglitz et al. (1994) developed a description of the force balance for the bubble with only the sludge weight force included. Here, the net weight force that was applied to the bubble depended on the bubble depth and the net density of the sludge (the amount by which sludge density exceeds supernatant density). The expanding force of the bubble comes from its internal pressure increment, which depends on the liquid-gas surface tension and the pore diameter; this is the curvature diameter governing the liquid-gas interface. The force balance gives a weight-based Bond number Bo_w of

$$\#Bo_w = (\rho_s - \rho_l)D_p gh/4\sigma \quad (E.5)$$

The bubble must first overcome the weight force, that is, have a $\#Bo_w$ of less than or equal to unity, before it can possibly move sludge and reach a quasi-spherical form. It meets these conditions at a pore diameter that is less than or equal to D_{pw}, which is

$$D_{pw} = 4\sigma/(\rho_s - \rho_l)gh \quad (E.6)$$

With sludge yield forces included, the new Bond number, $\#Bo_y$, can be calculated by a force balance:

bubble lift force (encouraging expansion) $= (P_L + \rho_l gh + 4\sigma/D_p)A_b$

sludge force down (resisting expansion) $= (P_L + \rho_s gh)A_b$

resisting yield force (resisting expansion) $= (6\tau_s\epsilon_s^{1/2}/N_0D) \; / \; ((1/\alpha)^{1/3}-1)^{1/2}$

where P_L = a reference pressure at the top of the sludge layer
ρ_l = the liquid density
ρ_s = the sludge density, liquid, solids, gas, and all
g = gravitational acceleration
σ = surface tension (liquid/gas)
A_b = contact area between the bubble and the particle(s)

When the expanding and resisting forces on the bubble are equal, $\#Bo_y = 1$ and

$$(P_L + \rho_l gh + 4\sigma/D_p)A_b = (P_L + \rho_s gh)A_b + (6\tau_s\epsilon_s^{1/2}/N_0D) \; / \; ((1/\alpha)^{1/3}-1)^{1/2} \quad (E.7)$$

As an approximation, we can take $A_b = (\pi/4)D^2(1-\alpha)^{2/3}$. This expression accounts for the area fraction that is occupied by solid at any given value of volumetric void fraction α. Dividing through by A_b,

$$(\rho_s - \rho_l)gh = 4\sigma/D_p - (24\tau_s\epsilon_s^{1/2} \; / \; \pi N_0D^3) \; / \; \{((1/\alpha)^{1/3}-1)^{1/2} \; (1-\alpha)^{2/3}\} \quad (E.8)$$

It follows that the Bond number, with the sludge strength accounted for, is of the form

$$\#Bo_y = \#Bo_w + (6\tau_s\epsilon_s^{1/2}D_p \; / \; \pi\sigma N_0D^3) \; / \; \{((1/\alpha)^{1/3}-1)^{1/2} \; (1-\alpha)^{2/3}\} \quad (E.9)$$

Because $\alpha = \pi N_0D^3/6$, the new Bond number $\#Bo_y$ can be expressed more simply as

$$\#Bo_y = \#Bo_w + (\tau_s\epsilon_s^{1/2}D_p \; / \; \sigma) \; / \; \{\alpha \; ((1/\alpha)^{1/3}-1)^{1/2} \; (1-\alpha)^{2/3}\} \quad (E.10)$$

Here, a Bond number greater than 1 indicates that bubble-constricting forces prevail and bubbles are dendritic. A Bond number less than 1 indicates that the bubbles displace the sludge. Note that the sludge weight force could more accurately be expressed as an integral over depth of the variable sludge density; the model handles it this way, in fact.

Probably the two biggest conceptual uncertainties in the derivation of Equation E.10 are a) whether the compressive yield strength and failure strain are more appropriate than the same properties for shear and b) the effect of multiple bubble expansions on the sludge around the bubbles. These two questions are related, in that sludge being displaced by bubbles expanding in many different directions would undergo both compression and shear. Sludge displaced by only one bubble would only undergo compression (in the radial direction).

It isn't clear how to add the forces on sludge that result from several nearby bubbles expanding simultaneously. The above derivation added the forces linearly to obtain a linear average of the required force per bubble. A root-mean-square average would give a different result, with a larger effect of the sludge yield strength on the Bond number. The derivation is outlined below:

$$
\begin{aligned}
N_v &= N_0(\pi D_s^3/6) = \alpha((1/\alpha)^{1/3}-1)^{3/2} / \epsilon^{3/2} \\
F_{eb} &= F_e / (N_v)^{1/2} = (\pi \tau_s D^2/\alpha^{1/2})\ ((1/\alpha)^{1/3}-1)^{1/4} / \epsilon_s^{1/4} \\
(\rho_s - \rho_l)gh &= 4\sigma/D_p - (4\tau_s/\alpha^{1/2})\ ((1/\alpha)^{1/3}-1)^{1/4} / \epsilon_s^{1/4}(1-\alpha)^{2/3} \\
\#Bo_y &= \#Bo_w + (\tau_s D_p/\sigma\epsilon_s^{1/4})\ ((1/\alpha)^{1/3}-1)^{1/4} / \alpha^{1/2}(1-\alpha)^{2/3}
\end{aligned}
\qquad \text{(E.11)}
$$

This result is somewhat similar to that of the first derivation but implies a greater likelihood of dendritic bubbles. A comparison of Equations E.10 and E.11 gives some idea of the uncertainty in the Bond number that results from the interactions between bubbles. The computer model allows either Equations E.10 or E.11 to be used to calculate the Bond number, as the modeler prefers.

A less approximate form for the effect of the presence of multiple bubbles could probably be found using a free-cell derivation of 3-D stress and strain variation around a population of spherical holes containing pressure. A 2-D free-cell model of pressurized circular holes in a plate under tension has been derived (see the Appendix F), but the constraints on a 2-D model are such as to make it of dubious applicability to the 3-D case except for calculating stress concentration factors.

Post-rollover bubble-size distribution

The model begins by assuming that a complete rollover has recently been completed and the sludge has just resettled. The initial bubble size distribution in the sludge is derived by assuming that some fraction of the gas in the sludge was retained after the rollover because a fraction of the bubbles were too small to escape. These bubbles are assumed to have been all the same size when they were at the surface of the supernatant, at atmospheric pressure. Because of the hydrostatic pressure in the liquid in the sludge pores, the bubbles have a depth-dependent size distribution in the resettled sludge. The hydrostatic pressure is

$$P = P_0 + \rho_l g\Delta + \int_{\Delta}^{\Delta+L}(1 - \alpha)\rho_l g d\xi \qquad \text{(E.12)}$$

Here Δ is the depth of the supernatant and L the additional depth of the sludge alone.

Equation E.12 treats the gas density as zero and assumes that the bubbles are sludge-displacing. For dendritic bubbles, which displace liquid without displacing particles, the term in the integral is $(1\ \alpha)\rho_l g\ dx]/\phi$, where ϕ is the pore volume fraction (or maximum liquid volume fraction) of the sludge. The local void fraction α, for bubbles that occupied a void fraction of α_0 while at the supernatant surface at pressure P_0, can be expressed as

$$\alpha = (P / P_0)\ \alpha_0 \qquad \text{(E.13)}$$

Using Equations E.12 and E.13, a transcendental expression for the initial bubble size distribution (assuming small, sludge-displacing bubbles) can be derived:

$$(1/\alpha - 1)\exp(1/\alpha) = (1/\alpha_\Delta - 1)\exp(\rho_l gx / \alpha_0 P_0)\exp(1/\alpha_\Delta) \qquad \text{(E.14)}$$

where x = depth below the top of the sludge layer
α_Δ = void fraction at the top of the sludge layer
= $(P_0/P_L)\alpha = (P_0 / (P_0+\rho_l g\Delta))\alpha$

To use Equation E.14 in a discrete numerical form, BOND6 divides the bed into a number of depth increments of equal size and calculates the initial bubble size for each increment. The bubble size is taken as uniform at any given depth, with no cross-sectional variation. In addition, the pore volume fraction (which sets the gas-free sludge density) is treated as constant with depth.

An analytical solution being unavailable, Equation E.14 is solved numerically at each depth increment. After the void fraction has been found, the corresponding bubble diameter and Bond number are calculated and adjustments to the pressure are made if the bubble is dendritic.

The process of bubble sizing is necessarily iterative. The local density depends on whether the local bubbles are dendritic or sludge-displacing, which in turn depends on the pressure above them, which in turn depends on how much liquid has been forced out of the sludge into the supernatant layer, which depends in part on the shape of the local bubbles. Therefore the model iterates until a constant value of the new supernatant depth has been determined, and this is taken as evidence that a consistent bubble size distribution has been calculated.

Gas generation

With the initial gas bubble size distribution known, the next step is to add the gas produced at each depth increment during each time step. The model does not use time as an explicit independent variable; rather, it uses a gas generation increment (per unit liquid) as the time-like variable. It is therefore appropriate to speak not of a "time step" but of a "gas volume increment."

The gas generation is treated as linearly dependent on the amount of liquid present, or (ϕ - α). Thus the gas generation in a modeled depth increment of sludge is affected by the bubble shape. A higher volume fraction of liquid can be present in the "Swiss-cheese" regime, in which liquid remains in the pores of the sludge between bubbles, than in the dendritic regime, in which the gas may entirely expel the liquid from the pores.

Gas generation is also treated as dependent on depth, using depth as a surrogate for temperature. The temperature in the sludge is assumed to vary parabolically with depth, as in a slab with finite constant thermal conductivity and volumetric heat generation. Further, the gas generation rate is assumed to depend on the local temperature. By this reasoning, the gas generation per unit of liquid is assumed to vary parabolically with depth. The two inputs governing this variation are the overall average gas generation increment per unit liquid volume and the ratio of peak generation to the minimum generation (at the sludge surface), or $<R>$ and b. At any given depth x below the sludge surface, the local gas generation increment per unit liquid volume, R, is

$$R = (3<R>/(2b+1))\,[b - 4(b-1)(x/L - 0.5)^2] \qquad \text{(E.15)}$$

To put it more exactly, R is the gas volume that is generated at a pressure of P_0 per unit of liquid volume present. The model uses the following expression to calculate the change in void fraction in a depth increment containing dendritic bubbles:

$$\alpha_{new} = \alpha_{old}\,(P_{old}/P_{new}) + R(\phi - \alpha_{old})(P_0/P_{new}) \qquad \text{(E.16)}$$

In a depth increment containing sludge-displacing bubbles, the second term is

$$R\phi(1 - \alpha_{old})(P_0/P_{new})$$

The difference in gas generation for sludge-displacing versus dendritic bubbles makes an iterative solution necessary for each "time" step, as for the initial gas bubble size distribution.

Percolation

At some point in "time," or gas generation, there is enough gas in the sludge that some of the bubbles interconnect with each other across one or more of the model's depth increments. The formation of this "percolation network" allows some of the gas in those depth increments to escape and flow to the top of the percolating region. The maximum amount of gas that could so escape is the volume fraction in excess of the percolation threshold; however, not all the gas volume is interconnected, so some of that excess remains in the sludge. (Predicting the resulting cross-sectional variation in void fraction is beyond the abilities of the present model.)

This percolation process is believed to account for the gas-filled "fractures" that have been observed in wet sand columns in recent experiments (Gauglitz et al. 1994). After a certain amount of gas generation in a sand bed, percolation occurs in the lower part of the bed where the bubbles are dendritic, and after that point much of the generated gas flows up through the pore network to the top of the percolating region. Here it forms a gap, or fracture, where only gas is present, cutting the sand

bed into two separate parts. Below the fracture, the bubbles remain largely interconnected and the gas volume fraction does not change. Above the fracture, the bubbles are sludge-displacing and do not form a percolation network (till much later); the wet sand is held together by its agglomerate tensile strength.

The percolation threshold is expected to be lower for dendritic bubbles than for sludge-displacing bubbles. A sludge-displacing bubble needs to make contact with its fellows over the full volume of a sludge-filled "unit cell." A dendritic bubble needs to make contact over only the pore volume of the cell, which is ϕ times the unit cell volume. This difference accounts for the earlier percolation in dendritic regions. In accord with this theory, no fractures have been seen in wet clay beds, whose very small pore sizes tend to promote sludge-displacing bubbles–as is expected from Equation E.10–and consequently to possess higher percolation thresholds.

The model takes two different approaches to percolation regions, depending on whether or not they are at the top of the sludge bed. Percolation regions at the top of the bed release the gas fraction in excess of the percolation threshold into the supernatant, and consequently maintain their gas fraction at the percolation threshold value. Regions further down are flagged as percolation regions, and their gas generation rates are set to be consistent with a gas fraction that equals the percolation threshold. However, the model makes no attempt to move the excess gas up into a "fracture." For simplicity, the accumulated gas is modeled as remaining in the depth increments where it is generated.

A model improvement (which would be difficult to implement) would be to explicitly include the gap in the model. Another would be to release only a portion of the excess gas from a percolating region, rather than all of the excess.

Rollover criterion

The sludge rollover in a tank is the result of a buildup of buoyancy-inducing gas in the sludge. The model considers that rollover occurs when the integrated net weight of a sludge column -- the weight relative to the supernatant -- becomes zero.

$$\int_0^{x_R} (\rho_b - \rho_l)\, g\, dx = 0 \qquad \text{(E.17)}$$

In Equation E.17, x_R represents the depth at which the integrated net weight becomes zero; as long as x_R is greater than L (the depth of sludge), rollover does not occur.

Bear in mind that the local sludge density ρ_b is different depending on whether the bubbles in it are sludge-displacing or dendritic (liquid-displacing). For sludge-displacing bubbles,

$$\rho_b = ((1 - \phi)\rho_s + \phi\rho_l)(1 - \alpha) \qquad \text{(E.18)}$$

For dendritic bubbles, the local sludge density is

$$\rho_b = (1 - \phi)\rho_s + (\phi - \alpha)\rho_l \qquad \text{(E.19)}$$

This approach treats the sludge as essentially solid, capable of resisting some lifting force without flowing (so flow begins only when a yield stress is reached). A fluid would begin to flow as soon as $(\rho_b - \rho_l)$ was less than zero anywhere–that is, when the point, rather than the integrated, net weight was zero anywhere in the tank.

There is some question whether the sludge strength could make a macroscopic contribution to delaying rollover, and have a microscopic effect by controlling the bubble shape. The criterion in Equation E.17 applies only if net buoyancy need not work against the strength of the sludge above it. If the sludge strength is significant for a given tank geometry, then for rollover to occur the integral in Equation E.17 has to equal not 0 but -G, where G is the upward pressure the sludge slab can withstand. This approach pictures rollover as a giving-way of sludge near the center of the tank, where the "bending" of sludge by upward force is greatest–not as an overall "flipping" of the sludge plate around some axis of rotation.

Consider the slab of sludge above the rollover level x_R as a structural element, a kind of beam over which a buoyancy force is uniformly distributed. The length l of this "beam" ranges from D, the tank diameter, to zero at the "sides" of the tank. (In short, this approach looks at "strips" of the circular slab as individual "beams.")

Each of the beams has a rectangular cross-section with an area wx_R, where w is an arbitrary beam width. The force per unit length, at the time when the beam gives way, is Gw. Further, consider the beam as having a fractional strain at tensile failure of ϵ_T and a tensile strength of T. According to any standard text on beam deflection, the maximum deflection δ for a beam of length l freely supported at its ends and carrying a uniformly distributed load is

$$\delta = (5\ (Gw)\ l^4)\ /\ (384\ EI)$$

where E = the elasticity; for an elastic solid this is tensile strength over fractional strain, or T/ϵ_T (also note that at failure $\delta = \epsilon_T x_R$)

I = the moment of inertia of the beam; in this orientation, $w(x_R)^3/12$

The deflection equation can be solved for G:

$$G = 6.4T\ (x_R/l)^4 \qquad \text{(E.20)}$$

Take a value for x_R of 5 m, slightly less than the sludge depth, and a tank diameter of 23 m as a maximum value of the beam length l. The tensile strength of the sludge is unknown, but the highest value measured for shear strength of the sludge in Tank 241-SY-101 is about 12,000 Pa.[a] Putting all this together, very approximately, G is found to be 170 Pa (not including crust strength.) To put this in perspective, the calculated G value corresponds to only about 0.1 m (or 3 in.) of sludge at a buoyant sludge density 10% less than the supernatant density of 1.45 g/cc. Very little instability is required to break the "sludge slab." There seems little need to include the "structural strength" of the sludge in the model, at least for the waste tank geometry in which l can be so much greater than x_R.

(a) Tingey, J. M. 1992. *"Physical Characterization of Tank 101-SY Core Samples from Window C."* Letter report prepared for Westinghouse Hanford Company by Pacific Northwest Laboratory, Richland, Washington.

Gas release

When the model finds that the rollover criterion in Equation E.17 has been met somewhere in the tank, it does several things. First, it releases all the gas exceeding a volume fraction of α_0 (at pressure P_0) that is contained in the sludge above the rollover level x_R. Second, it discharges all the gas exceeding the percolation threshold contained in sludge that is in a percolation region whose top boundary is at x_R, if any such region exists. Those two releases together make up the calculated gas release. Third, it resettles the sludge that rolled over, initializing its post-rollover bubble size distribution in the manner already described. The sludge beneath the rollover level is not initialized, except that the gas volume fraction in discharged percolation regions is set to the percolation threshold.

The gas released from the sludge involved in a rollover is calculated as

$$dQ = A\ dx \left(\alpha \frac{P}{P_0} - \alpha_0 \right) \tag{E.21}$$

where dQ = the incremental gas release from an increment of sludge depth
A = the cross-sectional area (plan view) of the tank
dx = the depth increment
α = the local void fraction
P = the local pressure
P_0 = the ambient pressure at the top of the supernatant
α_0 = the retained void fraction at P_0

The gas "drained" from the sludge in a percolating layer below the rollover, if such a layer exists, is calculated in a way that accounts for the percolation paths remaining open after the excess gas is drained:

$$dQ\ \ A\ dx \left\{ (\alpha - \alpha_p) \frac{P}{P_0} - \alpha_0 \right\} \tag{E.22}$$

where α_p = the percolation threshold void fraction.

The model does not at present calculate the amount of gas released during non-rollover conditions (the gas released at each "time step" from percolation regions [if any] at the top of the sludge). Calculating and printing out these releases would not be difficult.

Sludge strength model

The model for the sludge yield strength allows for the dependence of the strength on both depth in the sludge and the length of "time" since a rollover last disturbed the sludge at that depth. The presence of these dependences has been suggested by experimental observations (Tingey et al. 1994).

The yield strength S that the model uses is a composite quantity that represents either $\tau_s \epsilon_s^{1/2}$ or $\tau_s / \epsilon_s^{1/4}$, depending on whether Equation E.10 or E.11 is used to calculate the Bond number. As a first approximation, the property S is taken to depend on depth x in a continuous step-like function whose slope and smoothness can be set by input of three parameters S_0, S_{max}, and x_{max}:

$$S = \frac{S_{max} + S_0}{2} + \frac{S_{max} - S_0}{2 \tan^{-1}(C x_{max}/2)} \tan^{-1}(C (x - x_{max}/2)) \qquad \text{(E.23)}$$

where S_0 = the strength at $x = 0$
S_{max} = the strength at $x = x_{max}$
x_{max} = a depth used to "position" the strength function (x_{max} does not have to equal L, the sludge depth)

The time dependence of S is included in the parameters S_0 and S_{max}; these are treated as functions of "time" in complementary exponential form:

$$\tau_0 = s_{0,0} + s_0 (1 - \exp(-t/\theta_0)) \qquad \text{(E.24)}$$

$$\tau_{max} = s_{max,0} + s_{max} (1 - \exp(-t/\theta_{max})) \qquad \text{(E.25)}$$

In Equations E.24 and E.25 the time elapsed since last disturbance, t, and the time constants θ_0 and θ_{max} are not in actual time units but are in the model's "time" units related to gas generation increments.

Model inputs

Three different sets of model inputs have been studied. The first input set describes Tank 241-SY-101; it includes a "best-estimate" case, some sensitivity tests to illustrate the effect of very small changes in variables, and scenarios with decreased temperature and supernatant depth. The second set of inputs contains a more extensive set of 241-SY-101 sensitivity tests, showing the effects of large changes in variables. The third set of inputs describes an experimental wet sand column (with gas generation) that was used by Gauglitz et al. (1994).

The BOND6 inputs for a best-estimate description of 241-SY-101, before mitigation are in Table E.1. These inputs are used as the base case for a variety of sensitivity tests.

The sludge-displacing bubbles were taken as having the percolation threshold for a general random mixture (Nan and Smith 1991). The value for dendritic bubbles is ϕ times that for the sludge-displacing bubbles.

The peak/minimum gas generation ratio of 4.0 was derived from Figures 2.9 and 3.1 of Allemann et al. (1991). The minimum and peak measured temperatures in the nonconvective layer were about 125°F (52°C) and 145°F (63°C). From Figure 3.1 (Allemann et al. 1991) and its associated correlation, the ratio of the thermal gas-volume production rates at these temperatures is about 4. (Unfortunately,

Table E.1. Best-Estimate BOND6 Input Parameters for Tank 241-SY-101 Before Mitigation

Surface area of tank	410 m^2 (for a diameter of 23 m)
Depth of supernatant Δ	4.57 m
Supernatant density ρ_l	1503 kg/m^3 [(a)] interpolated to the average temperature, 57°C and averaged over Segments 15, 19, and 22 from the nonconvective layer
Surface tension σ	0.065 N/m (Norton and Pederson [1994] for slurry simulant SY1-SIM-91A +at 50°C with 1% NH_3)
Gas-free sludge depth L	5.26 m gasless (gives 387 in. of waste height when gas-free)
Solids density ρ_s	2100 kg/m^3 (for $Nato_3$, $Nato_2$ with some liquid inclusions to lower the density)
Pore volume ϕ	0.686 (for a gas-free sludge density of 1690 kg/m^3 interpolated to 57°C and averaged)[(a)]
Pore diameter D_p	3 x 10^{-6} m (consistent with Gauglitz et al. [1994])
Percolation threshold	0.15 for sludge-displacing bubbles 0.10 for dendritic bubbles
Post-rollover α_0	0.122 volume fraction gas (at 1 atm); this is consistent with a minimum post-rollover waste height of 400 in.)
Initial bubble diameter D_0	100 x 10^{-6} m (at 1 atm); this gives an average bubble size in situ of 80-100 μm at rollover, consistent with recent analyses
Gas generation variation	peak/minimum ratio = 4.0 (explained below)
Sludge strength model	
S_0	65 Pa, constant with time (= $\tau_s \epsilon_s^{1/2}$)
S_{max}	200 Pa, constant with time (= $\tau_s \epsilon_s^{1/2}$)
C	17 (for a sharp increase in strength with depth)
x_{max}	7 m

we do not have data on the temperature dependence of the radiolytic gas production.) Using the parabolic dependence of gas generation on depth that is assumed in the computer model, the average gas generation rate in the layer is

= (2 * maximum rate + minimum rate)/3
= 3 vol%/month

(a) Tingey, J. M. 1992. *Physical Characterization of Tank 101-SY Core Samples from Window C.* Letter report prepared for Westinghouse Hanford Company by Pacific Northwest Laboratory, Richland, Washington, Tables 3.3 and 3.4.

The inputs for the sludge strength model were roughly based on the shear strength measurements for the nonconvective sludge layer in Window C.[a] The measurements at 50 and 65°C were used to make a very rough interpolation to the average temperature of 57°C. This procedure gave a shear strength τ_s of 600 Pa at the top and middle of the layer and a value of 2000 Pa at the bottom. The shear strength in the middle of the sludge layer (Segment 19) has been measured as less than or equal to the value at the top (S_0); therefore C and x_{max} were adjusted to match this behavior while still leveling out at the maximum strength value at the tank bottom. The fractional strain at failure ϵ_s is not known for the sludge, but is expected to be about 0.01. (For comparison, the fractional failure strain for wet limestone agglomerate is about 0.002, as stated in Schubert et al. [1983].)

BOND6 was also used to examine the behavior of the wet sand column (with gas generation) that was used by Gauglitz et al. (1994) in experiments. For this system, the model inputs are in Table E.2.

Table E.2. BOND6 Input Parameters for a Bench-Scale Wet Sand Column

Surface area of column A	0.002 m^2
Depth of supernatant Δ	0.075 m
Supernatant density ρ_l	1000 kg/m^3 (water)
Surface tension σ	0.072 N/m (water)
Gas-free sludge depth L	0.50 m
Solids density ρ_s	2600 kg/m^3 (quartz)
Pore volume ϕ	0.32 (equal-size spherical particle packing)
Pore diameter D_p	$30x10^{-6}$ m (consistent with Gauglitz et al. [1994])
Percolation threshold	0.15 for sludge-displacing bubbles 0.05 for dendritic bubbles
Post-rollover α_0	0.01 volume fraction gas (at 1 atm)
Initial bubble diameter D_0	50×10^{-6} m (at 1 atm)
Treat gas generation as constant with depth	
Sludge strength model	
S_0	0 Pa
S_{max}	0 Pa

Model predictions–best-estimate for Tank 241-SY-101

The BOND6 predictions for the 241-SY-101 best-estimate case are compared to the 241-SY-101 observations in Table E.3. It appears that the model matches the rollover behavior up through August-December 1991, if each time step is taken equal to about eight days, but that some new regime of tank behavior begins after that. In the data, the December 1991 rollover is associated with an unprecedented decrease of temperature all through the nonconvecting layer. In this new regime (whose emergence this model does not predict), the average amount of gas generated per "timestep" would be smaller as a result of the lower temperature. Possibly some of the waste properties had changed in such a way as to cause different rollover behavior.

(a) Tingey, J. M. 1992. *Physical Characterization of Tank 101-SY Core Samples from Window C.* Letter report prepared for Westinghouse Hanford Company by Pacific Northwest Laboratory, Richland, Washington, Tables 3.3 and 3.4.

Table E.3. Comparison of BOND6 Predictions with 241-SY-101 GRE Behavior Before Mitigation

Model Output		241-SY-101 Measured GREs (Babad et al. 1992, WHC-SD-PE-050 Table 6-1)		
Time Steps Since Last Rollover	Gas Release (m^3)	Days Since Last Rollover (date of GRE)		Gas Release (m^3)
10	222	109	(1/90)	---
14	275	110	(4/19/90)	174 - 253
14	129	109	(8/5/90)	96 - 133
11	214	80	(10/24/90)	187 - 272
14	129	110	(2/13/91)	93 - 128
9	275	82	(5/16/91)	114 - 204
14	129	102	(8/27/91)	85 - 142
11	214	99	(12/4/91)	271
14	129	138	(4/20/92)	130
10	222	136	(9/3/92)	297
14	275	152	(2/2/93)	184
14	129	144	(6/26/93)	198

A best-estimate model for 241-SY-101 after 12/4/91 contains many of the same parameter values as the prior period (Table E.1). However, several parameters are adjusted to reflect the lower temperature range–120 to 130°F, rather than 125 to 145°F. The changed parameters are shown in Table E.4.

Table E.4 Temperature-Corrected BOND6 Input Parameters for Tank 241-SY-101

Supernatant density ρ_l	1513 kg/m^3 (Tingey 1992, Tables 3.3 and 3.4, at the average temperature, 52°C and averaged)
Surface tension σ	0.066 N/m (Norton and Pederson 1994)
Pore volume ϕ	0.698 (for a gas-free sludge density of 1690 kg/m^3 at 52°C and averaged)
Gas generation variation	peak/minimum ratio = 2.0 (explained below)
S_0	70 Pa, constant with time ($= \tau_s \epsilon_s^{1/2}$)
S_{max}	265 Pa, constant with time ($= \tau_s \epsilon_s^{1/2}$)

It should also be noted that the average gas generation rate in the lowered temperature range is 40% of that for the pre-December-91 scenario.

Table E.5 gives the predicted behavior of the 241-SY-101 waste in the lower-temperature regime that prevailed after December 1991.

In the case shown in Table E.5, the model does not work especially well. It strongly over predicts the increase in the time between GREs, which presumably resulted from the decrease in temperature and gas generation rate. The pattern of release sizes also does not match, in particular the prediction of characteristically smaller releases.

Table E.5. Comparison of BOND6 Predictions with 241-SY-101 GRE Behavior After 12/91, Ignoring the Effects of Mitigation

Model Output		241-SY-101 Measured GREs (Babad et al. 1992, WHC-SD-PE-050 Table 6-1)	
Time Steps Since Last Rollover	Gas Release (m^3)	Days Since Last Rollover (date of GRE)	Gas Release (m^3)
18	246	99 (12/4/91)	271
29	67	138 (4/20/92)	130
18	165	136 (9/3/92)	297
28	223	152 (2/2/93)	184
29	67	144 (6/26/93)	198

The sensitivity of the model, and possibly of the tank wastes, to small changes in parameters can be seen in Table E.6. Here the behaviors of three versions of the pre-December-91 241-SY-101 tank wastes are compared. Each GRE sequence in Table E.6 contains one cycle of GREs; hypothetically, barring the type of unpredicted regime change that occurred in December 1991, they could repeat indefinitely.

As can be seen from the difference between the base case and the 50°C case, small changes in density parameters strongly affect the magnitudes of releases but (at least in this pair of cases) do not change the pattern of the sequence. The decrease in the difference between sludge and liquid densities accounts for the smaller release sizes in the 50°C case. Nevertheless, both cases have the same sequence of release sizes: medium, large, small, medium, small, large, small, medium, small.

However, an increase in the ratio of the maximum to the minimum gas generation rate drastically changes the sequence without greatly changing the spacing or release sizes. The pattern for the ratio-5 case is much more complex than that for the base case. (Comparison with Table E.2 suggests that the ratio-5 case fits the observations better than the base case, in terms of release magnitudes, relative lengths of time intervals, and pattern.)

The base-case model can be adapted in an attempt to predict the behavior of the 241-SY-101 wastes after drastic changes in system parameters. Table E.7 contains two examples. The first prediction is for the case where the overall tank temperature drops by about 20°F; the second, a case where enough supernatant is removed to reduce the waste height to 240 inches.

As can be seen, the decreased temperature leads to a larger difference between liquid and sludge densities and so to larger releases. The cause of the simplified release pattern is not so obvious. The "small, medium, large" pattern that is seen would be expected for gas generation with low peaking. First a top layer reaches the highest stable void fraction, peels off, and resettles as a low-void lid on the more gassy strata beneath. Then the top part of those layers reaches its stable limit and everything above it rolls, leaving only a bottom layer where the gas buildup continues. Finally this bottom layer becomes unstable and all of the waste rolls over, producing the third and largest gas release. The larger is the sludge-liquid density difference and the smaller the gas generation peaking ratio, the closer the rollover behavior comes to a simple "three-step."

Table E.6. Small-Variation Sensitivity Tests for the 241-SY-101 Pre-12/91 Scenario

Base Case, Pre-12/91		Pre-12/91 with All Parameters at 50°C		Pre-12/91 Base Case with Gas Ratio = 5	
ρ_l: 1503 kg/m^3		ρ_l: 1550		ρ_l: 1503	
σ: 0.065 N/m		σ: 0.066		σ: 0.065	
ϕ: 0.686		ϕ: 0.690		ϕ: 0.686	
Gas gen. ratio: 4.0		Gas gen. ratio: 4.0		Gas gen. ratio: 5.0	
Average gas rate: 3%/month		Average gas rate: 0.8%		Average gas rate: 3%	
S_0: 65 Pa		S_0: 70		S_0: 65	
S_{max}: 200 Pa		S_{max}: 265		S_{max}: 200	
Time Steps Since Last Rollover	Release (m^3)	Time Steps Since Last Rollover	Release (m^3)	Time Steps Since Last Rollover	Release (m^3)
10	222	22	115	11	204
14	275	31	187	14	242
14	129	32	63	14	135
11	214	22	124	11	281
14	129	32	63	14	130
9	275	18	60	14	135
11	214	21	176	10	256
14	129	32	63	14	135
				11	210
				14	252
				14	135
				11	268
				14	135

The effect of another important parameter can be seen in the shallow-supernatant case. Here, a very complicated release pattern results from decreasing the hydrostatic pressure at the top of the sludge layer. Remember that the retained void fraction α_0, the volume fraction gas that the sludge keeps even after a rollover, was set at 0.122 at the top of the supernatant. Because the supernatant in this case is so shallow, the void fraction at the top of the sludge layer is only a little less than 0.122; in fact, it is 0.104. The void fraction at which sludge and liquid density are equal is 0.105. The small difference between the initial (retained) void fraction and the nominal rollover void fraction leads to a large number of small rollovers in which thin top layers peel off interspersed with a few rollovers in which large fractions of the tank waste participate. In fact, the rollover pattern predicted for the shallow case has been simplified for Table E.6: the many rollovers in which less than 1 m^3 offgas is released have been omitted on the grounds that they might not be detected by tank instruments. Note that the near equality of the retained and rollover void fractions also leads to smaller maximum releases.

The release pattern is simplified not only by large sludge-liquid density differences and small gas generation peaking but also by large differences between the initial and rollover void fractions. The large differences come from diminished retention or substantial hydrostatic head above the sludge layer.

Table E.7. Predicted 241-SY-101 Behavior for Cooler Temperature and Shallower Supernatant Layer

Base Post-12/91		Post-12/91 with Temperature 98-107°F		Post-12/91 with Removed Supernatant	
Δ: 4.57 m liquid		Δ: 4.57 m		Δ: 0.84 m	
ρ_l: 1513 kg/m^3		ρ_l: 1494		ρ_l: 1513	
σ: 0.066 N/m		σ: 0.073		σ: 0.066	
ϕ: 0.698		ϕ: 0.672		ϕ: 0.698	
Gas gen. ratio: 2.0		Gas gen. ratio: 2.0		Gas gen. ratio: 2.0	
Avg. gas rate: 1.2%/month		Avg. gas rate: 0.22%		Avg. gas rate: 1.2%	
S_0: 70 Pa		S_0: 300		S_0: 70	
S_{max}: 265 Pa		S_{max}: 750		S_{max}: 265	
Time Steps Since Last Rollover	Release (m^3)	Time Steps Since Last Rollover	Release (m^3)	Time Steps Since Last Rollover	Release (m^3)
18	246	213	99	5.3	2.2
29	67	133	229	2.6	6.9
18	165	214	289	4.1	20.7
28	223	214	104	5.3	2.1
29	67	138	229	1.4	47.0
18	165	203	303	5.3	2.2
26	241			2.7	7.2
29	67			3.3	78.6
18	165			5.3	2.2
28	223			2.7	7.2
29	67			4.1	21.1
18	244			5.3	2.1
29	71			1.2	105.6
18	166				
29	217				
29	71				

At present, the data are not sufficient to predict rollover behavior for tanks other than 241-SY-101. Temperature profiles have been obtained in many cases, as well as estimates of sludge and liquid depths, but the crucial density data are lacking.

Model predictions–large variation in parameters

Figure E.1 shows the effect on the gas release pattern of large variations in some of the model parameters–namely, yield strength, gas generation peaking ratio, and percolation threshold. In Figure E.1(A), the base case yield strength given in Table E.1 was multiplied by a factor of 20 and reduced to 0. The reduction in the yield strength caused an imperceptible change in gas release behavior;

apparently the expected yield strength of the 241-SY-101 sludge is already too low, according to BOND6, to affect rollover behavior. Multiplying the yield strength by 20 increases the maximum release, decreases the minimum release, and creates a slightly more irregular cycle pattern.

Rearranging the spatial distribution of the gas generation also had interesting effects, as shown in Figure E.1(B). Here the inputs were adjusted to give all three cases the same depth-averaged gas generation rate as the base case, but there were different distributions of gas generation with depth. The two sensitivity cases were 1) 10 times as much gas generation in the center of the sludge as at the top and bottom (a parabolic convex profile), and 2) the same gas generation in the center (a flat profile). The increase in gas generation peaking causes a release pattern that appears chaotic (at least over the time interval shown here); the maximum and minimum releases, and the times between releases, are about the same as for the base case. The flat gas generation profile leads to a regular pattern of releases with shorter periods and much smaller minimum releases than the base case.

Figure E.1(C) portrays the effects of different values of percolation thresholds. Increasing the percolation thresholds (spherical and dendritic) by one-third changes the release pattern slightly and has little effect on the magnitude of the maximum and minimum. The period of the release cycle appears slightly greater for the higher percolation threshold. Decreasing the percolation threshold has a more noticeable effect, producing much lower minimum releases and shorter cycle periods than for the base case.

Figures E.2, E.3, and E.4 show the void fraction and bubble type distributions for the case in which the waste is like that in Tank 241-SY-101, except that it has 20 times the expected yield strength [this sensitivity case is also shown in Figure E.1(A)]. This value of yield strength, or $(\tau_s \epsilon_s)^{1/2}$, is at the upper end of the uncertainty range for 241-SY-101 yield strength. The figures show the complicated patterns of bubble shape that can arise in sludge with high yield strength.

Figure E.2 depicts the bubble distributions that exist just after a rollover that involves the entire sludge bed, and shows how the bubble distribution evolves over the time before the next rollover. The region of spherical bubbles gradually expands downward as the higher void fraction causes a decrease in the weight carried by bubbles in the lower layers. In Figure E.3, which starts just after the rollover at the end of Figure E.2, the undisturbed lower layer has accumulated enough gas to form a dendritic percolation zone. Fractures would be expected to form at the upper edge of the percolation zone, where the escape of gas is blocked by the non-percolating spherical bubble region. After another rollover, the situation shown in Figure E.4 arises. The dendritic percolation layer is trapped between two layers of dendritic bubbles, with spherical bubbles in the upper region.

Model predictions–sand column

Figure E.5 shows the model's predictions for the bench-scale wet sand column (with gas generation), modeled with Table E.2 inputs. Bubbles that are initially contained within the pores and effectively dendritic, because the bubble diameters are less than the pore diameter, grow to establish two distinct regions of sludge-displacing and dendritic bubbles. The dendritic bubbles soon form a percolation region, at whose top a "fracture" would be expected to form. This fracture would be about two-fifths of the way up the column. As time passes some of the dendritic area below the fracture changes to sludge-displacing bubbles, which might tend to cap off the dendritic percolating region below. Finally (at more than three times as long as required for the fracture to form) the entire column becomes a

percolating region. The bed height has increased by about 11%. At this time the top part of the bed would presumably collapse into the fracture because there would be no trapped air pressure to hold it up. Because the percolation threshold is substantially smaller than the concentration at which buoyancy makes the bed unstable, rollover does not occur.

Figure 4.1 in Gauglitz et al. (1994) allows some comparison between predictions and observations. The depth of the supernatant layer increases, although its increase stops after about one hour and 15 minutes; this suggests that a region of dendritic bubbles has formed and stopped growing. At about the same time, a fracture region begins to appear about three-fourths of the way up the column. At two hours, the sand bed has partly collapsed and the bed height has increased by about 14%. The observed supernatant layer about doubles in depth, compared with a predicted increase of about 20%. These observations are roughly in accord with predictions. Note that the inputs prescribed a yield strength of zero for the bed; however, if a small yield strength S of 50 Pa had been used instead, the predicted fracture height would match the observed, and the larger dendritic region would cause a greater increase in supernatant depth.

Possible model improvements

The model as it stands can predict gross rollover behavior, or at least match it conceptually. The correspondence between rollover predictions and observations suggests that the bubble size and shape distributions predicted by the model also have some validity. Some possible improvements to the model have already been mentioned and will be repeated here.

- A less approximate form for the effect of the presence of multiple bubbles on the sludge yield (on the microscopic scale) would improve the Bond number calculations. It could probably be found using a free-cell derivation of 3-D stress and strain variation around a population of spherical holes containing pressure.

- More physical properties could be treated as variable with depth, and the variation could be fitted to data using some form of numerical interpolation rather than analytical functions.

- An explicitly defined time step would be more convenient and comprehensible than the "time step," defined implicitly by gas generation, that has been used to date.

- When a fracture comes into being because of a capped percolation region, the model should show it explicitly as a gas gap in the bed. A related model improvement would be to release only a portion of the excess gas from a percolating region, rather than all of the excess. The whole breadth of a percolating depth increment does not necessarily participate in a gas discharge.

- Include the effect of the "structural strength" of the sludge slab over a buoyant layer in delaying rollover. In tanks that have a sludge crust, such as 241-SY-101, the strength of the crust should also be included.

- Calculate and output the release rate for gas discharging from uncapped percolation regions, if they exist.

References

Allemann, R. T., Z. I. Antoniak, J. R. Friley, C. E. Haines, L. M. Liljegren, and S. Somasundaram. 1991. *Collection and Analysis of Existing Data for Waste Tank Mechanistic Analysis. Progress Report -- December 1990.* PNL-7658, Pacific Northwest Laboratory, Richland, Washington.

Babad, H., G. D. Johnson, D. A. Reynolds, and D. M. Strachan. 1992. *Understanding of Cyclic Venting Phenomena in Hanford Site High-Level Waste Tanks: The Evaluation of Tank 241-SY-101.* WHC-SA-1364-FP, Westinghouse Hanford Company, Richland, Washington.

Gauglitz, P. A., L. A. Mahoney, D. P. Mendoza, and M. C. Miller. 1994. *Mechanisms of Gas Bubble Retention.* PNL-10120, Pacific Northwest Laboratory, Richland, Washington.

Nan, C.-W., and D. M. Smith. 1991. "A.C. Electrical Properties of Composite Solid Electrolytes." *Materials Science and Engineering* , Vol. B10, pp. 99-106.

Norton, J. D., and L. R. Pederson. 1994. *Ammonia in Simulated Hanford Double-Shell Tank Wastes: Solubility and Effects on Surface Tension.* PNL-10173, Pacific Northwest Laboratory, Richland, Washington.

Schubert, H., W. Herrmann, and H. Rumpf. 1975. "Deformation Behavior of Agglomerates under Tensile Stress." *Powder Technology*, Vol. 11, pp. 121-131.

Tingey, J. M., P. R. Bredt, and E. H. Shade. 1994. *The Effects of Heating and Dilution on the Rheological and Physical Properties of Tank 241-SY-101 Waste.* PNL-10198, Pacific Northwest Laboratory, Richland, Washington.

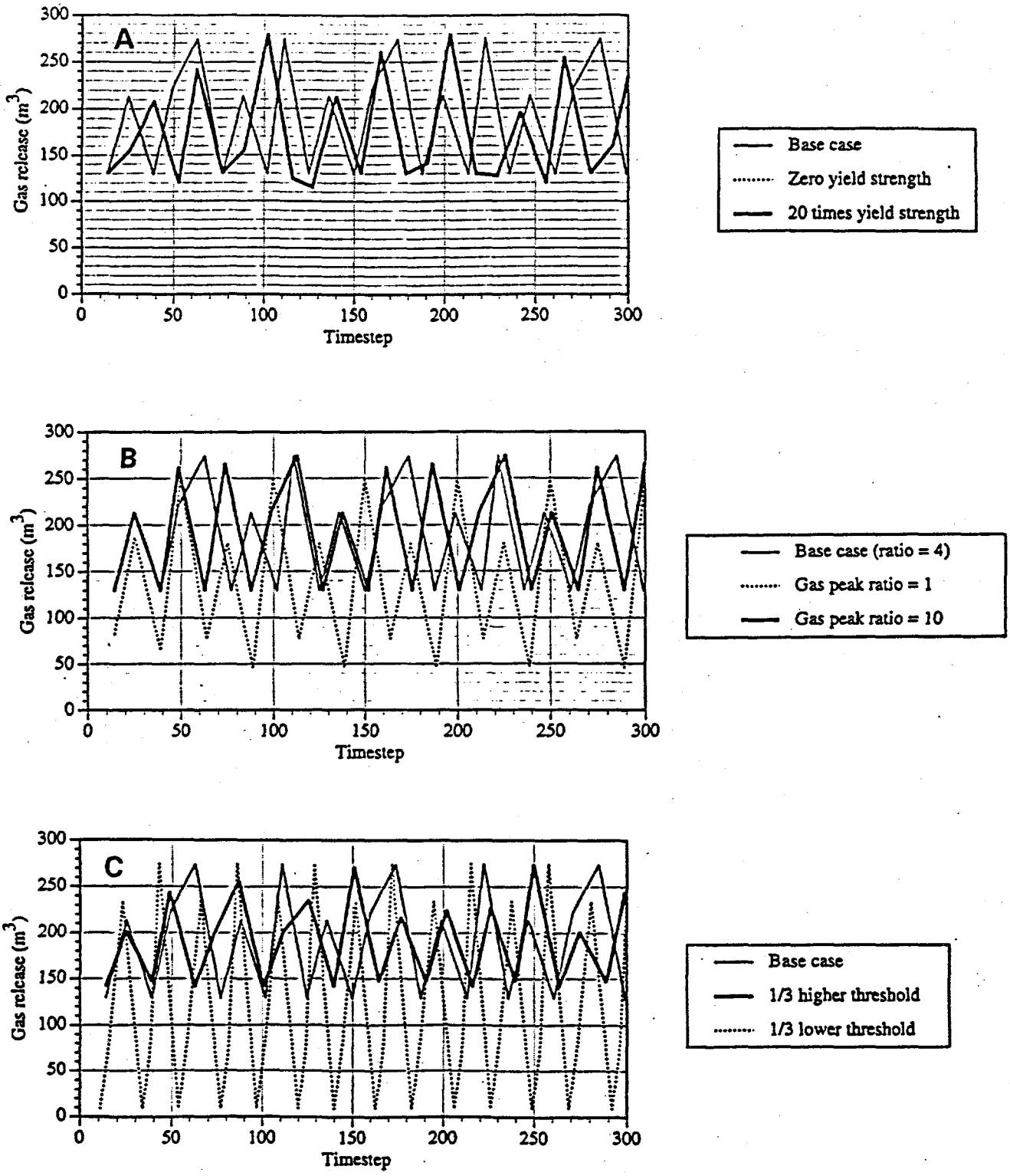

Figure E.1. Effects of (A) Yield Strength, (B) Gas Generation Distribution, and (C) Percolation Threshold on the Gas Release for Tank SY-101

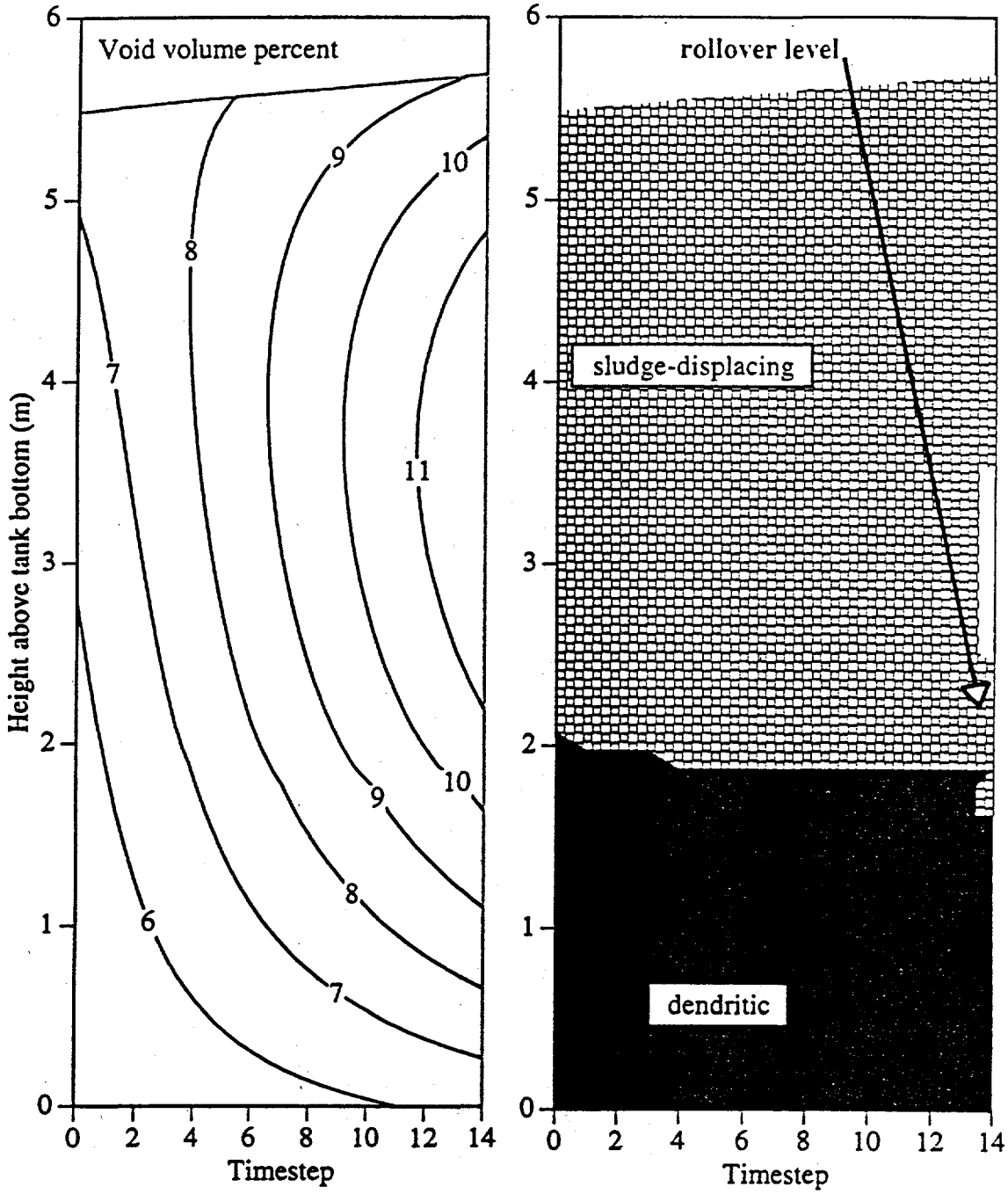

Figure E.2. The Void Percent and Bubble Shapes for the First Rollover in the Cycle for Tank 241-SY-101 (with 20 times the expected yield strength)

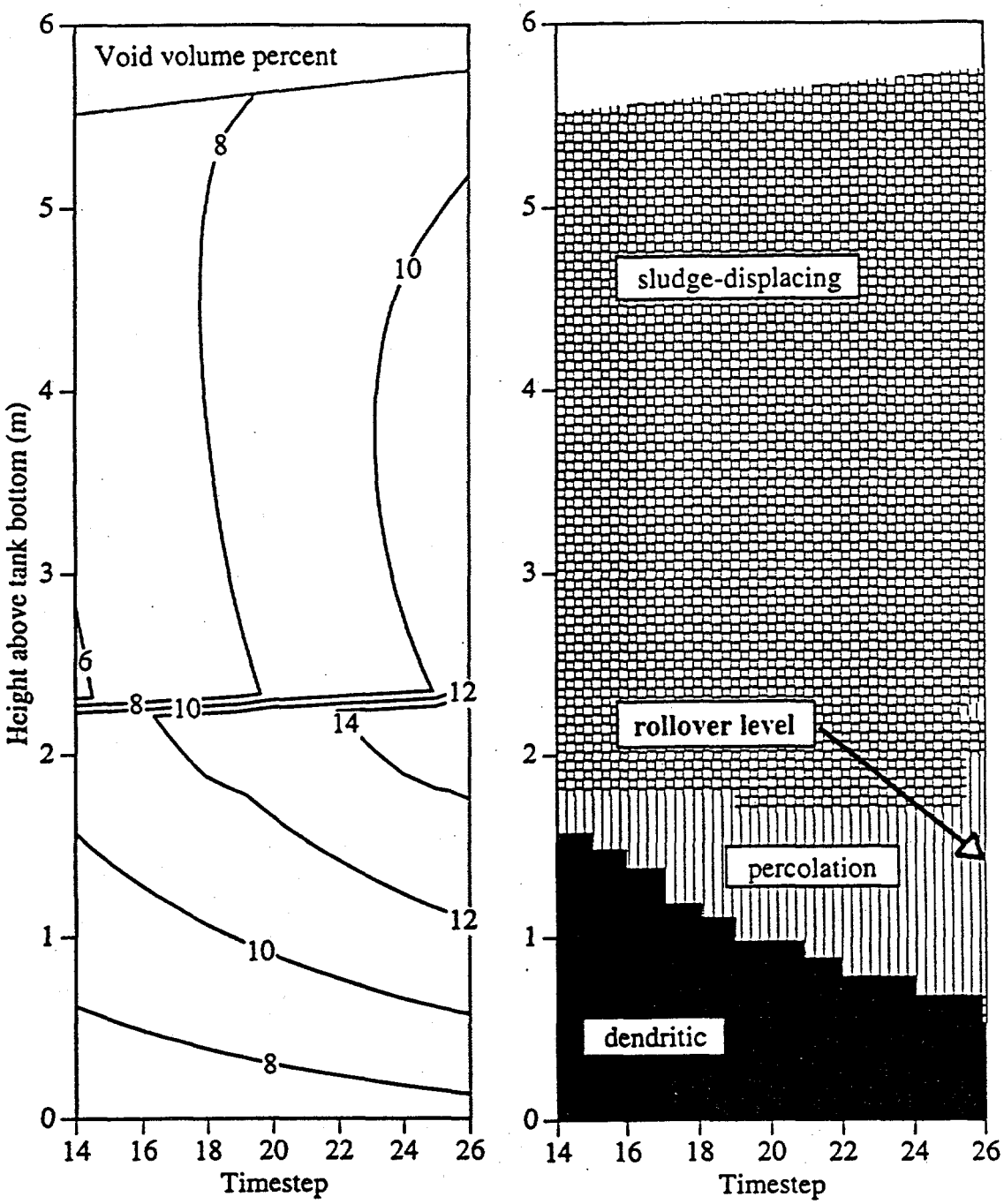

Figure E.3. The Void Percent and Bubble Shapes for the Second Rollover in the Cycle for Tank 241-SY-101 (with 20 times the expected yield strength)

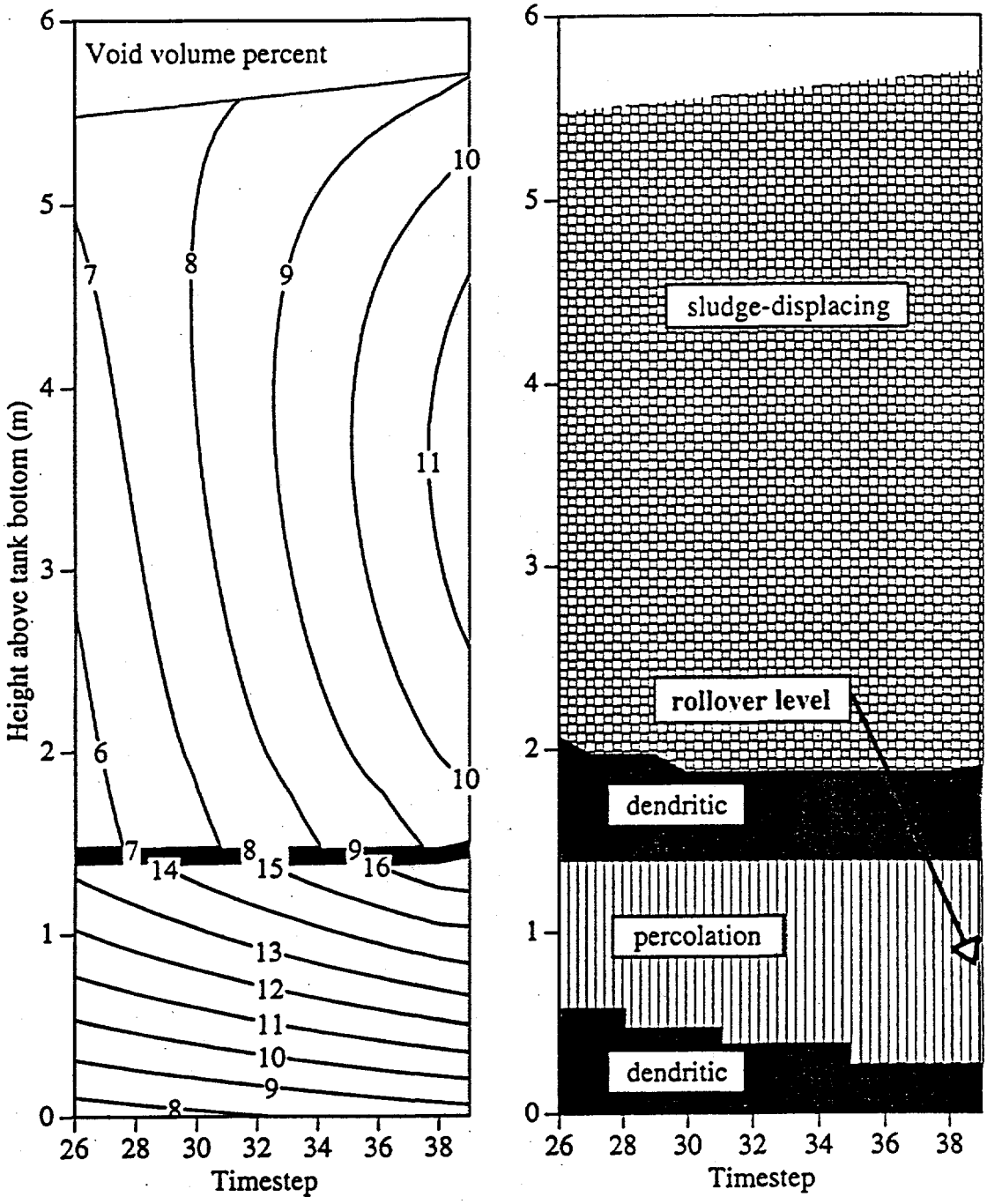

Figure E.4. The Void Percent and Bubble Shapes for the Third Rollover in the Cycle for Tank 241-SY-101 (with 20 times the expected yield strength)

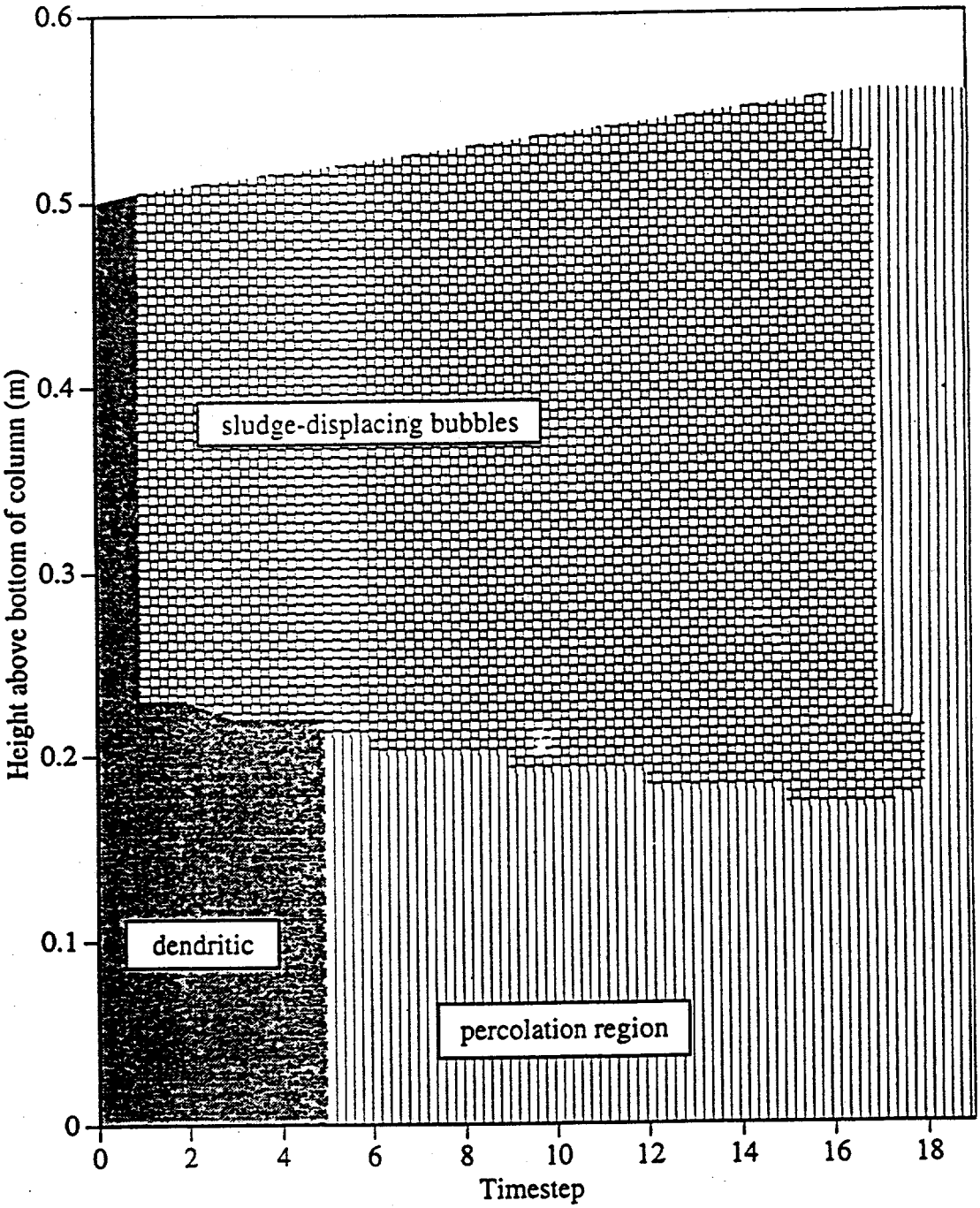

Figure E.5. Progress in Time of the Bubble-Type Regions in a Sand Column

Appendix F

A Two-Dimensional Model of Stress in a Bubbly Sludge

Appendix F

A Two-Dimensional Model of Stress in a Bubbly Sludge

A theoretical model can be derived for the stresses that result when a unidirectional tensile stress is applied to a thin (2-D) plate containing a large number of evenly spaced circular holes. The model includes a "pressure" at the edges of the hole. This approach provides some insight as an analogy to the behavior under stress of the "Swiss cheese" sludge in the 3-D case.

The model depends on treating an annular region around each hole as a "free cell." At the border of the circular region, the overall boundary conditions (unidirectional tension or compression) are applied as derived in pp. 76-81 of Dally and Riley (1978):

$$\begin{aligned} \sigma_{rr} &= (\sigma_0/2)(1 - \cos(2\theta)) \\ \sigma_{\theta\theta} &= (\sigma_0/2)(1 + \cos(2\theta)) \end{aligned} \tag{F.1}$$

where all the variables are defined under Equation F.5. The size of the annulus is chosen to make the solid fraction (annulus area/total area) the same as the solid fraction of the "Swiss cheese" as a whole. At the edge of the hole, the "pressure" A in the hole is used as a boundary condition:

$$\begin{aligned} \sigma_{rr} &= A \\ \tau_{r\theta} &= 0 \end{aligned} \tag{F.2}$$

Although the assumptions inherent in the free cell treatment are only approximately accurate for the 3-D sludge bed containing sludge-displacing, roughly spherical bubbles, the end result of the derivation should indicate some of the structure of a true solution (especially for low void-fraction). The derivation is carried out by solving for the coefficients of the Airy's stress functions (the known general solutions of the 2-D stress-strain equation); an example of such a solution (for a single hole containing no pressure) has already been referred to.

The result is the following set of equations for the tensile (or compressive) and shear stresses at any point in the 2-D free-cell slice of "Swiss cheese":

$$\frac{\sigma_{rr}}{\sigma_0} = \frac{\left[\frac{A}{\sigma_0}\left(1 - \ln(\epsilon_b R^2) - 1/\epsilon_b R^2\right) - \frac{1}{2}\left(1/\epsilon_b - 1/\epsilon_b R^2 - \ln(R^2)\right)\right]}{1 - \ln(\epsilon_b) - 1/\epsilon_b} + \frac{\left(1 + 1/\epsilon_b^2 - 4/\epsilon_b^2 R^2 + 3/\epsilon_b^2 R^4 - 1/R^4\right)}{2\left(1 - 1/\epsilon_b\right)^2\left(\epsilon_b^2 + 2\epsilon_b - 1\right)}\cos(2\theta) \tag{F.3}$$

$$\frac{\sigma_{\theta\theta}}{\sigma_0} = \frac{\left[\frac{A}{\sigma_0}\left(-1 - \ln(\epsilon_b R^2) + 1/\epsilon_b R^2\right) - \frac{1}{2}\left(1/\epsilon_b + 1/\epsilon_b R^2 - \ln(R^2) - 2\right)\right]}{1 - \ln(\epsilon_b) - 1/\epsilon_b} + \frac{\left(-1 - 1/\epsilon_b^2 - 3/\epsilon_b^2 R^4 + 1/R^4 + 4R^4\right)}{2\left(1 - 1/\epsilon_b\right)^2\left(\epsilon_b^2 + 2\epsilon_b - 1\right)}\cos(2\theta) \qquad \text{(F.4)}$$

$$\frac{\tau_{r\theta}}{\sigma_0} = \frac{\left(-1 - 1/\epsilon_b^2 - 2/\epsilon_b^2 R^2 + 3/\epsilon_b^2 R^4 - 1/R^4 + 2R^2\right)}{2\left(1 - 1/\epsilon_b\right)^2\left(\epsilon_b^2 + 2\epsilon_b - 1\right)}\sin(2\theta) \qquad \text{(F.5)}$$

where σ_{rr} = tensile stress in the radial direction

$\sigma_{\theta\theta}$ = tensile stress in the angular direction (everywhere perpendicular to σ_{rr})

σ_0 = the applied unidirectional tensile stress

$\tau_{r\theta}$ = shear stress

A = the pressure at the edge of the hole (outward pressure is positive)

a = the radius of a hole

ϵ_b = the fraction of the plate area taken up by holes (void fraction); it should be less than roughly 0.20 for the above equations to be applicable.

R = normalized radius = r / a, measured from the center of the hole; meaningful values are

$$1 \le R \le 1/\sqrt{\epsilon_b}$$

θ = angle, measured counterclockwise from the positive horizontal radius of the hole

These equations match the original boundary conditions, and reduce (for A=0 and ϵ_β approaching 0) to the reference's derived equations for stress around a single, pressureless hole in a plate subjected to tension. Under the condition of zero applied tensile stress (σ_0=0), Equations (A-3) through (A-5) become

$$\frac{\sigma_{rr}}{A} = \frac{\left[\left(1 - \ln(\epsilon_b R^2)\right) - 1/\epsilon_b R^2\right]}{1 - \ln(\epsilon_b) - 1/\epsilon_b} \qquad \text{(F.6)}$$

$$\frac{\sigma_{\theta\theta}}{A} = \frac{\left[\left(-1 - \ln(\epsilon_b R^2)\right) + 1/\epsilon_b R^2\right]}{1 - \ln(\epsilon_b) - 1/\epsilon_b} \tag{F.7}$$

$$\tau_{r\theta} = 0 \tag{F.8}$$

When the general Equations F.3 through F.5 are solved over the domain of the free cell, the maximum values of the stresses can be found. Figure F.1 is the maximum normalized angular stress, shown as a function of the pressure A and the void fraction. Note that at zero pressure and void fraction this maximum normalized tensile stress is 3, the expected stress concentration factor. Figure F.2 shows the maximum normalized shear stress, a function of void fraction ϵ_β alone.

References

Dally, J. W., and W. F. Riley. 1978. *Experimental Stress Analysis. 2nd Ed.* McGraw-Hill Co., New York.

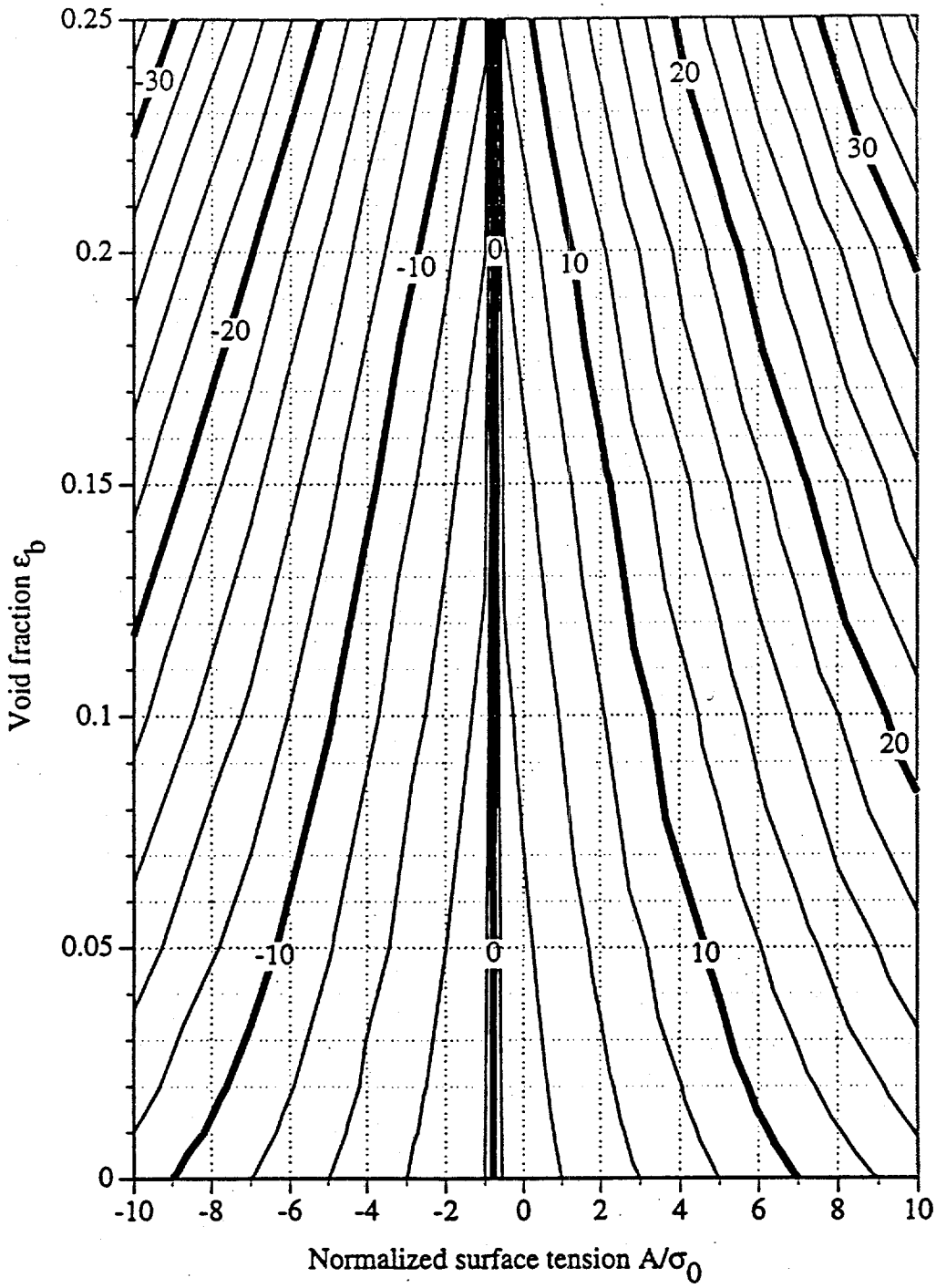

Figure F.1. The Maximum Normalized Stress $\sigma_{\theta\theta}/\sigma_0$ in a Thin Plate Filled with 2-D "Bubbles" when a Unidirectional Tensile Stress σ_0 Is Applied

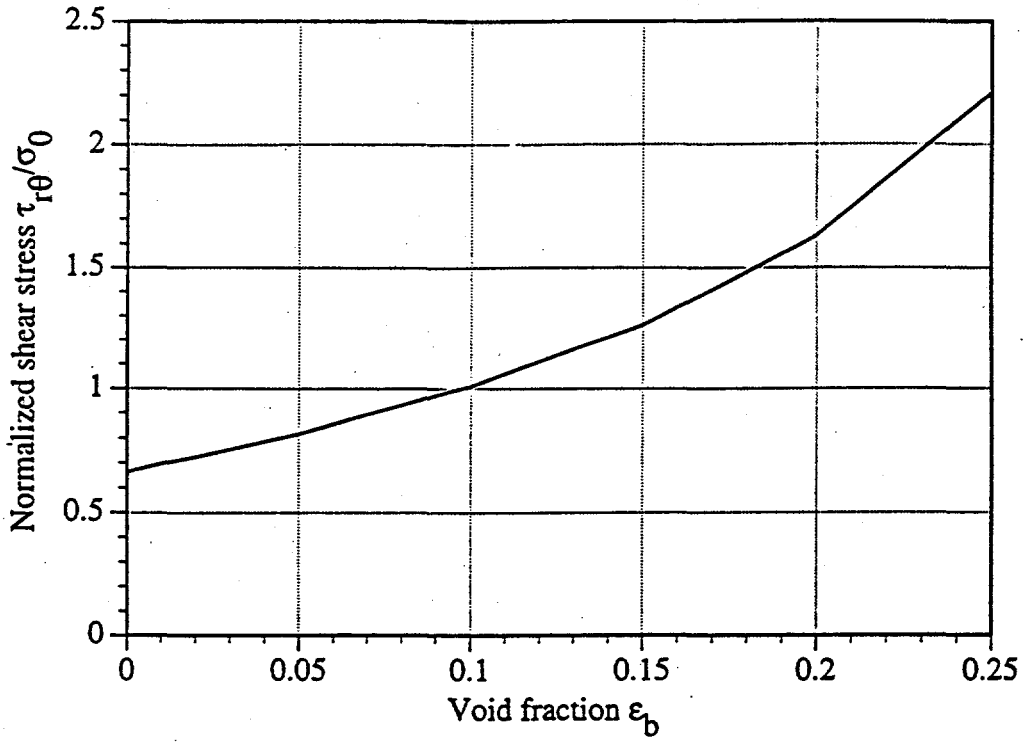

Figure F.2. The Maximum Normalized Shear Stress $\tau_{r\theta}/\sigma_0$ in a Thin Plate Filled with 2-D "Bubbles" when a Unidirectional Tensile Stress σ_0 Is Applied

DISTRIBUTION

No. of Copies

OFFSITE

2 DOE/Office of Scientific and Technical Information

B. S. Hudson
P.O. Box 271
Lindsborg, KA 67456

K. Pasamehmetoglu
Los Alamos National Laboratory
P.O. Box 1663
Mailstop K555
Los Alamos, NM 87545

W. R. Rossen
Department of Petroleum and Geosystems Engineering
University of Texas at Austin
Austin, TX 78712-1061

R. A. Tennant
Los Alamos National Laboratory
Mailstop J565
P.O. Box 1663
Los Alamos, NM 87545

ONSITE

3 DOE Richland Operations Office

J. M. Gray	S7-54
M.F. Jarvis	S7-54
G. Rosenwald	S7-54

No. of Copies

17 Westinghouse Hanford Company

H. Babad	S7-15
W. B. Barton	R2-11
R. J. Cash	S7-15
D. L. Herting	T6-09
J. D. Hopkins	R2-11
J. Jewett	T6-09
G. D. Johnson (5)	S7-15
J. W. Lentsch	S7-12
E. J. Lipke	S7-14
N. G. McDuffie	S7-15
J. C. Person	T6-09
D. A. Reynolds	R2-11
R. J. Van Vleet	H4-62

48 Pacific Northwest Laboratory

Z. I. Antoniak	K7-15
S. Q. Bennett	K7-90
P. R. Bredt	P7-27
J. W. Brothers (5)	K5-22
S. A. Bryan	P7-25
J. L. Buelt	P7-41
C. J. Call	P7-20
J. A. Campbell	P8-08
P. A. Gauglitz (15)	P7-41
J. D. Hudson	K7-15
T. E. Michener	K7-15
F. E. Panisko	P8-34
L. R. Pederson	K2-44
M. R. Powell (4)	P7-19
S. D. Rassat (4)	P7-35
H. C. Reid	K7-15
A. Shekarriz	K7-15
C. W. Stewart	K7-15
J. M. Tingey	P7-25
D. S. Trent	K7-15
P. D. Whitney	K5-12
Technical Report Files (3)	